Multidimensional Late-Time Modeling of Type Ia Supernova Spectra

by

János Botyánszki

A dissertation submitted in partial satisfaction of the

requirements for the degree of

Doctor of Philosophy

in

Physics

in the

Graduate Division

of the

University of California, Berkeley

Committee in charge:

Professor Daniel N. Kasen, Chair
Professor Alexei V. Filippenko
Professor Saul Perlmutter

Spring 2018

Multidimensional Late-Time Modeling of Type Ia Supernova Spectra

Abstract

Multidimensional Late-Time Modeling of Type Ia Supernova Spectra

by

János Botyánszki

Doctor of Philosophy in Physics

University of California, Berkeley

Professor Daniel N. Kasen, Chair

Type Ia supernovae (SNe Ia) have been used successfully to derive constraints on the expansion history of our universe. They are also a source of kinetic energy and iron-group elements in galaxies, and they are inherently interesting cosmic events whose study requires the application of sophisticated algorithms and computational architectures. Late-time, or nebular, observations of SNe Ia are taken during the phase in which the ejecta are optically thin and are heated by radioactive decay of iron-group elements. They are a powerful and unique probe of ejecta properties and may be used to infer information about the explosion itself. In this thesis, I present a three-dimensional radiative transfer code to calculate the properties and synthetic data of optically thin, homologously-expanding gases illuminated by radioactive decay energy and apply it to a variety of SN Ia explosion models. I derive the relationship between key explosion properties and nebular spectra using a suite of parametrized models, which results in the identification of a number of degeneracies. I also present the first-ever multidimensional nebular spectra of SNe Ia interacting with a binary companion, which leads us to rule out classic single-degenerate systems as SN Ia progenitors.

I dedicate this thesis to my wife, Sahar, who has been a constant source of strength for me and a catalyst of growth throughout my studies.

Contents

Acknowledgments

A number of amazing people have helped make this dissertation a reality over the past few years. I want to thank my wife Sahar, parents János and Erzsébet, and sisters Lívia and Zsófia for their endless love and support.

I am grateful to my advisor, Dan Kasen, for his guidance along this fruitful and interesting path, and to my groupmates, Jennifer Barnes and Nathan Roth, who have been an immense help throughout these years.

I am also grateful to my committee members, Alex Filippenko, Saul Perlmutter, and Eliot Quataert, whose helpful comments have helped shape this work, and I owe many thanks to Anne Takizawa, Claudia Trujillo, and Donna Sakima of the Berkeley Physics department for their invaluable support.

This material is based upon work supported by the National Science Foundation Graduate Research Fellowship Program under Grant No. DGE 1106400.

Chapter 1

Introduction

Cosmic explosions originating from dying stars are known as supernovae (SNe). While stars are the laboratories that build heavy elements like carbon and oxygen from the primeval elements (primarily hydrogen and helium), SNe synthesize the bulk of iron-group elements (IGEs; Leibundgut, 2000) and, via violent explosion, enrich their galaxies with these elements and provide a source of thermal and kinetic energy (McKee and Ostriker, 1977; Powell, Slyz, and Devriendt, 2011).

There has been a growing effort over the past few decades to observe and classify these explosions (Filippenko, 1997; Maoz, Mannucci, and Nelemans, 2014) and to model their physics (Hillebrandt et al., 2013; Woosley and Weaver, 1986). There has been tremendous progress in modeling the explosion at all stages, from the stellar and binary evolution (Woosley, Heger, and Weaver, 2002; Woosley and Janka, 2005) through explosion and into the remnant phases. A great deal is now known about these events from both the theoretical and observational perspectives (see, e.g., Hillebrandt et al., 2013). Modeling efforts have probed the trigger mechanisms of the explosions (Hillebrandt and Niemeyer, 2000), hydrodynamical evolution of the deflagrations and detonations, and radiation transport through unbound ejecta in early (*photospheric*; Dessart and Hillier, 2010; Kasen, Thomas, and Nugent, 2006; Kerzendorf et al., 2014; Sim, 2007), late (*nebular;* Axelrod, 1980; de Kool, Li, and McCray, 1998; Kozma and Fransson, 1998a,b; Liu, Jeffery, and Schultz, 1997; Ruiz-Lapuente and Lucy, 1992), and remnant phases (Truelove and McKee, 1999).

In this thesis, I focus on the theoretical modeling of the late-time (nebular) spectra of a subclass of explosions called Type Ia SNe. Interested readers should consult the following review papers for further information: Branch and Khokhlov, (1995), Filippenko, (1997), Hillebrandt and Niemeyer, (2000), Maoz, Mannucci, and Nelemans, (2014), Wang and Han, (2012), and Woosley and Weaver, (1986). These reviews and references therein provide a view into the rich and fascinating world of exploding white dwarfs.

1.1 Classification of Supernovae

The first contemporary light curves and spectra of SNe were obtained in the 1930s (e.g., Baade and Zwicky, 1938; Minkowski, 1939). At the time, there was little theoretical intuition into these events. Two main classification schemes have endured, one based on spectral and light-curve (LC) characteristics, the other based on physical explanations.

1.1.1 Spectral Classification

The first classification scheme for SNe was based on spectral features in the early-time spectrum. In particular, Type I and Type II were defined based on the absence or presence (respectively) of hydrogen features in early-time spectra (Minkowski, 1941). Type I was further differentiated based on the presence or absence of Si and He features. Type II SNe were further classified by the shape of their light curves (i.e. brightness vs. time). The following basic classes emerged (e.g., Filippenko, 1997):

- Type Ia: No H or He, but strong Si, features in the early-time optical spectrum
- Type Ib: No H or Si, but obvious He, features
- Type Ic: No H, Si, or He features
- Type IIL: H features, linearly declining LC (in magnitudes/day)
- Type IIP: H features, plateau in LC

While this classification system provides a good first pass at organizing the sample of SNe, the system does not provide any intuition about the physical differences between these classes, and occasionally an observed event may transition from one class to another (e.g. Folatelli et al., 2006). Furthermore, as the number of peculiar events in the sample increases, it becomes useful to have a physically motivated classification for SNe.

1.1.2 Physical Classification

Based on current understanding, SNe originate from either thermonuclear explosion of a white dwarf (WD) star or the collapse of a massive star's core. The Type Ia class consists of thermonuclear WD explosions, while the other classes (Types Ib, Ic, and II) correspond to core-collapse SNe. Therefore, spectra classified as SNe Ib/Ic/II share a similar explosion mechanism but differ in progenitor and/or phase of observation. SNe Ia are qualitatively different in that the exploding object is a compact star whose disruption is triggered by interaction with a binary companion. Both spectroscopic and physical classification systems are in wide use today.

1.1.3 Normal and Peculiar SN Ia Subclasses

Branch, Fisher, and Nugent, (1993) define normal SNe Ia as those resembling SN 1981B and other events, such as SN 1986G, SN 1991bg, and SN 1991T, as peculiar; see Branch, Fisher, and Nugent, (1993) for a list of other normal SNe Ia. These so-called "Branch-normal" SNe Ia make up a large majority of the Type Ia sample. Much of their observational diversity can be explained by the width-luminosity relation (WRL; Phillips, 1993), which relates an event's peak luminosity to the width of its light-curve. Failure to fall on the typical WLR is one indication that an event is of a peculiar subclass. A few of these peculiar classes are mentioned here, described relative to normal SN Ia properties.

The largest class of peculiar SNe Ia is known as "SN 2002cx-like" or Type Iax SNe; see Foley et al., (2013) and references therein. They show faster light-curve evolution, are subluminous, and exhibit a combination of continuum and line emission at late times.

"SN 1991bg-like" SNe are a class of significantly subluminous events with a fast light-curve decline (Filippenko et al., 1992b). They show early-time optical features from Ti II and C I that are typically not found in normal SNe Ia. Nebular spectra suggest lower ionization of atoms in the core.

"SN 1991T-like" SNe are slightly brighter-than-normal events that have unusual pre-maximum spectra, lacking strong features from intermediate-mass elements (IMEs) and showing strong features from iron-group elements (IGEs; Filippenko et al., 1992a). The latter implies a relatively high amount of IGEs mixed into outer layers, where typically only IMEs are detected. This is also confirmed by broader emission at nebular times, indicating that IGEs are located at higher velocities.

Calcium-rich "gap transients" occupy the peak-luminosity gap between novae and normal SNe Ia (Kasliwal et al., 2012; Lunnan et al., 2017; Perets et al., 2010). They have fast light-curve evolution, are subluminous, evolve to the nebular phase quickly, and show a high [CaII] to [OI] ratio at late times. Perhaps more surprisingly, they are found to be highly offset from any potential host galaxy. Proposed progenitor systems include mergers between WDs and neutron stars, binary systems ejected from the nucleus of a host through interaction with a supermassive black hole, and failed deflagrations of WDs.

"Super-Chandrasekhar" SNe Ia are slowly-evolving, superluminous events (Hicken et al., 2007; Howell et al., 2006). They are thought to have ejecta masses over the Chandrasekhar mass (hence their name) and to produce large amounts of ^{56}Ni in order to explain their high peak luminosities. Early-time spectra show lines from unburnt carbon even past maximum brightness.

These and other peculiar subclasses constitute an exciting area of research. Most of these events transition to an optically-thin regime into which our analyses may be extended, and future modeling work with the code presented in this thesis could be quite fruitful.

1.2 Observational Constraints on Normal SNe Ia

Henceforth, we turn our attention toward the study of normal SNe Ia. Current efforts to model the progenitors of SNe Ia rely on a number of observational constraints. Any model of a SN Ia progenitor must be able to explain the following observational constraints (Branch and Khokhlov, 1995; Leibundgut, 2000):

- Absence of broad hydrogen and helium spectral features in early-time spectrum
- Presence of both IMEs and IGEs
- Broad spectral features indicating ejecta velocities of $\sim 10,000 - 20,000$ km s^{-1}
- Light-curve peak absolute B-band magnitude around -19
- A continuum-free late-time spectrum dominated by the forbidden emission lines of IGEs
- Lack of significant polarization

Hydrogen is not predicted to be present in an exploding C-O WD, and any interaction with circumstellar material (CSM) would produce narrow H features. As will be discussed in Chapter 4, there is lack of late-time observational evidence for the interaction of the ejecta with the binary companion. The balance between IME and IGE abundances puts constraints on the explosion during which nucleosynthesis takes place. The nucleosynthesis of elements up to nickel is enough to unbind the WD, while radioactive decay of ^{56}Ni is required to power the resulting light-curve.

1.3 Introduction to SN Ia Progenitors

SNe Ia are thought to be explosions of WDs in a binary system (Hoyle and Fowler, 1960), and efforts are underway to explain which progenitor scenarios are responsible for producing the observed sample of SNe Ia. Stellar and binary evolution determine the possible progenitor scenarios and their relative fraction. Hydrodynamical modeling probes the interaction between the two stars, the mechanism by which the explosion is triggered, the evolution of the flame structure, and the nucleosynthesis during the burning phase. Radiative transfer tracks the radiation produced in the gas and provides predictions of light curves and spectra. Interactions with CSM, a binary companion, and ISM contribute to the observed radiation at various phases of evolution.

This section introduces the main progenitor scenarios, their strengths and weaknesses, and differentiating factors that can be probed using nebular modeling. See Wang and Han, (2012) for a comprehensive review of progenitor models.

1.3.1 The Single-Degenerate Chandrasekhar Mass Model

Single-degenerate (SD) models assume that the binary companion to the WD is a non-degenerate star (Whelan and Iben, 1973). As gravitational wave emission brings the two stars closer together, the binary companion may transfer mass to the WD through Roche lobe overflow (RLOF) or a symbiotic wind. The effect is to increase the mass of the WD until the theoretical Chandrasekhar mass limit ($M_{\rm ch} \approx 1.4 M_{\odot}$), which is defined as the mass above which a degenerate star would undergo gravitational collapse (Chandrasekhar, 1931; Stoner, 1930). Before it reaches this mass limit, however, the core will start a period of convective carbon simmering, which produces some neutron-rich isotopes like ^{22}Ne (Chamulak et al., 2008; Martínez-Rodríguez et al., 2016; Piro and Bildsten, 2008). The end of this phase is marked by deflagration (subsonic burning) of the core material. Since the mass of the WD approaches $M_{\rm ch}$ for these models, they are called "Chandrasekhar mass" explosion models.

A pure deflagration of the WD does not produce enough energy and ^{56}Ni to both disrupt the star and power the typical SN Ia light-curve (Röpke et al., 2007, 2006), while a pure detonation of the WD produces almost exclusively IGEs (Arnett, 1969). It is common, therefore, to add a deflagration-to-detonation transition (DDT) to the hydrodynamical modeling by hand in order to pre-expand the star before detonation to match observed SN Ia properties (Khokhlov, 1991). This gives rise to the alternate name "delayed-detonation" for these models.

The SD-$M_{\rm ch}$ model has a few key predictions that sets it apart from other progenitor scenarios. Owing to the turbulent deflagration phase, the core of the ejecta can be highly asymmetric (e.g., Seitenzahl et al., 2013). Furthermore, high core densities (as a result of being close to $M_{\rm ch}$) lead to electron captures during the deflagration phase that neutronize the core ejecta. This would impact the final isotopic abundances of IGEs, mainly ^{54}Fe and ^{58}Ni (Hillebrandt et al., 2013). Finally, interaction with a non-degenerate binary companion is expected to strip up to $0.5 M_{\odot}$ of solar-abundance material that becomes embedded in the ejecta (Chugai, 1986; Wheeler, Lecar, and McKee, 1975). These key predictions will be tested by the radiative transfer code presented in this thesis.

1.3.2 The Double-Degenerate Merger Model

The double-degenerate (DD) merger model proposes that the binary companion is also a WD (Iben and Tutukov, 1984; Webbink, 1984). The two stars merge and produce the necessary conditions for the primary WD to detonate. This scenario produces an explosion of a lower mass WD, and thus a pure detonation produces the correct amount of IMEs and IGEs. The conditions necessary for triggering the detonation are found to be met by prompt (or violent) mergers (Moll et al., 2014; Pakmor et al., 2012; Ruiter et al., 2013), and these scenarios produce light curves and spectra consistent with observations as long as the mass ratio between the two WDs is not too close to unity (Pakmor et al., 2011). On the other hand, a slower disruption of the companion WD leads to an hourglass-shaped accretion disk that produces peculiar light curves and spectra (Raskin et al., 2014).

The lack of turbulent burning in this scenario suggests a highly symmetric explosion. The interaction with the binary companion does not produce strong observational diagnostics. In addition, low burning densities limit neutronization from electron captures, significantly reducing the amount of stable nickel in the gas at late times.

1.3.3 The Double-Detonation Model

An alternative to the SD and DD merger models comes from the insight that mass transfered from a helium companion (degenerate or not) may be easier to detonate than the C/O in the primary. Detonation of a helium shell can lead to a second detonation in the primary WD (Fink, Hillebrandt, and Röpke, 2007; Livne, 1990; Shen and Bildsten, 2014). Originating from binaries with low-mass primary WDs, these are called "sub-Chandrasekhar" explosion models. Like the DD merger model, this model should result in little material stripped from the binary companion and low neutronization.

1.3.4 Other Models

Some have proposed scenarios in which a direct collision of two WDs produces a normal SN Ia (Benz, Thielemann, and Hills, 1989; García-Senz et al., 2013; Kushnir et al., 2013; Raskin et al., 2010, 2009; Rosswog et al., 2009). This scenario has an increased probability of taking place in dense stellar environments such as globular clusters. Another scenario involves angular momentum transfer during the mass-transfer phase that leads to a spin-up and subsequent spin-down of the primary WD, delaying explosion and allowing the possibility of advanced evolution of the binary companion (Di Stefano, Voss, and Claeys, 2011; Justham, 2011). This may explain the nondetection of solar-like emission at late times.

1.4 The Nebular Phase of Supernovae

SN ejecta are found to be in homologous expansion, in which the radial distance of an element of the gas from the center of explosion is proportional to the time since explosion and velocity of the element ($r = v_{\rm ej}t$). The first few weeks of expansion are called the photospheric phase, wherein the ejecta are optically thick and heated by decaying ^{56}Ni. The light-curve is powered by this radioactive heating. Spectra in this phase are well modeled by a blackbody illuminating a photosphere that produces superimposed, broad P-Cygni features.

The nebular phase is defined as the time at which the SN ejecta become optically thin (Axelrod, 1980). The transition to the nebular phase can be estimated by setting the optical depth to unity, assuming the opacity is dominated by electron scattering ($\kappa_{\rm es} = 0.2$ cm^2 g^{-1}), and solving for time since explosion:

$$\begin{aligned} \tau \approx 1 &\approx \rho \kappa_{\rm es} R \\ &\approx M R^{-2} \kappa_{\rm es} \\ &\approx M (v_{\rm ej} t)^{-2} \kappa_{\rm es} \\ t &\approx 137 \left(\frac{M}{M_{\rm ch}} \right)^{1/2} \left(\frac{v_{\rm ej}}{20,000 \text{ km s}^{-1}} \right) \text{ days}, \end{aligned} \tag{1.1}$$

where $M_{\rm ch} = 1.4\ M_\odot$ is the Chandrasekhar mass and $v_{\rm ej}$ is the outer velocity of the ejecta.

A significant amount of radioactive ^{56}Ni is produced in SN explosions, powering the early-time light-curve. Since ^{56}Ni has a half-life of only 6 days, the ejecta at nebular times are instead heated by gamma-rays and positrons from the radioactive decay of ^{56}Co, which has a longer half-life of 77 days.

The late-time spectrum is dominated by forbidden emission, and the features depend on which coolants are present in the ejecta. For SNe Ia, a large fraction of the ejecta is in the form of stable ^{56}Fe, while core-collapse SNe tend to have more IMEs such as oxygen and calcium.

The radioactive energy from ^{56}Co decay is deposited via Compton scattering interactions with the electrons in the gas. This produces a non-thermal, high-energy population of electrons that (i) heat the gas, (ii) excite atomic transitions, and (iii) ionize atoms. The fraction of energy contributing to each of these channels has been studied by Kozma and Fransson, (1992) and Xu and McCray, (1991).

Photons produced by line transitions of moving atoms are subject to a Doppler shift in wavelength in the frame of the observer. In homologous expansion, this Doppler effect can be related to the line-of-sight distance from the center of the explosion. In particular, starting from the relativistic formula and assuming that ejecta velocities are low ($\beta = v/c << 1$),

$$\begin{aligned} \frac{\lambda_{\rm obs}}{\lambda_{\rm rest}} &= \sqrt{\frac{1-\beta}{1+\beta}} \\ &= \left(1 - \frac{1}{2}\beta + \mathcal{O}(\beta^2) \right) \left(1 - \frac{1}{2}\beta + \mathcal{O}(\beta^2) \right) \\ &= 1 - \beta + \mathcal{O}(\beta^2) \\ &\approx 1 - \frac{v}{c} \\ &= 1 - \frac{z}{ct}, \end{aligned} \tag{1.2}$$

where we have assumed the line-of-sight is along the z-axis and used the relations $v = Rt$, $z = R\tan(\theta)$, and $v_r = v\tan(\theta)$.

For each transition with rest wavelength $\lambda_{\rm rest}$, each point in the spectrum of a nebular gas is a sum over all of the emission in a plane perpendicular to the line of sight corresponding to the observed wavelength. Thus, the geometry of the ejecta along the line of sight may be probed using unblended lines of a nebular spectrum.

1.4.1 Using Nebular Modeling to Constrain Progenitor Scenarios

Nebular emission is found to be dominated by line cooling in an optically thin gas. The emission lines can therefore provide a wealth of information that can be used to validate explosion models.

Nebular spectra encode the emission of atomic transitions in planes perpendicular to the line of sight. This can be used to infer the geometry of the ejecta, with the caveat that the spectra are degenerate with regard to the distribution of emission in the planes. Asymmetrical burning is a key prediction of some SN Ia explosion models (e.g., Seitenzahl et al., 2013), and nebular modeling can be used to predict resulting line profiles. An early version of the code presented in this thesis was used to model the bimodal geometry of the core-collapse SN 2011dh (Shivvers et al., 2013) to explain the presence of double features in the nebular spectrum.

Neutronization from high-density burning is expected to produce stable IGEs, which cool efficiently but do not contribute to heating the gas. As a result, the ionization state of regions with a large fraction of stable IGEs is expected to differ from that of regions produced by scenarios with minimal neutronization. In particular, Chandrasekhar mass models predict high neutronization near the core, unlike sub-Chandrasekhar mass models. Therefore, it may be possible to differentiate these models based on ratios of line emission produced by various ionization states.

Interaction with some binary companion types is expected to result in stripped gas embedded into the core of the ejecta. Considering this gas is thought to be of solar-like abundance, hydrogen and helium emission may contribute to the spectrum at nebular times. While observations of SNe Ia have not detected this emission, it may be possible to hide it if, for example, the gas is highly ionized.

1.5 Organization of This Work

In this thesis, I present a code to calculate the spectra of explosion models in the nebular approximation. In Chapter 2, I introduce a tool to calculate the nebular spectra of supernovae. I explain the methodologies and physics relevant to the nebular phase, as well as the assumptions that are needed for modeling SN Ia nebular spectra. In Chapter 3, I present a parameter-space study with toy SN Ia models to illuminate the dependence of their nebular spectra on explosion properties, model abundances, and atomic data sources. We find that nebular spectral features are degenerate with respect to parameters such as explosion energy, ejecta mass, and synthesized ^{56}Ni mass. We conclude that a range of generic SN Ia models

from sub-Chandrasekhar mass to super-Chandrasekhar mass are in principle able to fit the observed spectral features. In Chapter 4, I present multidimensional spectra of SN Ia models with stripped gas from a binary companion. Using two-dimensional hydrodynamic interaction models, we rule out main-sequence companions as being a viable progenitor channel of most normal SNe Ia.

Chapter 2

Nebular Modeling Methods

2.1 Introduction

Nebular spectra can be used to study the uncertain progenitors of Type Ia supernovae (SNe Ia; Maeda et al., 2010b; Mazzali and Hachinger, 2012; Mazzali et al., 2015, 2011; Sollerman et al., 2004). While SNe Ia are thought to be the result of the explosion of carbon-oxygen white dwarfs (C/O WDs) in a binary system (Hoyle and Fowler, 1960), their progenitor systems and explosion mechanisms are still unknown. Despite the success of the empirical width-luminosity relation (Phillips, 1993) to calibrate luminosities of SNe Ia, systematic variation due to intrinsic SN Ia diversity is an ongoing challenge for precision cosmology (Howell, 2011).

Several candidates for the progenitors of "normal" SNe Ia have been proposed (see Branch, Fisher, and Nugent, 1993; Maoz, Mannucci, and Nelemans, 2014; Wang and Han, 2012, and references therein). In the single-degenerate $M_{\rm Ch}$ model, the WD gains mass from a non-degenerate binary companion (Whelan and Iben, 1973) and ignites carbon burning when the mass approaches $M_{\rm ch} \approx 1.4 M_{\odot}$. In the double-detonation model, a layer of helium gas from a binary companion detonates above the primary C/O WD causing the WD to detonate at a mass $< M_{\rm Ch}$ (Fink, Hillebrandt, and Röpke, 2007; Guillochon et al., 2010; Livne, 1990; Shen and Bildsten, 2014; Woosley and Weaver, 1994). In the double-degenerate model, two WDs coalesce or collide and may detonate violently on impact or subsequent to the merger (Benz, Thielemann, and Hills, 1989; Iben and Tutukov, 1984; Kashyap et al., 2015; Kushnir et al., 2013; Moll et al., 2014; Pakmor et al., 2012; Raskin et al., 2009; Rosswog et al., 2009; Webbink, 1984). It may be that SNe Ia come from most, if not all, of these progenitor channels. A main goal of spectral modeling is to help understand the origin of different events.

Nebular spectra reveal emission throughout the entire ejecta and so are a valuable probe of density and compositional structure. If the ejecta mass, kinetic energy, and/or compositional yields can be determined, these can differentiate explosion scenarios. For example, it is thought that $M_{\rm Ch}$ models produce more stable IGEs (such as ^{58}Ni and ^{54}Fe) than sub-$M_{\rm Ch}$

mass models because of burning at higher central densities (Iwamoto et al., 1999). Nebular line profiles are also sensitive to global asymmetries and therefore offer a way to study the imprints of the explosion mechanism on ejecta geometry.

Initial work by Axelrod, (1980) enabled a number of codes used to model the nebular spectra of supernovae (Kozma and Fransson, 1998a,b; Liu, Jeffery, and Schultz, 1997; Ruiz-Lapuente and Lucy, 1992). Updated codes use improved atomic data and incorporate more sophisticated radiative transport and non-thermal deposition physics (Dessart and Hillier, 2011; Jerkstrand, Fransson, and Kozma, 2011; Kozma et al., 2005; Li, Hillier, and Dessart, 2012; Maeda et al., 2006; Maurer et al., 2010; Mazzali et al., 2007b, 2001; Sollerman et al., 2000, 2004). Despite the publication of numerous 3D hydrodynamic simulations of SNe Ia (e.g., Hillebrandt et al., 2013), few such explosion models have been analyzed in the nebular phase (but see Kozma et al., 2005). Furthermore, previous nebular modeling work has focused on interpreting events individually (Ashall et al., 2016; Maeda et al., 2010a,b; Maurer et al., 2011; Mazzali and Hachinger, 2012; Mazzali et al., 2015, 2011; Sollerman et al., 2004; Stehle et al., 2005; Taubenberger et al., 2013), rather than carrying out parameter studies to identify the general dependencies and degeneracies of nebular spectra (but see Ruiz-Lapuente, 1997; Ruiz-Lapuente and Lucy, 1992).

In this chapter, we present our method of calculating level populations (§2.2.2), temperature and ionization balance (§2.2.4), and nebular spectra (§2.2.5). We provide a thorough discussion of non-thermal deposition and other key atomic processes in §2.3.

2.2 Code Implementation

We have developed a new 3D radiative transfer tool to model nebular spectra of SNe. Given an initial ejecta model, the code calculates the emissivity of each atomic transition by solving for the temperature, ionization state, and NLTE atomic level populations, including non-thermal effects from radioactive decay products, and generates spectra by integrating the radiative transfer equation in a moving medium.

2.2.1 Basic Assumptions

The underlying supernova ejecta model is specified by the mass density and elemental abundances in each zone on a 3D Cartesian grid. We assume the ejecta are in homologous expansion (i.e., velocity proportional to radius) which is appropriate for SNe Ia at a few seconds to days after explosion (e.g., Röpke, 2005). The structure of a homologous model at one epoch can be easily scaled to any other time, taking into account compositional changes due to radioactive decay. The models in this paper study SNe Ia out to 400 days and include the following species: C, O, Si, S, Ca, Fe, Co, and Ni (see §2.2.3 for a description of atomic data sources).

Our calculations assume stationarity – i.e., that the gas temperature and level populations reach equilibrium on a timescale short compared to the ejecta expansion timescale.

This assumption is reasonable except at rather late times ($\gtrsim$500 days), when thermal and ionization freeze-out may become important (Fransson and Jerkstrand, 2015; Fransson and Kozma, 1993; Kozma and Fransson, 1998a; Sollerman et al., 2004).

Our transport solver assumes that the ejecta are optically thin to radiation. For many supernovae, this is true in the optical and infrared regions at times $\gtrsim$ 100 days. However, at blue and ultraviolet wavelengths ($\lesssim$ 4000 Å), the ejecta may remain opaque to iron-group lines for hundreds of days (Friesen et al., 2017). This limits the reliability of our nebular models at short wavelengths and may affect the calculated ionization fractions (e.g., Sollerman et al., 2004), issues that will be addressed in the future by incorporating a more general transport solver.

2.2.2 Non-LTE Level Populations

To calculate spectral emission from the SN nebula, one has to determine the level populations of each ion in the gas. Since local thermodynamic equilibrium (LTE) is a poor approximation at these epochs, we solve for each species the set of non-LTE (NLTE) equations expressing statistical equilibrium

$$\mathbf{M}\vec{n} = \mathbf{0}, \tag{2.1}$$

where $\vec{n}$ is a vector of level populations for the species, and the matrix $\mathbf{M}$ encodes the transition rates between the various levels and ionization states (see, e.g., Li and McCray, 1993). To the set of equations must be added the constraint of number conservation.

A generalized form for the statistical equilibrium rate equations is

$$n_{\mathrm{I,i}}\left(R_{\mathrm{I,i}} + \sum_{\mathrm{j}\neq\mathrm{i}} \mathcal{E}_{\mathrm{ij}}\right) = \sum_{\mathrm{k}\neq\mathrm{i}} n_{\mathrm{k}}\mathcal{E}_{\mathrm{ki}} + n_{\mathrm{I+1,gs}} n_{\mathrm{e}} \alpha_{\mathrm{i}}, \tag{2.2}$$

where $n_{\mathrm{I,i}}$ is the level population of the i-th level of the ion with I-th ionization state, n_{e} is the electron density, $R_{\mathrm{I,i}}$ is the total ionization rate from the i-th to the I+1-th ionization state (including photoionization, collisional ionization, and non-thermal ionization), and $\alpha_{\mathrm{i}}(T)$ is the total recombination coefficient from ionization state I's ground state to the i-th level (including radiative, dielectronic, and three-body recombination). $\mathcal{E}_{\mathrm{ij}}$ are bound-bound rate coefficients between levels i and j, including spontaneous emission, stimulated absorption/emission, and collisional excitation/de-excitation.

The microphysics relevant to the nebular phase calculation is encoded into the transition matrix of Equation 2.1. For the SN Ia problem, we treat collisional ("electron-impact") bound-bound and bound-free processes, radiative and dielectronic recombination, and non-thermal deposition of ^{56}Co energy into heating, excitation, and ionization channels. Following Nahar and Pradhan, (1997), we assume that all collisional ionization rates are ground-state rates, and that radiative recombinations come from the ground state. Details of the implementation of these processes are given in §§2.2.3-2.3.4.

2.2.3 Atomic Data

For the current version of the code, we use the atomic data compilation of the CMFGEN code (Hillier and Miller, 1998; Li, Hillier, and Dessart, 2012) for radiative transition probabilities (Einstein A coefficients), effective collisional strengths Υ_{ij} (see §2.3.3 for treatment of missing data), and photoionization cross sections. We take ground-state ionization energies from NIST (Kramida, Ralchenko, and Reader, 2016). For thermal collisional ionization rates, we use the results of Voronov, (1997). For collisional ionization cross sections, we use Mattioli et al., (2007) and references therein. Radiative and di-electronic recombination rates are taken from the CHIANTI database v.8 (Del Zanna et al., 2015a; Dere et al., 1997).

2.2.4 Temperature and Ionization Balance

We use an iterative nonlinear solver to determine the free electron density and temperature in each zone. The electron density is constrained by the charge conservation condition that all free electrons come from ionization,

$$n_e = \sum_{k,i} n_{k,i} i, \tag{2.3}$$

where $n_{k,i}$ represents the population of the i-th ionization stage of the k-th species (i = 0 is neutral). Given that the non-thermal deposition fractions (η_{ij} and η_k in Equations 2.8-2.9) are level-population dependent, we recalculate them during each iterative step until convergence is reached.

The temperature of each zone is calculated from the balance of heating from radioactive decay and cooling due to line emission. The line emissivity (units ergs s^{-1} cm^{-3}) from a transition between the i-th and j-th levels of an ion ($E_j > E_i$) is

$$\dot{\epsilon}_{ij}(T) = h\nu_{ij} A_{ij} n_j, \tag{2.4}$$

where ν_{ij} is the photon frequency of the transition, A_{ij} is the spontaneous radiative decay rate (Einstein A coefficient), and n_j is the population of the j-th level of the ion. The temperature sensitivity of $\dot{\epsilon}_{ij}$ arises primarily from the temperature-dependent collisional excitation rates, which are important in setting the populations n_j for low-lying states.

The total emissivity per unit volume is then a sum over all line transitions which, in equilibrium, is equal to the energy deposition by radioactivity,

$$\sum_{i,j} \dot{\epsilon}_{ij} = \dot{\epsilon}_{rad}, \tag{2.5}$$

where {i,j} runs over all transitions. Note that Equation 2.5 represents a balance of all emission and deposition processes, not just the thermal processes.

We use an iterative BrentDekker method to solve the non-linear equations 2.3 and 2.5 for the temperature and electron density in each zone. For each iteration, we solve the NLTE rate

equations to determine the ionization/excitation state and emissivity. The values and T and n_e are then adjusted and the procedure iterated until thermal and ionization equilibrium is reached. A single zone typically converges within 200-400 iterative steps to reach an accuracy of 0.1% in temperature.

2.2.5 Spectrum Calculation

Once the line emissivities (Equation 2.4) are known for all transitions in a converged model, we can integrate the emission for any arbitrary geometry to determine the nebular spectrum of the SN. Assuming homologous expansion ($r = vt$) and choosing the direction to the observer to be the z-axis, the nonrelativistic Doppler effect along the line of sight is

$$\lambda_{\rm obs} = \lambda_{\rm ij} \left(1 - \frac{z}{ct}\right), \tag{2.6}$$

where $\lambda_{\rm obs}$ is the observed wavelength of a line transition with rest-frame wavelength $\lambda_{\rm ij}$. Equation 2.6 allows us to associate the observed flux at wavelength $\lambda_{\rm obs}$ with the line emission integrated over a specific plane (perpendicular to the z-axis) sliced through the ejecta. For isolated transitions, this mapping can be used to constrain the geometrical distribution of material along the line of sight (see, e.g., Shivvers et al., 2013). Since the bulk of the emission typically comes from ejecta with velocities $\lesssim$10,000 km/s, using the nonrelativistic Doppler shift leads to errors in z-mapping of only $\lesssim$ 3% while allowing the calculation to run significantly faster.

Assuming the ejecta are optically thin, the observed specific intensity can be expressed as the integral

$$L_\lambda(\lambda)d\lambda = \left[\sum_{\rm i,j} \frac{ct}{\lambda_{\rm ij}} \int \dot{\epsilon}_{\rm ij}(x,y,z)dxdy\right] d\lambda, \tag{2.7}$$

where the sum {i,j} runs over all possible transitions, and the integration is over the $x-y$ plane at location $z = ct(\lambda_{ij} - \lambda)/\lambda_{ij}$. The spectral flux observed at Earth is simply $F_\lambda = L_\lambda/(4\pi D^2)$, where D is the distance to the source.

2.2.6 Physical Processes Neglected

Dust formation might be possible in SNe Ia at late times, but not necessarily in significant amounts (Nozawa et al., 2011). Further, observations of the nearby SN 2011fe show no evidence for dust formation at 930 days past maximum brightness (Kerzendorf et al., 2014). We therefore neglect dust formation and plan on implementing it in future work.

While implementing photoionization and stimulated radiative processes in our code, we neglect them for the work published in this paper under the assumption that there is negligible continuum radiation field.

Charge transfer (CT) is expected to occur in SNe between neutral atoms and ions (Swartz, 1994). While CT might affect ionization fractions of SNe Ia at later times, we tested CT

between ions of Fe and found that their effect on the nebular spectrum at 200-400 days is negligible. This is because the nebula is primarily ionized gas, and therefore the rate of ionization/recombination due to CT is subdominant. Since CT preferentially ionizes neutral atoms (as Coulomb repulsion suppresses ion-ion interactions), we expect that neutral atoms like O I and Fe I should not contribute much to nebular emission. One could add a detailed CT treatment to the code in the future in order to quantify this effect.

2.2.7 Code Verification

We ran a number of tests to verify the code. We tested the NLTE level population solver in the limit that collisional processes dominate and in the limit that the radiation field is the Planck function, both resulting in the expected LTE level populations. We also tested the ionization solution in the collisional-ionization equilibrium (CIE) regime and found good agreement with previous results (e.g., Sutherland and Dopita, 1993). We further compared total CIE cooling functions for individual ions to published results from the Cloudy code (Gnat and Ferland, 2012). Given disparities in the atomic data inputs, exact agreement of the cooling functions is not expected, but we found reasonably similar values and temperature dependences in the regimes of interest. The radiation transport calculation of synthetic spectra was verified by comparing single line profiles to analytic solutions.

2.3 Atomic Processes

While the SN Ia application of the code was subject to a number of simplifications, future work may involve a wider set of physics essential for modeling low-density, optically-thin gases. Here we present a comprehensive overview of the atomic processes that are relevant for such situations.

2.3.1 Non-thermal Effects

Energy deposition due to the radioactive decay chain ^{56}Ni$\rightarrow^{56}$Co$\rightarrow^{56}$Fe is the dominant energy source for SNe Ia in the nebular phase (Colgate and McKee, 1969; Kuchner et al., 1994). Since ^{56}Ni decays on a timescale of $\tau_{\rm Ni} = 7.7$ days, its contribution to heating is minor by nebular times, while ^{56}Co decay ($\tau_{\rm Co} = 111.3$ days) is generally the most important source of radioactive energy. Other radioactive isotopes with half-lives in the nebular range (e.g., ^{22}Na, ^{35}S, ^{45}Ca, ^{46}Sc, ^{49}V, ^{54}Mn, ^{55}Fe, ^{57}Co, ^{58}Co, ^{65}Zn, and ^{68}Ge) are usually not produced in enough abundance to significantly contribute to heating at the epochs we consider here (Iwamoto et al., 1999; Seitenzahl et al., 2013), and are not included in the present calculations.

We determine the radioactive energy deposition rate in each zone using a 3D Monte Carlo radiation transport scheme (Kasen, Thomas, and Nugent, 2006) that samples gamma-ray wavelengths from the radioactive decay lines and treats energy losses due to Compton

scattering and photoionization. Positrons from ^{56}Co decay are assumed to be trapped locally, in accordance with recent observations of SNe Ia at late times, as presented by Kerzendorf et al., (2014) and Leloudas et al., (2009) (but see Dimitriadis et al., 2017).

The gamma-rays from ^{56}Co decay produce high-energy electrons ($E_0 \approx 1$ MeV) that interact with the ejecta through heating (Coulomb interactions), ionization, and excitation. These interactions affect the temperature and ionization state of the gas. The rates of excitation and ionization, respectively, by non-thermal electrons/positrons are given by

$$R_{\rm ex} = \frac{\dot{\epsilon}_{\rm rad}\eta_{\rm ij}}{\Delta E_{\rm ij} n_{\rm i}} \tag{2.8}$$

$$R_{\rm ion} = \frac{\dot{\epsilon}_{\rm rad}\eta_{\rm k}}{I_{\rm k} n_{\rm k}}, \tag{2.9}$$

where the transition from level i to level j (with $j > i$) has energy $\Delta E_{\rm ij}$, $n_{\rm i}$ is the level population of the i-th atomic level, $I_{\rm k}$ is the ionization potential of the ion indexed by k having number density $n_{\rm k}$, $\dot{\epsilon}_{\rm rad}$ is the radioactive energy deposition rate per unit volume, and $\eta_{\rm ij}$ and $\eta_{\rm k}$ refer to the non-thermal excitation and ionization deposition fractions, respectively, described in the following section.

2.3.2 Non-thermal Deposition Fractions

Radioactive decay of ^{56}Co atoms produces a population of high-energy, non-thermal electrons that deposit their energy into the ejecta. The electrons either heat, ionize, or excite the gas, and the fraction of energy going into these three channels has been shown to be insensitive to the initial energy of the electrons (Kozma and Fransson, 1992; Li, Hillier, and Dessart, 2012). Owing to the similar asymptotic behavior of collisional cross sections and plasma loss function (see below), our treatment is also independent of the initial energy of non-thermal electrons. Following the Continuous Slowing Down Approximation formulation of Xu and McCray, (1991), we can write the fraction of deposition into heating ($\eta_{\rm h}$), ionization ($\eta_{\rm k}$), and excitation (η_{ij}) as

$$\eta_{\rm h} = \frac{L_{\rm e}(E_0) + f\sum_{\rm k} x_{\rm k} I_{\rm k} Q_{\rm k}(E_0)}{A} \tag{2.10}$$

$$\eta_{\rm k} = \frac{x_{\rm k} I_{\rm k} Q_{\rm k}(E_0)}{A}, \tag{2.11}$$

where E_0 is the injection energy of electrons, L_e is the Coulomb loss function (see below), k labels an ion and its ionization potential $I_{\rm k}$, ionization fraction $x_{\rm k} = n_{\rm k}/n$, collisional ionization cross section $Q_{\rm k}(E)$, $f \approx 0.3$ is the mean energy of a secondary electron, and

$$\eta_{\rm ij} = \frac{x_{\rm i} E_{\rm ij} \sigma_{\rm ij}(E_0)}{A}, \tag{2.12}$$

where ij labels a transition with energy $E_{ij} = E_j - E_i > 0$, the fractional level population of the lower-energy state is $x_i = n_i/n$, the collisional excitation cross section is σ_{ij}, and

$$A = L_e(E_0) + (1+f)\sum_k x_k I_k Q_k(E_0) + \sum_{ij} x_i E_{ij}\sigma_{ij}(E_0) \tag{2.13}$$

is the normalization constant. The Coulomb loss function (Schunk and Hays, 1971; Xu and McCray, 1991) for high-energy electrons is

$$L_e(E) = -\frac{1}{n}\left(\frac{dE}{dx}\right)_e = x_e \frac{2\pi e^4}{E}\ln\left(\frac{4E}{\zeta_e}\right), \tag{2.14}$$

where E is the electron energy, e is the electron charge, $x_e = n_e/n$ is the electron fraction, and $\zeta_e = 2\hbar\omega_p$ for plasma frequency given by

$$\omega_p(n_e) = \sqrt{\frac{4\pi n_e e^2}{m_e}} = 56414.6\sqrt{\frac{n_e}{\mathrm{cm}^{-3}}}\ \mathrm{s}^{-1}. \tag{2.15}$$

For collisional ionization cross sections, we use the approximate form (Younger, 1981)

$$Q_I(E) = \frac{1}{uI^2}\left[A\left(1-\frac{1}{u}\right) + B\left(1-\frac{1}{u}\right)^2 + C\ \ln(u) + D\frac{\ln(u)}{u}\right]\ \mathrm{cm}^2, \tag{2.16}$$

where $u = E/I$, I is the ionization potential, and A, B, C, and D are fitting coefficients. We use the fitting coefficients published by Arnaud and Rothenflug, (1985a), taking into consideration updates by Arnaud and Raymond, (1992a) and Mattioli et al., (2007). While more recent calculations are available, Dere, (2007) points out that the discrepancies between new and old ionization rates are minor except for Ni V-XI, which are not important for this work. Coefficients are unavailable for Co II-IV, so we use Fe II-IV cross sections instead and plan to update these data when they become available in the future.

For collisional excitation cross sections of allowed transitions by non-thermal electrons, we use the approximation of van Regemorter, (1962),

$$\sigma_{ij} = \frac{8\pi}{\sqrt{3}}\frac{1}{k_i^2}\frac{I_H}{\Delta E_{ij}} f_{ij}\bar{g}\pi a_0^2, \tag{2.17}$$

where I_H is the ionization potential of hydrogen, k_i^2 is the initial electron energy scaled to 13.60 eV, f_{ij} is the oscillator strength, a_0 is the Bohr radius, and $\bar{g}$ is given by a quadratic fit to the results of van Regemorter, (1962),

$$\bar{g} \approx -0.0065\left(\frac{E}{\Delta E_{ij}}\right)^2 + 0.228\left(\frac{E}{\Delta E_{ij}}\right) - 0.07 \tag{2.18}$$

with an imposed high-energy limit of

$$\bar{g} = \frac{\sqrt{3}}{2\pi}\ln\left(\frac{\mathrm{E}}{\Delta \mathrm{E}_{ij}}\right),\ \mathrm{E}/\Delta\mathrm{E}_{ij} > 36 \tag{2.19}$$

for all ions, and a low-energy limit for positive ions

$$\bar{g} = 0.2,\ \mathrm{E}/\Delta\mathrm{E_{ij}} < \sqrt{2}. \tag{2.20}$$

Forbidden transitions must be treated separately. We use the following form for the collision cross sections:

$$\sigma_{\mathrm{ij}} = \frac{1}{g_{\mathrm{i}} k_{\mathrm{i}}^2} \Omega_{\mathrm{ij}} \bar{g} \pi a_0^2, \tag{2.21}$$

where g_i is the statistical weight and Ω_{ij} is the collision strength given by Equation 2.25.

2.3.3 Collisional Excitation and De-excitation

To determine collisional excitation and de-excitation rates relevant for the thermal pool of electrons, we assume electrons adhere to a Maxwell-Boltzmann distribution. The subsequent "effective" or "Maxwellian-averaged" collisional strength can be calculated for each transition using

$$\Upsilon_{\mathrm{ij}} = \int_0^\infty \Omega_{\mathrm{ij}} e^{-\epsilon_{\mathrm{j}}/kT} d(\epsilon_{\mathrm{j}}/kT) \tag{2.22}$$

where Ω_{ij} is the collisional cross section for an electron to excite the i-j transition, and T is the electron temperature. These collision strengths can be found in the literature and data tables.

The subsequent rates of collisional excitation and de-excitation, respectively, are

$$C_{\mathrm{ij}}(T) = \frac{8.63 \times 10^{-6}}{g_{\mathrm{i}}\sqrt{T}} e^{-E_{\mathrm{ij}}/kT} \Upsilon_{\mathrm{ij}} n_{\mathrm{e}}\ \mathrm{s}^{-1} \tag{2.23}$$

$$C_{\mathrm{ji}}(T) = \frac{g_{\mathrm{i}}}{g_{\mathrm{j}}} e^{E_{\mathrm{ij}}/k_{\mathrm{B}}T} C_{\mathrm{ij}}, \tag{2.24}$$

where E_{ij} is the energy difference between the two levels and $j > i$.

In cases where atomic data for Υ are unavailable, one can use the dipole approximation (Jefferies, 1968; van Regemorter, 1962), which gives results for neutral atoms and positive ions

$$C_{\mathrm{ij}}(T) = \begin{cases} 2.16 f_{\mathrm{ij}} n_{\mathrm{e}} \left[\dfrac{E_{\mathrm{ij}}}{kT}\right]^{-1.68} T^{-3/2} e^{-E_{\mathrm{ij}}/kT}\ \mathrm{s}^{-1}, & \text{(neutral atoms)} \\ 3.9 f_{\mathrm{ij}} n_{\mathrm{e}} \left[\dfrac{E_{\mathrm{ij}}}{kT}\right]^{-1} T^{-3/2} e^{-E_{\mathrm{ij}}/kT}\ \mathrm{s}^{-1}, & \text{(positive ions)}, \end{cases} \tag{2.25}$$

where f_{ij} is the oscillator strength, T is the temperature in Kelvins, E_{ij} is the transition energy in eV, and n_{e} is electron density in cm^{-3}.

In practice, atomic data for Υ_{ij} are often published in a narrow temperature range; for temperatures outside this range, we use the above approximation to fill in the missing data. We scale Equation 2.25 so that there is no discontinuity in C_{ij}.

Forbidden transitions for which atomic data are not available should be treated as a special case, since oscillator strengths for these transitions produce artificially low collisional rates. Axelrod, (1980) provides the following formulation for forbidden transitions (defined as $f_{ij} \leq 0.001$):

$$\Omega_{ij,forb} = \begin{cases} 0.00375\ g_i g_j,\ \lambda \leq 10\ \mu m \\ 0.0225\ g_i g_j,\ \lambda > 10\ \mu m. \end{cases} \tag{2.26}$$

2.3.4 Recombination

Total recombination rates of relevant ions include a sum over all subshells and incorporate both radiative and dielectronic recombination. We assume recombinations involve only ground states, a good approximation in regimes where collisional excitation dominates the population of excited states. We use the rates published in the CHIANTI database v.8 (Del Zanna et al., 2015a; Dere et al., 1997). Although level-specific recombination rates are available for certain ions (e.g., Nahar and Pradhan, 1992, 1994), we opt to use a consistent source for recombination rates for this work. We explore this latter dataset in §3.2.8 and plan to implement state-specific recombination rates in any future work where recombination lines might contribute significantly.

2.3.4.1 Radiative Recombination

Radiative recombination rates are fit to the following form (Aldrovandi and Pequignot, 1973):

$$\alpha_r = A_{rad} T_4^{-X_{rad}}, \tag{2.27}$$

where $T_4 = T/10,000$ K and A_{rad} and X_{rad} are fitting coefficients. Aldrovandi and Pequignot, (1976, 1973) tabulate fitting coefficients for He I, C, N, O, Ne, Mg, Si, and S. Shull and van Steenberg, (1982a) provide coefficients for C, N, O, Ne, Mg, Si, S, Ar, Ca, Fe, and Ni. Arnaud and Rothenflug, 1985b provide updates to the Shull and van Steenberg, (1982a) results for C III-IV, N IV-V, O V-VII, and a number of high-ionization states of Ne, Na, Mg, Al, Si, S, Ar, Ca, Fe, and Ni. Landini and Fossi, (1991a) tabulate coefficients for F, P, Cl, K, Ti, Cr, Mn, and Co in the temperature range 10^5 K $< T < 10^8$ K.

Ground-state recombination fractions for Fe, which are calculated at $T = 10^4 Z_{eff}^2$ (where Z_{eff} is effective charge) and used to account for ionization promptly after recombination, are tabulated in Woods, Shull, and Sarazin, (1981). Similar values for He I, C, N, O, Ne, Mg, Si, and S can be calculated from the table in Aldrovandi and Pequignot, (1973).

An update to radiative recombination rates for Fe XV-XXVI is given by Arnaud and Raymond, (1992b) subject to the following form:

$$\alpha_{\rm r} = AT_4^{\alpha-\beta\log_{10}(T_4)}\ {\rm cm}^3\ {\rm s}^{-1}, \tag{2.28}$$

where $T_4 = T/10,000$ K and A, α, and β are fitting coefficients.

Pequignot, Petitjean, and Boisson, (1991) provide fits to the radiative recombination rates of H, He I, C I-V, N I-VI, O I-VII, and Ne I-IX using the following form:

$$\alpha_{\rm r} = 10^{-13} z \frac{at^b}{1+ct^d}\ {\rm cm}^3\ {\rm s}^{-1}, \tag{2.29}$$

where z is the ionic charge (1 for recombination to neutral state), $t = T_4/z^2$ (for $T_4 = 10,000$ K), and a, b, c, d are fitting coefficients valid for the temperature range $40z^2$ K $< T <$ $4 \times 10^4 z^2$ K.

Verner and Ferland, (1996) provide fits to radiative recombination rates of H-like, He-like, Li-like, and Na-like ions of elements Z = 1 − 30 using the following form:

$$\alpha_{\rm r} = a\left[\sqrt{\frac{T}{T_0}}\left(1+\sqrt{\frac{T}{T_0}}\right)^{1-b}\left(1+\sqrt{\frac{T}{T_1}}\right)^{1+b}\right]^{-1}\ {\rm cm}^3\ {\rm s}^{-1}, \tag{2.30}$$

where a, b, T_0, and T_1 are fitting coefficients, valid for a temperature range of 3 K $< T < 10^{10}$ K. Though this is a large temperature range, this study by Verner and Ferland, (1996) is limited by its ion coverage, missing coefficients for important low-ionization states of elements with Z > 5, including C, O, Fe, Co, and Ni, which are important for modeling SNe Ia in the nebular phase.

Finally, we note that the low-temperature asymptotic behavior of radiative recombination rates is $\alpha_{\rm r} \propto {\rm T}^{-0.5}$ (Ferland et al., 1992), in agreement with the result from Allen, (1963), who report the recombination rate for an ion with ionization level I to be

$$\alpha_{\rm r} = 10^{-13} I^2 T_4^{-0.5}\ {\rm cm}^3\ {\rm s}^{-1}, \tag{2.31}$$

where $T_4 = T/10,000$ K.

2.3.4.2 Dielectronic Recombination

Dielectronic rates are fit to the following form (Aldrovandi and Pequignot, 1973):

$$\alpha_{\rm d} = A_{\rm d} T^{-1.5} e^{-T_0/T}\left(1 + B_{\rm d} e^{-T_1/T}\right)\ {\rm cm}^3\ {\rm s}^{-1}, \tag{2.32}$$

where T is the temperature in Kelvins and $A_{\rm d}$, $B_{\rm d}$, T_0, and T_1 are fitting coefficients. Aldrovandi and Pequignot, (1976, 1973) tabulate fitting coefficients for He I, C, N, O, Ne, Mg, Si, and S. Shull and van Steenberg, (1982a) provide coefficients for C, N, O, Ne, Mg, Si, S, Ar, Ca, Fe, and Ni. Landini and Fossi, (1991a) tabulate coefficients for F, P, Cl, K, Ti, Cr, Mn, and Co in the temperature range 10^5 K $< T < 10^8$ K.

Arnaud and Rothenflug, (1985b) provide updates to the Shull and van Steenberg, (1982a) results for O VII, Mg XI, Ca XIX, and Fe XXV.

Dielectronic recombination rates for C, N, O, Ne, Mg, Al, and Si are given by Nussbaumer and Storey, (1983, 1984, 1986, 1987) subject to the following form:

$$\alpha_{\rm d} = 10^{-12} T_4^{-1.5} \left(\frac{a}{T_4} + b + cT_4 + dT_4^2 \right) e^{-f/T_4} \text{ cm}^3 \text{ s}^{-1}, \tag{2.33}$$

where a, b, c, d, and f are fitting coefficients and $T_4 = T/10,000$ K.

Dielectronic recombination rates for Fe XV-XXVI are given by Arnaud and Raymond, (1992b) subject to the following form:

$$\alpha_{\rm d} = T^{-1.5} \sum_{\rm i} c_{\rm i} \exp^{-E_{\rm i}/kT} \text{ cm}^3 \text{ s}^{-1}, \tag{2.34}$$

where $c_{\rm e}$ and $E_{\rm i}$ are fitting coefficients and T is the temperature in Kelvins. Mazzotta et al., (1998) tabulate these fitting coefficients for Z = 1 − 28.

More recent work has focused on publishing fitting coefficients to the above fitting formulae and collecting them into a consistent database for the community to use. In particular, the CHIANTI database[1] (Del Zanna et al., 2015b) incorporates new dielectronic recombination rates from Abdel-Naby et al., (2012), Altun et al., (2004, 2006, 2007, 2005), Badnell, (2006), Bautista and Badnell, (2007), Colgan, Pindzola, and Badnell, (2004, 2005), Colgan et al., (2003), Mitnik and Badnell, (2004), Nikolić et al., (2010), and Zatsarinny et al., (2003, 2005a,b, 2006, 2004), while maintaining the results of Mazzotta et al., (1998) and Shull and van Steenberg, (1982a) whenever newer rates are not available.

2.3.4.3 Unified Recombination

In the unified approach to ionization (Pradhan and Nahar, 2011, p. 123), radiative recombination and dielectronic recombination (RR and DR, respectively) are treated with a single rate as long as the bound-free cross sections capture the resonances due to autoionization processes. The recombination coefficient is typically defined using the free-bound cross-section integrated over the electron energy distribution, which assumes a Maxwell-Boltzmann distribution,

$$\alpha_{\rm i}(T) = \frac{4}{\sqrt{2\pi m}} (kT)^{-3/2} \int_0^\infty \epsilon e^{-\epsilon/kT} \sigma_{\rm fb,i} d\epsilon \text{ cm}^3 \text{ s}^{-1}. \tag{2.35}$$

Using the Milne relation (Rybicki and Lightman, 1979, p. 285), we can to relate the bound-free and free-bound cross-sections,

$$\frac{\sigma_{\rm bf}}{\sigma_{\rm fb}} = \left(\frac{m_{\rm e} c v_{\rm e}}{h\nu} \right)^2 \frac{g_{\rm e} g_{\rm ion}}{2 g_{\rm i}}, \tag{2.36}$$

where $g_{\rm e}$, $g_{\rm ion}$, and $g_{\rm i}$ are the statistical weights of electrons, the upper ion's ground state, and the i-th level (respectively), and $m_{\rm e}$ and $v_{\rm e}$ are the electron's mass and velocity (respectively).

[1] http://chiantidatabase.org/

Using the relation for excess electron energy $\epsilon = h\nu - \chi$, we arrive at the desired recombination coefficient from the ground state of the ion to the i-th level of the lower ion,

$$\alpha_{\rm i}(T) = 8.186 \times 10^{-11} \frac{g_{\rm i}}{g_{\rm ion}} T^{-3/2} \int_0^\infty (\epsilon + \chi_{\rm i})^2 e^{-\epsilon/kT} \sigma_{\rm bf,i} d\epsilon \ {\rm cm}^3 \ {\rm s}^{-1}, \tag{2.37}$$

where $\sigma_{\rm bf,i}$ and $\chi_{\rm i}$ are the unified photoionization rate (in Mb) and ionization potential (in eV) for level i, respectively, and energies ϵ are in eV. Finally, we can write the recombination rate as

$$R_{\rm rec} = n_{\rm e} \alpha_R(T) \ {\rm s}^{-1}. \tag{2.38}$$

In order to calculate NLTE level populations, we need the total (RR + DR) recombination rates to each atomic level. They can be calculated using Equation 2.37, or taken from published sources. For Fe, we use the sophisticated results of NORAD (Nahar, 1997, 1996; Nahar, Bautista, and Pradhan, 1998, 1997). For all other species, we take total recombination rates from CHIANTI (Dere et al., 2009) and estimate level-specific recombination rates based on statistical weighting. This method will give accurate ionization balance but may produce some unrealistic line emission in extreme cases. Future efforts should update recombination rates to the best available.

Photoionization cross-sections are available from a number of resources; in this work, we take them from TOPbase (Cunto et al., 1993; Palmeri and Mendoza, 2005). For missing atomic data, we use the hydrogenic approximation of Kramers, (1923):

$$\sigma_{\rm hyd} = 7.9 \bar{g} \frac{Z_{\rm eff}^4}{n_{\rm eff}^5} E_{\rm ryd}^{-3} \ {\rm Mb} \tag{2.39}$$

where $E_{\rm ryd}$ is the photon energy in Rydbergs. We use a different effective charge ($Z_{\rm eff}$) and effective quantum number ($n_{\rm eff}$) for each atomic level as described by Slater, (1930). We assume the gaunt-factor $\bar{g}$ is unity.

The above procedure has been carried out by a number of groups, resulting in the availability of various approximations for which best-fit parameters are available (Allen, 1963; Arnaud and Raymond, 1992a; Arnaud and Rothenflug, 1985a; Landini and Fossi, 1991b; Landini and Monsignori Fossi, 1990; Shull and van Steenberg, 1982b). The reader should note that in earlier work, radiative recombination and dielectronic recombination were reported separately.

2.3.4.4 Three-body (Collisional) Recombination

We use the result derived in Jefferies, (1968) for collisional recombination from the ground state of the upper ion to the i-th level of the lower ion,

$$R_{\rm rec,3b} = n_{\rm e} \alpha_{\rm 3b,i} \approx 5.6 \times 10^{-16} \zeta n_{\rm e}^2 \left[\frac{E_0}{kT} \right]^{-2} T^{-3} \frac{g_{\rm i}}{Z_+} \ {\rm s}^{-1}, \tag{2.40}$$

where ζ is the number of valence electrons, $g_{\rm i}$ is the statistical weight of the i-th level, Z_+ is the partition function of the upper ion, and electron density has units $[n_{\rm e}] = {\rm cm}^{-3}$. As this process requires two electrons, it is rare except in plasmas of high electron density.

2.3.5 Ionization

A number of ionizing processes can be important in low-density plasmas. In particular, radiation fields can photoionize atoms, free electrons can ionize by impact due to their thermal motion, and radioactive decay can produce high-energy leptons that ionize by impact in addition to heating the gas.

2.3.5.1 Photoionization and Autoionization

For most species, we use bound-free cross-sections provided by the CMFGEN atomic database, which collects a large part of its cross-sections from the Iron Project (Hummer et al., 1993). The cross-sections published by the Iron Project include resonances to account for autoionization processes, and consequently we treat these processes as one and derive the following ionization rate from the i-th level to the ground state of the subsequent ion,

$$R_{\rm pi} = 4\pi \int_{\nu_{\rm i}}^{\infty} \frac{J_\nu}{h\nu} \sigma_{\rm bf}(\nu) d\nu, \tag{2.41}$$

where $\nu_{\rm i}$ is the threshold frequency corresponding to the ionization potential of the i-th level, $\sigma_{\rm bf}$ is the bound-free cross-section that includes autoionization resonances, and J_ν is the average radiation field. This is a general equation that can be used for any arbitrary radiation field.

2.3.5.2 Collisional Ionization

Collisional ionization cross-sections are directly used in the calculation of non-thermal deposition fractions. Ionization cross sections for this work are taken from Mattioli et al., (2007) and Dere, (2007), which update the work of Lotz, (1969), Shull and van Steenberg, (1982b), Arnaud and Rothenflug, (1985a), Arnaud and Raymond, (1992a), and Mazzotta et al., (1998).

Given a distribution of electron energies, it is possible to determine collisional ionization rates using the above cross-sections (Younger, 1981). For an electron gas with arbitrary energy distribution f(E), the collisional ionization rate is

$$C_{\rm ic} = \int_{\chi}^{\infty} n_{\rm e} v_{\rm e} Q(E) f(E) dE, \tag{2.42}$$

where χ is the ionization potential of the ion.

For the thermal pool of electrons, we have used the analytical fits for $C_{\rm ic}$ from Voronov, (1997). Although these rates are limited to certain temperature ranges, this data-set is

consistently used in the literature. As a backup, we may also use the approximations documented in Jefferies, (1968):

$$C_{\rm ic} \approx 2.7\ \zeta n_{\rm e} \left[\frac{E_0}{kT}\right]^{-2} T^{-3/2} e^{-E_0/kT}\ {\rm s}^{-1}, \tag{2.43}$$

where ζ is the number of valence electrons, E_0 is the ionization potential of the desired level, T is in Kelvins, and electron density has units $[n_{\rm e}] = {\rm cm}^{-3}$.

2.3.6 Spontaneous Emission

Spontaneous emission from between atomic levels is responsible for the features seen in nebular spectra. Transition rates can be found in data tables in a number of formats, the most common being Einstein A coefficients ($A_{\rm ji}$) and oscillator strengths ($f_{\rm ij}$). The relation between these two is

$$f_{\rm ij} = 1.245 \times 10^{-10} \left(\frac{E_{\rm ij}}{\rm Ryd}\right)^{-2} \frac{g_{\rm j}}{g_{\rm i}}\ A_{\rm ji}, \tag{2.44}$$

where $g_{\rm i}$ and $g_{\rm j}$ are statistical weights and $j > i$.

2.3.7 Stimulated Absorption and Emission

If the gas is subject to a non-negligible radiation field, it is necessary to include transitions stimulated by the presence of photons. The rates for these processes are characterized by the Einstein B coefficients, which are related to the Einstein A coefficients by

$$B_{\rm ji} = \frac{c^2}{2h\nu_{\rm ij}^3} A_{\rm ji} \tag{2.45}$$

$$B_{\rm ij} = \frac{g_{\rm j}}{g_{\rm i}} B_{\rm ji}, \tag{2.46}$$

where $g_{\rm i}$ and $g_{\rm j}$ are statistical weights and $j > i$, and $\nu_{\rm ij}$ is the frequency associated with the energy difference of the transition.

The rate of transitions is related to the strength of the radiation field present. For an arbitrary radiation field,

$$\bar{J} = \int_0^\infty J_\nu \phi(\nu - \nu_0) d\nu \approx J_\nu(\nu_0), \tag{2.47}$$

where J_ν is the angle-averaged intensity and ϕ is the profile function of the transition. If the transition is relatively narrow compared to the changes in the radiation field, we can approximate ϕ as a δ-function and evaluate the function at that wavelength, as we have done in the above equation (Rybicki and Lightman, 1979).

We can thus write the stimulated emission and absorption rates (respectively) as

$$R_{\rm ji,stim} = \bar{J}B_{\rm ji} \quad (2.48)$$
$$R_{\rm ij,stim} = \bar{J}B_{\rm ij}. \quad (2.49)$$

Another approximation is the so-called "g-bar" approximation (Mewe and Gronenschild, 1981),

$$\Upsilon_{\rm ij} = \frac{8\pi}{\sqrt{3}} f'_{\rm gj} \bar{g}(T) \quad (2.50)$$
$$\bar{g}(x) = A + e^x(Bx - Cx^2 + Dx^3 + E)E_1(x) + (C + D)x - Dx^2 \quad (2.51)$$

where f', A, B, C, D, and E are parameters tabulated in Mewe and Gronenschild, (1981) and $E_1(x)$ is the first exponential integral.

Chapter 3

1D Nebular Modeling of Type Ia Spectra

3.1 Introduction

Spectra taken of supernovae at late times (in the nebular phase, $\gtrsim 100$ days after explosion) probe the central regions of the ejecta and thus contain a wealth of information about the explosion, such as nucleosynthetic yields, compositional mixing, and geometry. The quantity and breadth of nebular spectra has grown rapidly in recent years owing to international observational efforts. However, further modeling is needed to develop a systematic understanding of how nebular spectra depend on explosion parameters and how atomic data inputs affect spectral modeling.

The aim of this chapter is to systematically study how variations in explosion properties, density and abundance structure, and atomic data inputs affect the spectra of SNe Ia at late times. To that end, we present a new NLTE code to model the nebular spectra of supernovae. In Chapter 2, we have presented our method of calculating level populations, non-thermal deposition, temperature and ionization balance, and nebular spectra. In §3.1, we use a fiducial model to describe the physics of nebular spectral formation in SNe Ia. We then vary the parameters of the model to probe the sensitivity of the spectra to ejecta mass, composition, and kinetic energy (§3.2.1-3.2.6), as well as density profile (§3.2.7) and atomic data inputs (§3.2.8).

To study the nebular spectra of SNe Ia, we construct spherically symmetric models in which the ejecta properties (e.g., total mass, energy, and abundances) are free parameters. We first describe the general properties of spectrum formation in a "fiducial" model that resembles the ejecta structure expected for normal SNe Ia. In §3.2 we carry out a parameter survey that demonstrates how the nebular spectra depend on explosion properties.

3.1.1 Ejecta Modeling

We model the ejecta with a broken power-law density profile which is shallow in the core and steep in the outer layers (Chevalier and Soker, 1989; Kasen, 2010).

$$\rho(v) = \begin{cases} \rho_0 \left(\frac{\mathrm{v}}{\mathrm{v_t}}\right)^{-\delta} & \mathrm{v} \leq \mathrm{v_t} \\ \rho_0 \left(\frac{\mathrm{v}}{\mathrm{v_t}}\right)^{-\mathrm{n}} & \mathrm{v} > \mathrm{v_t}, \end{cases} \tag{3.1}$$

where ρ_0 can be interpreted as the central density of a perfectly flat core profile ($\delta = 0$) and v_t is the transition velocity marking the interface of the two regions. Integration gives (assuming $\delta < 3$ and $\mathrm{n} > 3$)

$$\rho_0 = \frac{\mathrm{M_{ej}}}{4\pi(\mathrm{v_t t_{ex}})^3} \left[\frac{1}{3-\delta} + \frac{1}{\mathrm{n}-3}\right]^{-1} \tag{3.2}$$

$$\mathrm{E_K} = \frac{1}{2}\mathrm{M_{ej} v_t^2} \left[\frac{1}{5-\delta} + \frac{1}{\mathrm{n}-5}\right] \left[\frac{1}{3-\delta} + \frac{1}{\mathrm{n}-3}\right]^{-1}, \tag{3.3}$$

where M_ej is the total ejecta mass, E_k is the ejecta kinetic energy, and t_ex is the time since explosion. The radial density profile is thus completely set by the choice of M_ej, E_k, and the exponents δ, n. In our calculations, we cut off the model at a radius that encompasses 99% of the total ejecta mass.

We find that the values $\delta = 0$, $\mathrm{n} = 10$ give reasonable fits to the nebular spectra of SNe Ia, and so use these values for our fiducial model. In this case, the characteristic velocity and density scales are

$$\mathrm{v_t} = 10,943\ \mathrm{E_{51}^{1/2}\ M_1^{-1/2}\ km\ s^{-1}} \tag{3.4}$$

$$\rho_0 = 4.90 \times 10^{-17}\ \mathrm{E_{51}^{-3/2}\ M_1^{5/2}\ t_{200}^{-3},\ g\ cm^{-3}} \tag{3.5}$$

where $M_1 = M_\mathrm{ej}/M_\odot$, E_{51} is the kinetic energy in units of 10^{51} erg, and t_{200} is the time since explosion scaled to 200 days. We explore using different power-law exponents, as well as an exponential density profile, in §3.2.7.

The compositional structure of the ejecta models is assumed to be stratified into three distinct zones (Woosley et al., 2007). The center of the ejecta is assumed to consist of stable iron-group elements (IGEs) of mass M_IGE. The stable IGEs are assumed to be composed of a ratio, R_stb, of ^{54}Fe to ^{58}Ni. Surrounding the stable IGE region is a zone consisting (initially) mostly of ^{56}Ni of mass $M_{^{56}\mathrm{Ni}}$. We include a small amount of stable IGEs in this region with mass abundance X_stb and the same isotopic ratio R_stb. Above the ^{56}Ni is an outer layer of intermediate-mass elements (IMEs) of mass M_IME. We compose the IME layer of 70% ^{28}Si, 29% ^{32}S, and 1% ^{40}Ca, roughly consistent with the nucleosynthetic results in the SN Ia explosion models of Plewa, (2007) and Seitenzahl et al., (2013). We study

the presence of unburned C/O mixed into the nickel zone and IME layer in §3.2.6. The parameters describing the masses of the elements are constrained to add to the total ejecta mass.

The total radioactive energy deposition rate (and hence bolometric luminosity) of a model depends not only on $M_{56\mathrm{Ni}}$ but also on the efficiency of the trapping of radioactive decay products. Since the ejecta are largely transparent to gamma rays at nebular phases, the gamma-ray trapping fraction is $f_{\gamma,\mathrm{c}} = 1 - \mathrm{e}^{-\tau_\gamma} \approx \tau_\gamma$, where τ_γ is the mean optical depth to gamma-rays. Taking a typical gamma-ray opacity $\kappa_\gamma \approx 0.03$ cm^2 g^{-1} (Swartz, Sutherland, and Harkness, 1995) and integrating the radial optical depth from the center ($r = 0$) gives an estimate

$$f_{\gamma,\mathrm{c}} \approx 0.025\ E_{51}^{-1}\ M_1^2\ t_{200}^{-2}. \tag{3.6}$$

Equation 3.6 presumably overestimates the gamma-ray trapping fraction (since τ_γ is evaluated at $r = 0$), but the scaling of $f_{\gamma,\mathrm{c}}$ with M_{ej}, E_{K}, and t will be useful for interpreting how the radioactive deposition rate depends on physical parameters.

3.1.2 Fiducial Model

To describe the basic features of nebular spectrum formation, we present first a fiducial model with parameters (given in Table 3.1) typical of standard SN Ia explosion models, i.e., M_{ej} near the Chandrasekhar mass and $M_{56\mathrm{Ni}} = 0.6\ M_\odot$. The fiducial model has a transition velocity of $10,131$ km s^{-1} while the interface between the nickel zone and IME layer is near $8,800$ km s^{-1}.

t_{ex} (days)	200
M_{ej} ($M_\odot$)	1.40
E_{K} (10^{51} erg)	1.2
$M_{56\mathrm{Ni}}$ ($M_\odot$)	0.6
M_{stb} ($M_\odot$)	0.0
X_{stb}	0.05
R_{stb}	1.0
M_{IME} ($M_\odot$)	0.75
M_{CO} ($M_\odot$)	0.0

Table 3.1: Fiducial model parameters. M_{stb} refers to the mass of the stable IGE region in the core of the explosion, X_{stb} is the mass fraction of stable IGE material mixed into the ^{56}Ni region, R_{stb} is the ratio of ^{54}Fe/^{58}Ni in both core stable IGE and ^{56}Ni regions, M_{IME} is the total mass of the IME layer, and M_{CO} is the mass of C/O mixed throughout the ejecta.

Figure 3.1 shows our calculation of the synthetic nebular spectrum of the fiducial model at 200 days after explosion. We compare to the observed spectrum of the well-studied nearby

Type Ia SN 2011fe (Mazzali et al., 2015; Nugent et al., 2011; Shappee et al., 2013). The model spectrum reproduces most but not all of the prominent features, as will be discussed below.

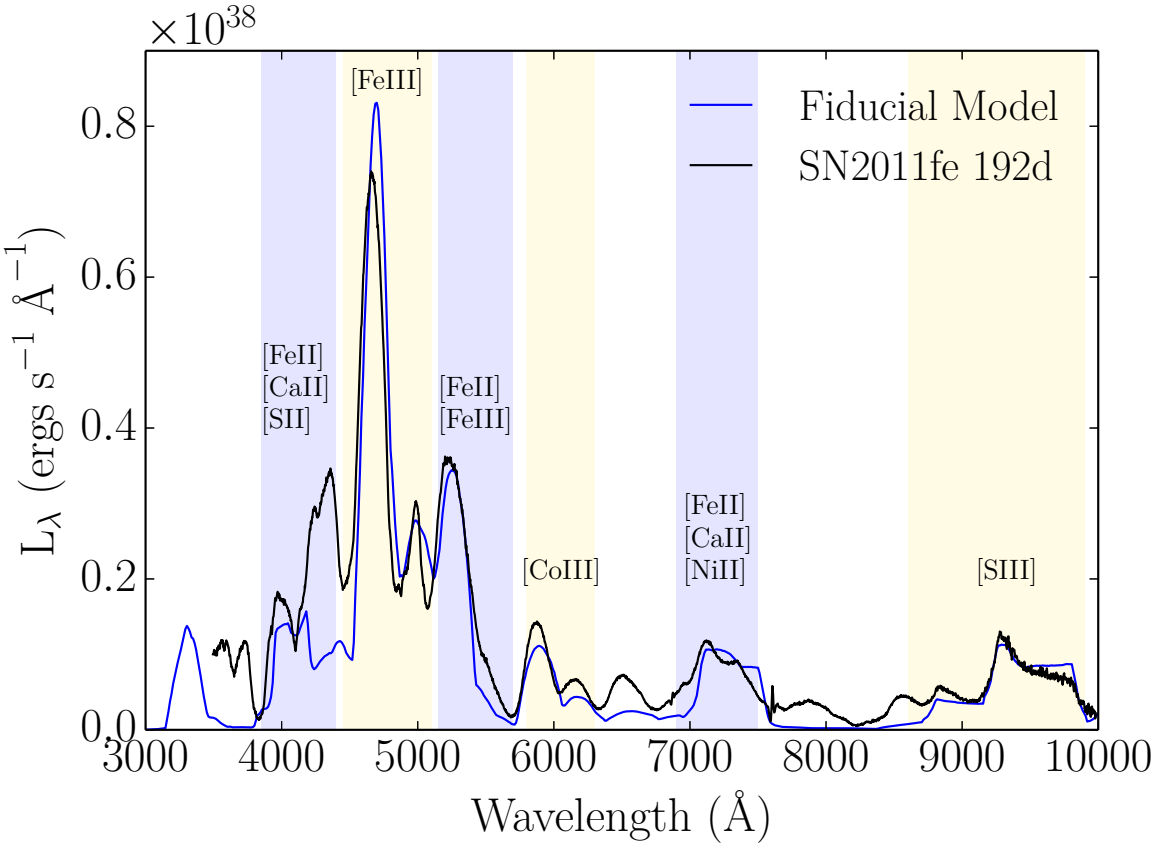

Figure 3.1: Synthetic spectrum of the fiducial SN Ia model (at 200 days after explosion) compared to SN 2011fe at 192 days (Mazzali et al., 2015).

Figure 3.2 shows a breakdown of the contribution from various ions to the fiducial model spectrum. The strongest features are due to forbidden transitions of Fe II and Fe III which are collisionally excited in the nickel zone. Emission due to IME lines is also visible at redder wavelengths. Most of the important individual line transitions are listed in Table 3.2.

The spectrum in the nebular phase forms primarily from the collisional excitation of ions by thermal electrons, followed by spontaneous de-excitation via the emission of a line photon. Given the relatively low ejecta temperatures, electrons can only excite low-lying atomic levels, among which radiative transitions are typically electron dipole forbidden (see Table 3.2). Nevertheless, the rate of collisional de-excitations is generally so small in the

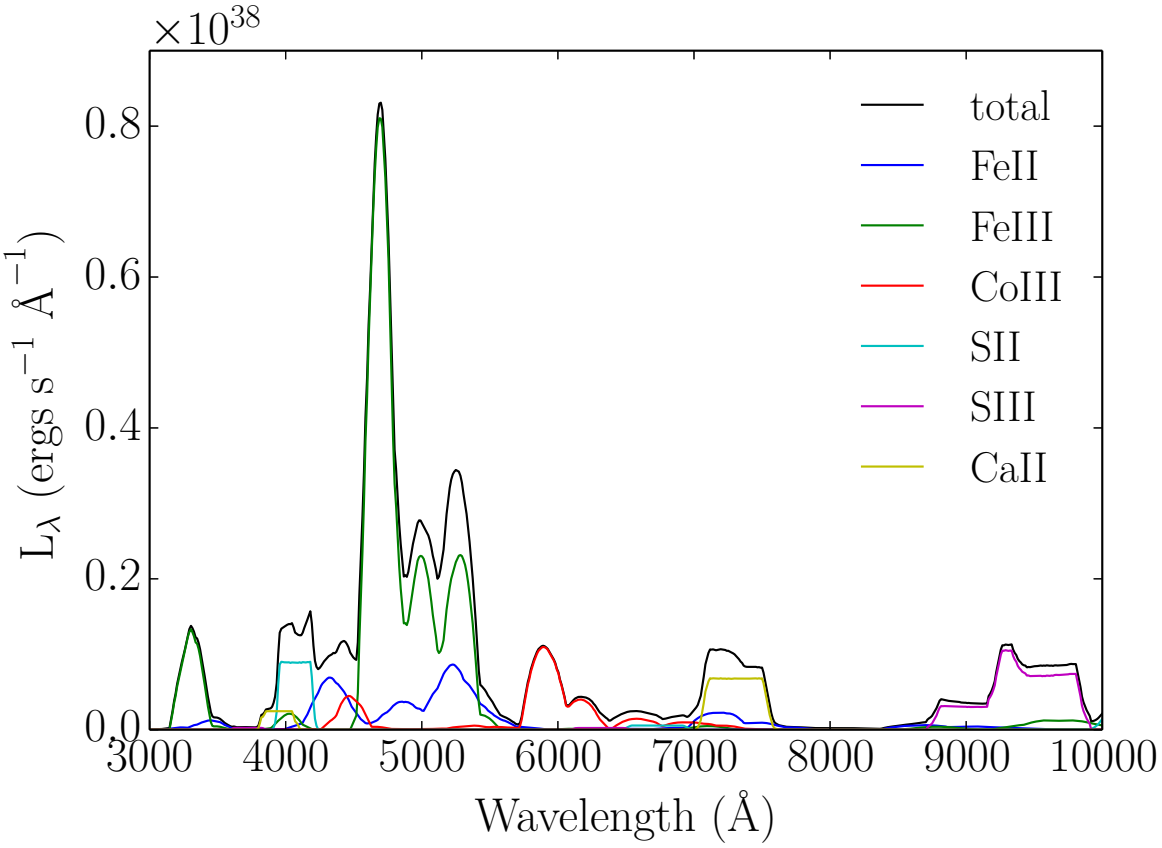

Figure 3.2: Fiducial model spectrum decomposed into the emission from individual ions. Forbidden transitions of Fe III dominate the spectrum, along with some forbidden Fe II, Co III, Ca II, S II, and S III features.

low-density nebula that essentially every collisional excitation eventually leads to radiative emission through a forbidden line.

The temperature of the ejecta is determined by the balance of radioactive heating and cooling by line emission. Figure 3.3 shows the radioactive heating rate and temperature for the fiducial model. The interior ejecta density profile is flat in this model, and so the ejecta temperature is nearly constant at $T \approx 9000$ K in the inner layers. Above the radioactive nickel zone, the temperature drops owing to the declining heating rate, but increases again in the very low-density outermost layers because of the inability of the ejecta to cool efficiently.

The important emission lines appearing in the nebular spectra depend on the composition and ionization state of the ejecta. In SNe Ia, ionization is primarily caused by the non-thermal electrons produced by radioactive decay (the collisional ionization rate from thermal electrons is subdominant), which is balanced by radiative recombination. Figure 3.3 shows

the radial dependence of the ionization fractions of iron for the fiducial model. Though Fe IV and Fe V are the most abundant ions, they lack low-lying levels that are able to be excited by the thermal electrons. Thus, the most prominent lines are produced by Fe III and Fe II.

As a comparison, we also run a model with same parameters as the fiducial model but with an exponential density profile similar to the commonly-used W7 model (Nomoto, Thielemann, and Yokoi, 1984; Thielemann, Nomoto, and Yokoi, 1986). Specifically, we use $\rho = \rho_0 e^{-v/v_e}$, where ρ_0 and v_e are set by total ejecta mass, kinetic energy, and time since explosion. We show the calculated ejecta properties in Figure 3.4. Higher central density in this model results in higher gamma-ray deposition overall. In general, the degree of ionization increases as the density declines at higher velocities, reflecting the reduced rate of radiative recombination. For the same reason, the overall ionization state of iron is lower in the W7-like model owing to higher overall densities. See §3.2.7 for synthetic spectra of this model and a systematic study of density profiles.

As a more comprehensive description of SN Ia nebular spectra, we discuss the features appearing in each key wavelength region seen in Figure 3.1.

3500-4500 Å: This region contains emission from [SII] and [Fe II] transitions. Similar to other studies (e.g., Friesen et al., 2017; Mazzali et al., 2015), our model fails to reproduce all of the observed features, which could be a result of ions missing in the model, uncertainties or incompleteness of the atomic line data, or the neglect of optical depth effects that may produce a pseudo-continuum at the bluest wavelengths. There is some evidence that [Fe II] emission at 4400 Å contributes to this feature in SN 2011fe (Friesen et al., 2017).

4500-5500 Å: This region is dominated by emission from [Fe III], which produces prominent features at 4658 Å and 5270 Å. The latter feature also includes a significant contribution from [Fe II] 5159 Å; therefore, the ratio of these two lines is a diagnostic of the ionization state of the gas. The small emission line appearing between the two strong lines is produced by [Fe III] 5011 Å, and can be washed out if the ejecta velocities are too high.

5500-7000 Å: This region contains a prominent [Co III] feature near 5888 Å with two smaller [Co III] features immediately to the red. The line strength depends on the abundance and ionization state of cobalt, and typically declines with time as ^{56}Co decays to ^{56}Fe. The feature near 6500 Å is not well fit by our model (or by previous models; e.g., Mazzali et al., 2015). Because stripped hydrogen from a nondegenerate companion should have velocities $\lesssim$ 1000 km s^{-1} (e.g., Marietta, Burrows, and Fryxell, 2000), this emission is unlikely to be due to Hα. The identification of the feature and the reason for the poor fit are thus unclear.

7000-7700 Å: The feature in this region is a blend of multiple [Fe II] lines and a broad [Ca II] line. In addition, [Ni II] emission can contribute if sufficient stable ^{58}Ni is present in the gas, but for our fiducial model [Ni II] does not dominate this feature. Notably, the fiducial model only contains 0.0075 $M_\odot$ of calcium and yet [Ca II] emission from the IME layer dominates the emission in this region.

8500-11,000 Å: This region is made up primarily of [S II] and [S III] emitted by the 0.22 $M_\odot$ of sulfur in the IME layer above the nickel zone. The broad, flat-topped profiles of IMEs are caused by their large velocities and absence of IMEs in the core.

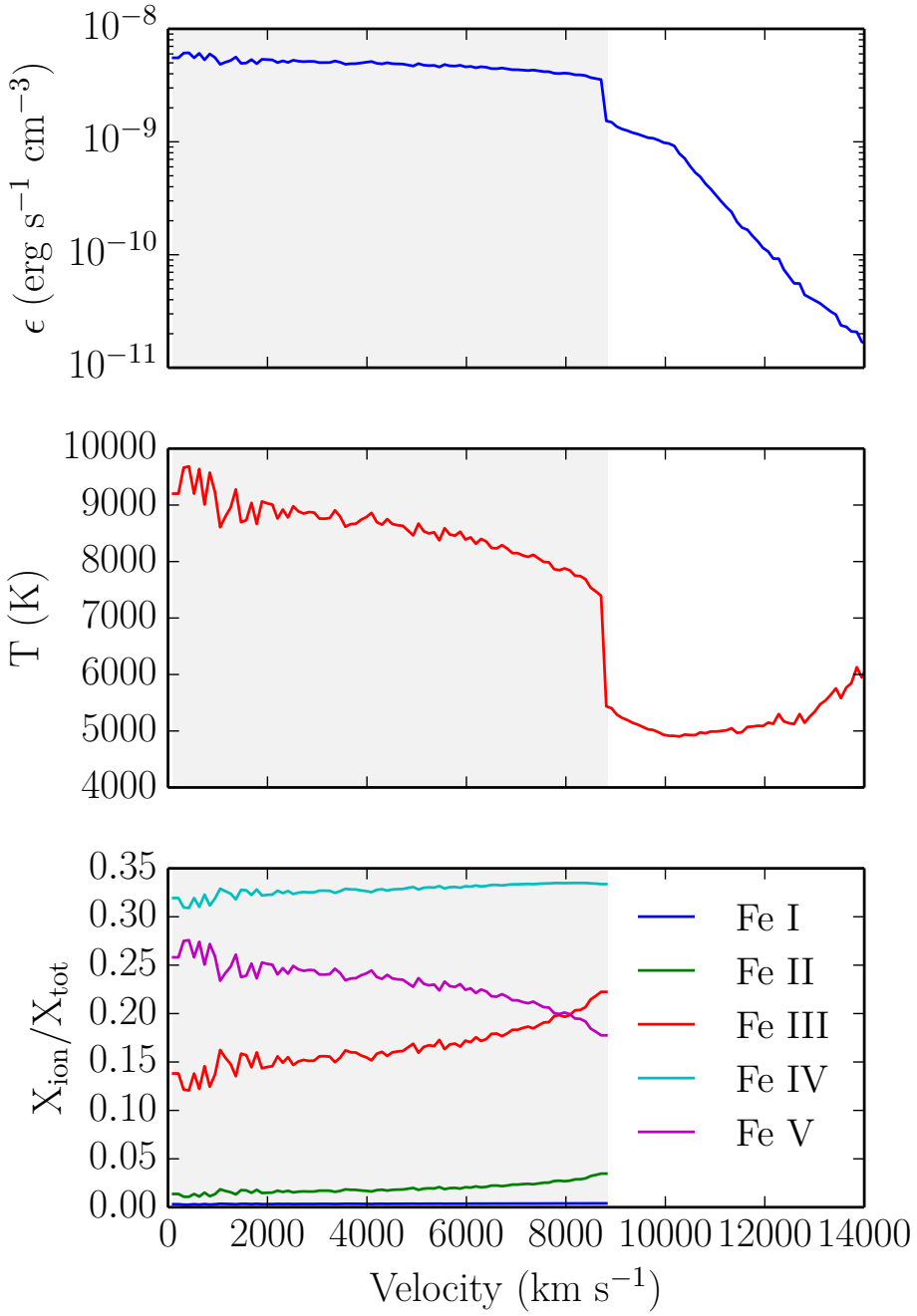

Figure 3.3: Calculated ejecta properties of the fiducial model, which has a flat interior density profile. The top panel shows the energy deposition rate from ^{56}Co decay, including gamma-ray and positron channels. The middle panel shows the calculated temperature based on the balance of ^{56}Co heating and line cooling. The bottom panel shows the ionization fractions of Fe I-V. The discontinuity at $\sim$8800 km s^{-1} is due to the interface between the nickel zone and IME layer.

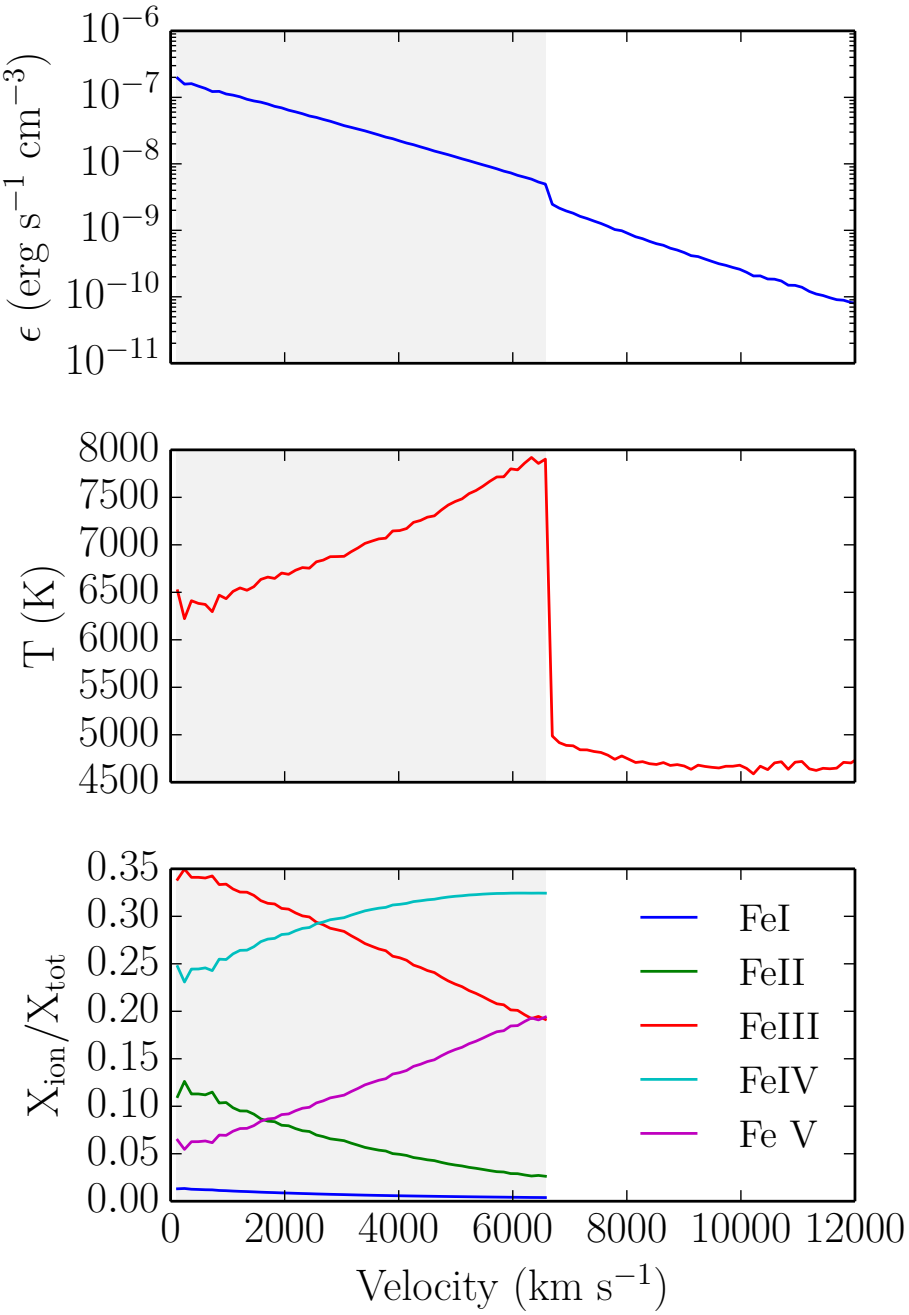

Figure 3.4: Same as Figure 3.3 but with a W7-like exponential density profile (see text for description). The discontinuity at ∼6500 km s^{-1} is due to the interface between the nickel zone and IME layer.

3.2 Systematic Parameter Study

We present the following systematic study probing the sensitivity of synthetic nebular spectra to model parameters and atomic data inputs. In particular, we calculate how the spectra depend on the total ejecta mass, kinetic energy, ^{56}Ni mass, and time since explosion, as well as on density and compositional structure. A full list of models and their derived properties is shown in Table 3.2.

3.2.1 Time Since Explosion

Figure 3.5 shows the nebular spectrum of the fiducial model at times between 200 and 400 days after explosion. As the supernova evolves in time, ejecta densities decline and radioactive isotopes decay. The bolometric luminosity drops with time owing to the declining radioactive heating and a decreasing gamma-ray trapping fraction. The relative strength of prominent Fe lines does not evolve significantly, indicating that the Fe III/Fe II ionization ratio remains fairly constant over time. However, as gamma-ray trapping becomes inefficient at late times, the relative strength of IME features to IGE features decreases.

The biggest relative change in the spectral features over time (see inset) is the strength of the [Co III] emission at 5888 Å, which decreases as ^{56}Co decays to ^{56}Fe. This behavior has been seen in observations and exploited to derive explosion properties such as ^{56}Ni mass and total ejecta mass (Childress et al., 2015). In addition, the declining gamma-ray deposition in the IME layer results in lowered relative strength of IME features.

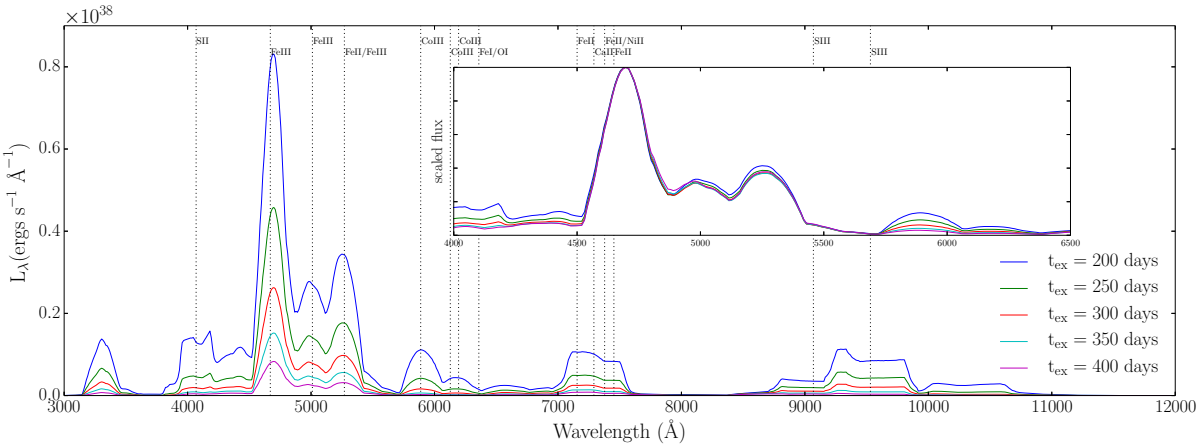

Figure 3.5: Synthetic spectra of the models with varying time since explosion. The inset shows all fluxes scaled to the peak of the 4658 Å feature. Vertical dotted lines identify the source of some prominent transitions. Over time, the bolometric luminosity declines owing to decreased energy deposition, and the [Co III] 5888 Å feature becomes weaker because of the decay of radioactive ^{56}Co.

3.2.2 Explosion Kinetic Energy

The amount of kinetic energy ($E_{\rm K}$) imparted to the ejecta by a supernova explosion depends on the nucleosynthetic yields and initial binding energy (Woosley et al., 2007). The typical energy of SNe Ia is around a Bethe ($1{\rm B} = 10^{51}$ erg). Various theoretical models have predicted kinetic energies in the range $0.87 - 1.6$ B (Bravo et al., 2009; Gamezo, Khokhlov, and Oran, 2005; Golombek and Niemeyer, 2005; Jordan et al., 2012, 2008; Plewa, 2007; Röpke and Niemeyer, 2007; Röpke et al., 2007).

Figure 3.6 shows synthetic spectra of the fiducial model with $E_{\rm K}$ varied between $1 - 2$ B. The lower $E_{\rm K}$ models are more efficient at trapping radioactive energy (owing to the higher ejecta density, Eq. 3.5) and so have higher bolometric luminosities.

Changing $E_{\rm K}$ has a modest effect on the shape of the spectral features. An increase of $E_{\rm K}$ from 1 B to 1.4 B increases the velocity scale by only 18%, which results in a subtle increase in the line widths (as these widths are also set in part by line blending). A larger change of $E_{\rm K}$ by a factor of 2 (from 1 B to 2 B) does have noticeable effects, causing the [Fe III]/[Fe II] complex to be so blended that the small central emission near 5000 Å becomes indistinguishable. Observations of this small feature may therefore be a useful diagnostic of the velocity of the nickel zone in SNe Ia.

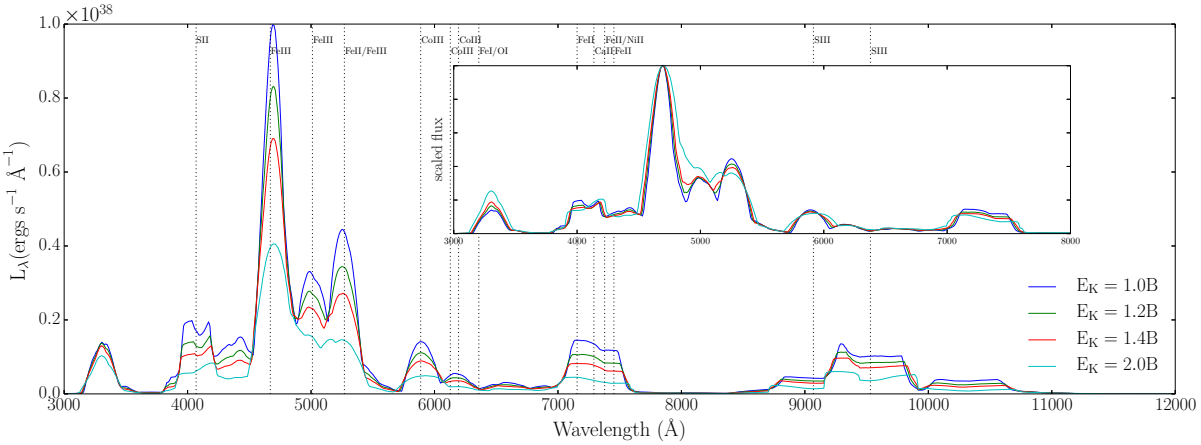

Figure 3.6: Same as Figure 3.5 but for the $E_{\rm K}$ parameter study. Increasing $E_{\rm K}$ produces slightly wider line profiles, eventually washing out features like the [Fe III] emission at 5011 Å. Bolometric luminosity drops as higher $E_{\rm K}$ models have decreased energy deposition.

3.2.3 Total Ejecta Mass

Theoretical models of SNe Ia predict an ejected mass in the range $0.8 - 2.0\ M_{\odot}$, depending on the progenitor scenario. Approximate light-curve modeling studies have suggested that

observed SNe Ia could span this entire range (Scalzo, Ruiter, and Sim, 2014; Scalzo et al., 2010; Scalzo et al., 2014; Stritzinger et al., 2006).

Figure 3.7 shows synthetic spectra of the fiducial model with $M_{\rm ej}$ varied in the range $1 - 2\ M_{\odot}$. For a fixed kinetic energy, a higher $M_{\rm ej}$ results in higher ejecta densities and lower velocities. As a result, higher $M_{\rm ej}$ models have greater gamma-ray trapping, a brighter bolometric luminosity, and less Doppler broadened spectral features. This effect of $M_{\rm ej}$ is therefore somewhat degenerate with that of kinetic energy.

The relative features in the synthetic spectra of Figure 3.7 show only subtle variations with $M_{\rm ej}$. For our super-$M_{\rm Ch}$ case with $M_{\rm ej} = 2.0\ M_{\odot}$, the IME features become visibly stronger owing to the higher total IME mass. The [Fe III]/[Fe II] line ratio also decreases because of the increased rate of recombination at higher densities.

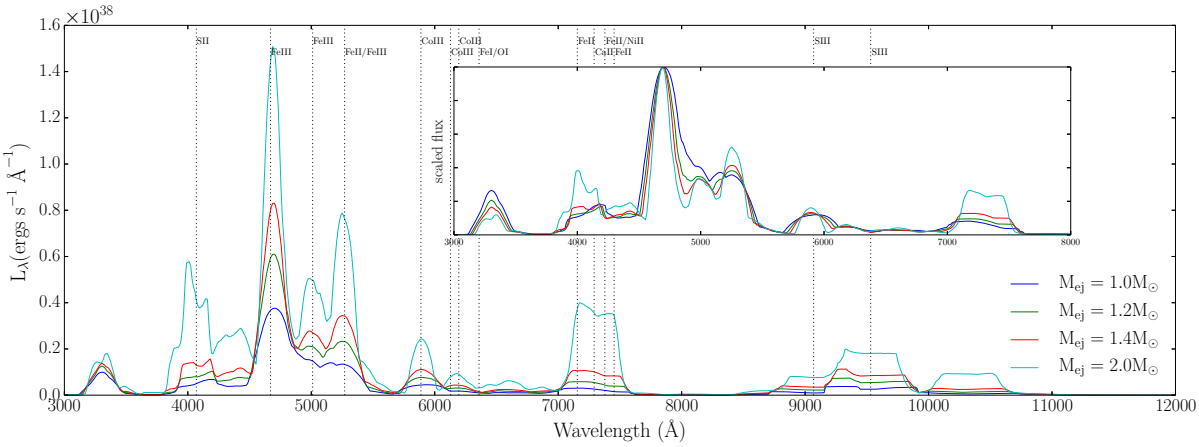

Figure 3.7: Same as Figure 3.5 but for the $M_{\rm ej}$ parameter study (kinetic energy and ^{56}Ni mass are held fixed). Increasing the total ejecta mass results in higher IME emission around 4000 Å, 7300 Å, and 9500 Å given that those models have higher IME masses by construction. The effect of reducing $M_{\rm ej}$ is largely degenerate with increasing the kinetic energy (Figure 3.6), with a low ejecta mass producing a highly-blended feature around 5007 Å.

While we have studied the effect of varying ejecta mass alone in Figure 3.7, this parameter is likely correlated with kinetic energy and ^{56}Ni mass (Woosley et al., 2007); for example, a super-$M_{\rm Ch}$ explosion is likely to produce more ^{56}Ni and higher kinetic energy. We therefore ran three additional models in which we fixed the ratios $\rm M_{56Ni}/M_{ej} = 1/2$ and $\rm E_{51}/M_{ej} = 1.2/1.4$. Based on the above discussion of gamma-ray trapping (§3.1.1), we expect luminosity to approximately scale as $\rm L_{bol} \approx M_{ej}^2$ if these ratios are held constant.

Figure 3.8 shows synthetic spectra of these scaled models with total ejecta masses 1.0, 1.4, and 2.0 $M_{\odot}$. We find that the spectral features are remarkably unchanged despite a substantial variation in the masses. The only major difference is the bolometric luminosity.

This indicates that, in a generic sense, the nebular spectra of SNe Ia are consistent with non-$M_{\rm Ch}$ models, provided $E_{\rm k}$ and $M_{\rm 56Ni}$ scale accordingly.

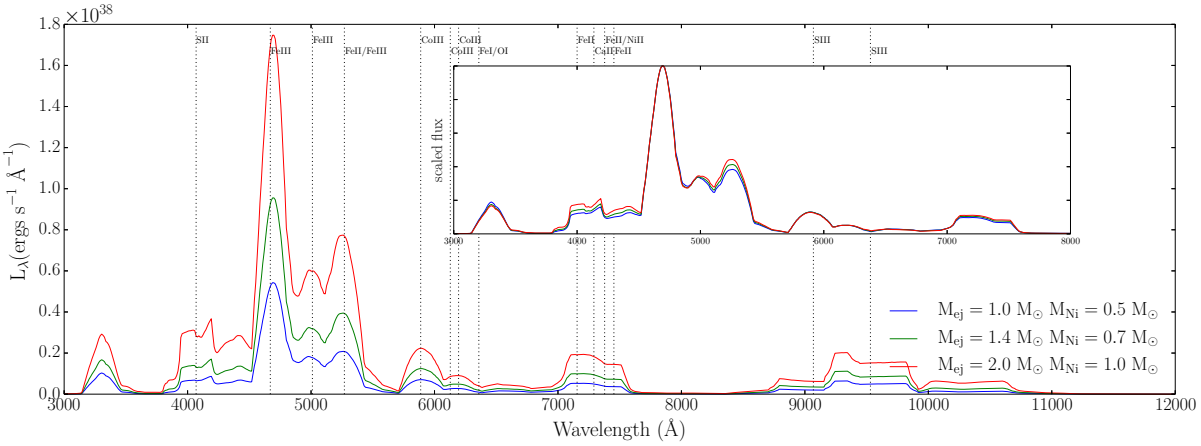

Figure 3.8: Same as Figure 3.5 but for the scaled parameter study which varies $M_{\rm ej}$ while keeping a fixed ratio of $M_{\rm 56Ni}/M_{\rm ej} = 1/2$ and $E_{51}/M_{\rm ej} = 1.2/1.4$. Unlike the models in which ejecta mass, kinetic energy, and ^{56}Ni mass are varied individually, these models produce almost identical synthetic spectra in all respects except for the overall bolometric luminosity.

3.2.4 Radioactive Nickel Mass

A number of observational studies and theoretical models indicate that the ^{56}Ni masses of normal SNe Ia range from 0.3 to 1.2 $M_\odot$ (Bravo et al., 2009; Gamezo, Khokhlov, and Oran, 2005; Jordan et al., 2012, 2008; Mazzali et al., 2007a; Plewa, 2007; Raskin et al., 2009; Röpke and Niemeyer, 2007; Röpke et al., 2007; Rosswog et al., 2009; Seitenzahl, Ciaraldi-Schoolmann, and Röpke, 2011; Seitenzahl et al., 2013), with a typical value near 0.6 $M_\odot$ (Branch and Khokhlov, 1995).

Figure 3.9 shows synthetic spectra of the fiducial model with $M_{\rm 56Ni}$ varied in the range $0.4 - 0.8$ $M_\odot$. Naturally, the bolometric luminosity increases proportionally with $M_{\rm 56Ni}$. The line ratios in these spectra are relatively insensitive to $M_{\rm 56Ni}$, with the exception being greater blending around the [Fe III] 5011 Å feature in higher ^{56}Ni mass models owing to the larger size of the ^{56}Ni core. The decrease in IME emission in higher $M_{\rm 56Ni}$ models is due to the lower total mass of IMEs in these models by construction (since $M_{\rm 56Ni} + M_{\rm IME}$ is held fixed).

3.2.5 Neutron-rich Iron-Group Elements (IGEs)

Stable IGEs are produced in SN Ia ejecta in two distinct ways. The trace presence of neutron-rich isotopes (in particular ^{22}Ne) due to the metallicity of the progenitor WD and pre-

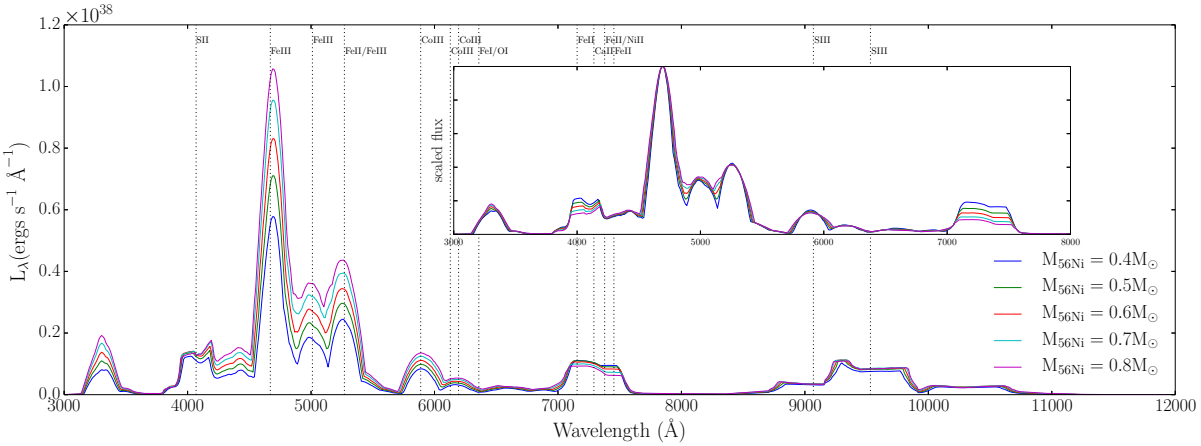

Figure 3.9: Same as Figure 3.5 but for the $M_{56\mathrm{Ni}}$ parameter study. Higher nickel mass models have larger nickel cores, and so produce slightly wider and more blended iron-group features. The declining IME mass (a result of keeping M_{ej} fixed while increasing $M_{56\mathrm{Ni}}$) results in declining IME emission.

explosion carbon simmering leads to the production of up to $\sim 25\%$ by mass of neutronized IGEs (in particular ^{54}Fe and ^{58}Ni) throughout the nickel core (Martínez-Rodríguez et al., 2016; Piro and Bildsten, 2008; Timmes, Brown, and Truran, 2003). In addition, electron capture occurring in nuclear burning at high central densities can lead to the production of $\sim 0.05 - 0.4\ M_\odot$ of neutronized IGEs (Nomoto, Thielemann, and Yokoi, 1984; Seitenzahl, Ciaraldi-Schoolmann, and Röpke, 2011; Seitenzahl et al., 2013; Thielemann, Nomoto, and Yokoi, 1986). This latter effect only occurs in white dwarfs with $\mathrm{M_{ej}} \gtrsim \mathrm{M_{ch}}$ (owing to their higher central densities) and is also influenced by the timing of a possible deflagration-to-detonation transition (Seitenzahl et al., 2013). 1D M_{Ch} models often predict stable IGEs to be produced at the core (Mazzali et al., 2007a; Nomoto, Thielemann, and Yokoi, 1984), while multi-D simulations indicate that buoyancy should mix IGEs throughout the ^{56}Ni region (Gamezo, Khokhlov, and Oran, 2005; Kasen, Röpke, and Woosley, 2009; Seitenzahl, Ciaraldi-Schoolmann, and Röpke, 2011). As a result, nebular spectra indicators of stable IGEs would be valuable for inferring the progenitor scenario.

Figure 3.10 shows synthetic spectra of the fiducial model varying M_{stb}, the mass of a neutron-rich core, in the range $0.05 - 0.20\ M_\odot$. The stable IGEs are assumed to be an equal mix of ^{54}Fe and ^{58}Ni. As expected, the [Ni II] 7378 Å feature becomes apparent with a stable core mass of 0.05 $M_\odot$, which corresponds to 0.025 $M_\odot$ of ^{58}Ni. [Fe II] 7388 Å emission can also produce a peak near these wavelengths, in some cases dominating the feature, suggesting that [Ni II] may not even be needed to fit this peak (see §3.2.7).

Higher stable core mass also increases the relative fraction of Fe II compared to Fe III, which is a result of lowered non-thermal ionization in the non-radioactive core region. Another noteworthy product of a stable core is the flat-topped profile of the [Co III] 5888 Å

feature, produced by the absence of cobalt in the core region. The lower flux in IME features is due to the lower mass of IMEs in higher $M_{\rm stb}$ models by construction.

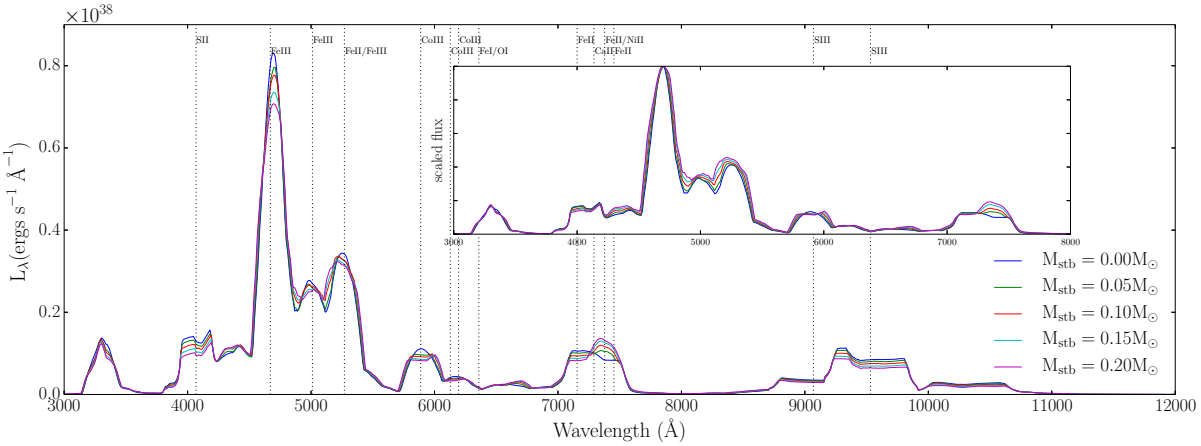

Figure 3.10: Same as Figure 3.5 but for the $M_{\rm stb}$ parameter study in which we add a region of stable IGEs of mass $M_{\rm stb}$ (and equal parts ^{58}Ni and ^{54}Fe) to the central core. We find that as little as 0.025 $M_\odot$ of central ^{58}Ni is enough to produce detectable emission at 7378 Å. The "hole" in energy deposition at the core also creates a characteristic flat-top profile for the [Co III] 5888 Å feature.

A comparison between two $M_{\rm stb}$ models and the fiducial model with a W7-like exponential density profile is shown in Figure 3.11. In the $M_{\rm stb} = 0.2M_\odot$ model we find an apparent blueshift of the [Ni II] 7378 Å peak by $\sim$ 1500 km/s because of the relative blending of this line with [Fe II] 7155 Å. The feature is also sensitive to [CaII] emission, which is stronger in the low-$M_{\rm stb}$ model. The [Fe II] 7453 Å feature redward of [Ni II] 7378 Å may also dominate in some models, resulting in an apparent redshift of the composite peak (see also §3.2.7). In the exponential model, both peaks are redshifted owing to line blending, which may lead to misinterpretation as ejecta asymmetry.

Maeda et al., 2010a find shifts in the 7378 Å peak of up to 3000 km/s, which they interpret as indications of ejecta asymmetry. Our models suggest that this geometrical interpretation is complicated by line blending. Isolating the [Ni II] emission in this feature can been attempted (Maeda et al., 2010b) but is subject to model-dependent uncertainties.

Surprisingly, the mixing of stable nickel through the nickel zone (i.e., varying the parameter $X_{\rm stb}$ in the range $0.05-0.20$) does not produce a visible effect on the synthetic spectrum, even for ^{58}Ni masses comparable to those in the core stable IGE region of Figure 3.10. This confirms the findings of Maeda et al., (2010b); it is due to the high level of ionization of Ni in the nickel zone, which suppresses [Ni II] emission. For the same reason, the ratio of ^{54}Fe to ^{58}Ni ($R_{\rm stb}$) in the nickel zone also had no visible effect on the synthetic spectra in the

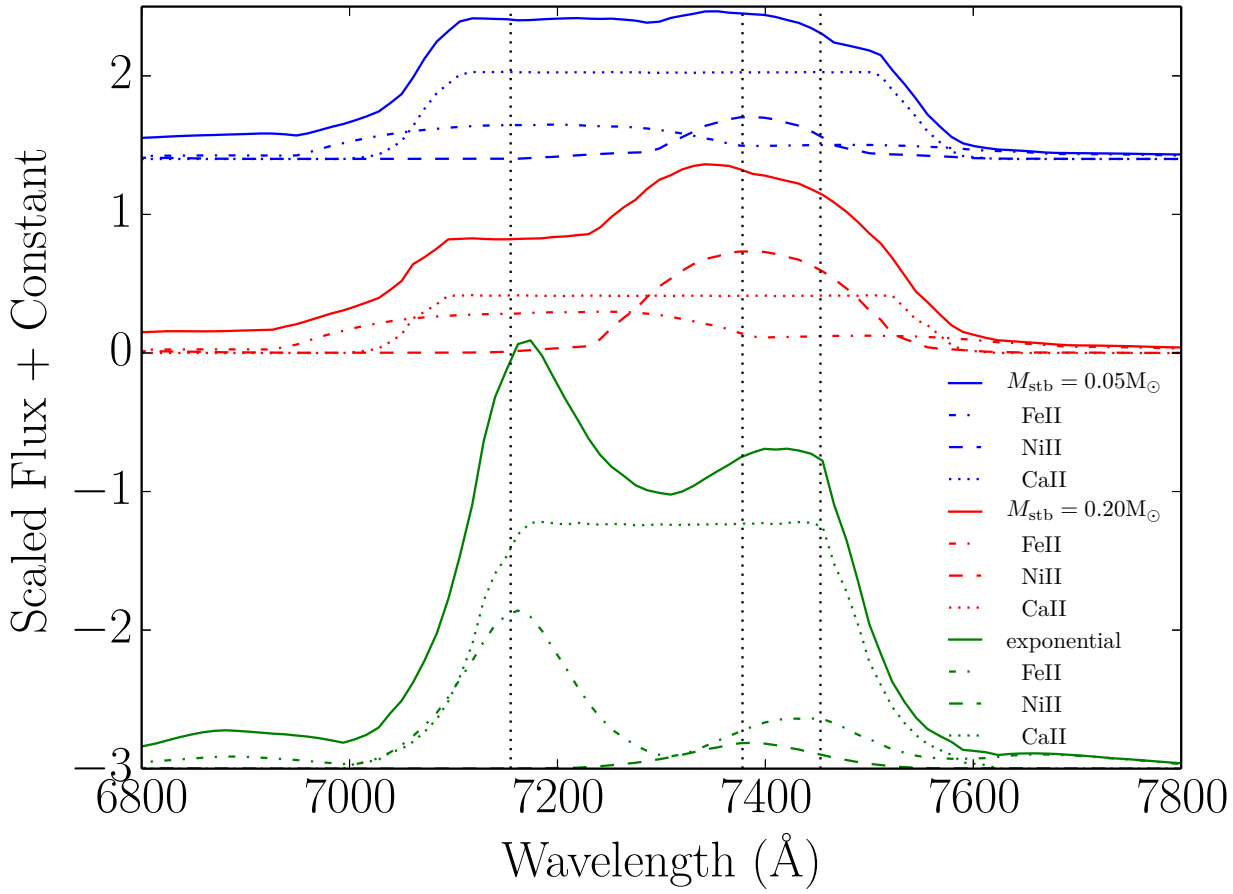

Figure 3.11: Decomposition of the spectral feature near [Ni II] 7388 Å for two models with varying stable core masses and for the fiducial model with a W7-like exponential profile. Vertical dotted lines show the line centers of the following transitions: [Fe II] 7155 Å, [Ni II] 7378 Å/[Fe II] 7388 Å, and [Fe II] 7453 Å. The apparent blueshift (by $\sim$ 1500 km/s) of the [Ni II] peak in the $M_{\rm stb} = 0.2\ M_\odot$ model is due to the relative blending between Fe II and Ni II components. The feature is also sensitive to [Ca II] emission, which is stronger in the low-$M_{\rm stb}$ model. The exponential density profile produces narrower lines, and line blending results in an apparent redshift for both peaks.

range (0.5-1.5) that we tested. We predict that up to 0.1 $M_\odot$ of stable nickel can be hidden in the ejecta of a SN Ia model with fiducial parameters because of this ionization effect.

3.2.6 Mass of Carbon/Oxygen in Ejecta

Observational studies have estimated that about 30% of SNe Ia show carbon in their early-time spectra (Maoz, Mannucci, and Nelemans, 2014, and references therein). The nearby

SN 2011fe also showed both carbon and oxygen in very early observations (Mazzali et al., 2014; Nugent et al., 2011), and hydrodynamical simulations have predicted various amounts of unburned C/O material mixed throughout the ejecta (Moll et al., 2014; Pakmor et al., 2012; Röpke, 2005; Seitenzahl et al., 2013). 3D nebular modeling by Kozma et al., (2005) showed clear [O I] features for a pure deflagration model of Röpke, (2005), which contained 0.6 $M_{\odot}$ of unburned C/O material. There have also been detections of possible [O I] emission in subluminous SNe Ia (Kromer et al., 2013; Taubenberger et al., 2013).

Figure 3.12 shows synthetic spectra of the fiducial model with C/O mass varied between $0.1 - 0.4$ $M_{\odot}$. We keep a fixed carbon-oxygen ratio of 1:9 and mix C/O into both the nickel zone and IME layer with the same mass fraction, consistent with the expected nucleosynthetic yields of delayed detonation explosions Seitenzahl et al., (2013).

We find a strong contribution of [O III] at 5007 Å as well a weak contribution of [O I] 6300/6364 Å and a blend of [O II] features at 7320 Å. The high ionization state of oxygen prevents the [O I] emission seen in Kozma et al., (2005) to contribute significantly, but we expect [O I] to become stronger if oxygen were more concentrated in the higher density central regions, or if the mass of ^{56}Ni (and hence radioactive deposition) were lower. In addition, our 1D models assume microscopic mixing of the C/O with IGEs; multidimensional models may find that clumps of oxygen isolated from ^{56}Co have lower ionization. C/O within the IME layer does not produce a significant nebular feature.

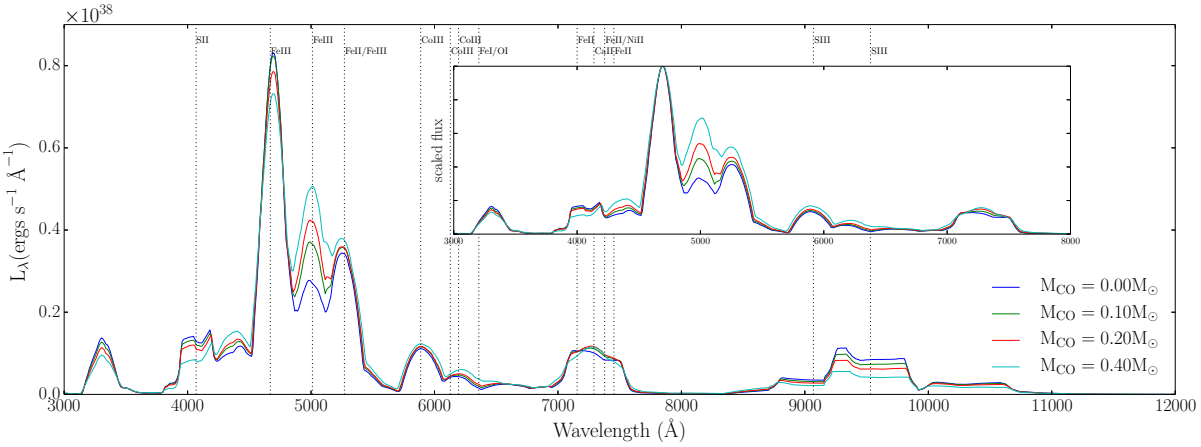

Figure 3.12: Same as Figure 3.5 but for the $M_{\rm CO}$ parameter study in which we mix C/O into both the nickel zone and IME layer (with a 1:9 carbon to oxygen ratio). Note the emergence of the [O III] 5007 Å feature with increasing C/O mass.

3.2.7 Sensitivity to Density Profile

The choice of the ejecta density profile is a critical input into nebular modeling. A broken power-law with a relatively flat interior was found to approximate the density structure in

some 2D delayed detonation models (Kasen, 2010), while a steeper exponential profile more closely fits the structure of the commonly used 1D W7 model (Nomoto, Thielemann, and Yokoi, 1984; Thielemann, Nomoto, and Yokoi, 1986). For the case of SN 2003hv, Mazzali et al., (2011) found that a core of lowered density provided a better fit to observed nebular spectra than a W7-like density profile. Here, we attempt to illuminate the effect of steepening our interior power-law density profiles. We also consider an exponential profile of the form $\rho = \rho_0 e^{-v/v_e}$, where ρ_0 and v_e can be determined from M_{ej}, E_K, and t_{ex}.

Figure 3.13 shows synthetic spectra of the fiducial model with varied density profiles. Steeper profiles, which concentrate more mass at low velocities, produce stronger and narrower spectral profiles. In particular, an exponential profile helps resolve the individual peaks in the feature around 7300 Å. Figure 3.11 shows the nebular emission of the exponential model around 7300 Å decomposed into contributions from individual ions. The bluer peak is dominated by [Fe II] 7155 Å, while the redder peak is dominated by [Fe II] 7388 and [Fe II] 7453 Å with some contribution from [Ni II] 7378 Å. [Ca II] 7291 Å adds an offset to the feature. These are consistent with the findings of Ashall et al., (2016) from their W7-like models for SN 1986G. Therefore, [Fe II] can account for the emission in the redder peak if stable Ni is absent, and it could potentially redshift that peak if stable Ni is present. In either case, we find that isolation of [Ni II] 7378 Å emission would be difficult.

Higher gamma-ray trapping due to higher central densities produces higher bolometric luminosities in steeper density profiles. Furthermore, steeper density profiles lead to lower central temperatures, as cooling becomes more efficient at higher densities. Therefore, the ionization state is lower, which changes the main [Fe III]/[Fe II] line ratio.

When comparing to the nebular spectrum of SN 2011fe, we find that a broken power-law with a flat interior profile ($\delta = 0$) best reproduces the shape of the features and the main iron line ratios, whereas an exponential density produces lines that are too centrally peaked and overestimates the [Fe II] to [Fe III] ratio (indicated by high flux in the [Fe II] feature at 5159 Å). While there is some degeneracy with other parameters, such as kinetic energy, nebular models may be able constrain the interior ejecta density, which should be useful in testing explosion models.

3.2.8 Sensitivity to Atomic Data Uncertainties

One important factor for the modeling of nebular spectra is the extensive atomic data inputs. Uncertainties in published atomic data, discrepancies between different sources for the same data, and the need for crude approximations where data are lacking impact the model predictions. Here we attempt to quantify some of the uncertainties by systematically changing the values of three of the most important and uncertain atomic data – the collisional ionization cross sections (Q_k), the thermal collisional excitation rates (C_{ij}), and the radiative recombination rates (α).

We show the impact of systematically varying atomic data in Figures 3.14–3.15. To explore the effect of the collisional ionization cross sections (Figure 3.14), we carried out calculations in which (a) all ionization cross sections were increased by a factor of 2, (b) all

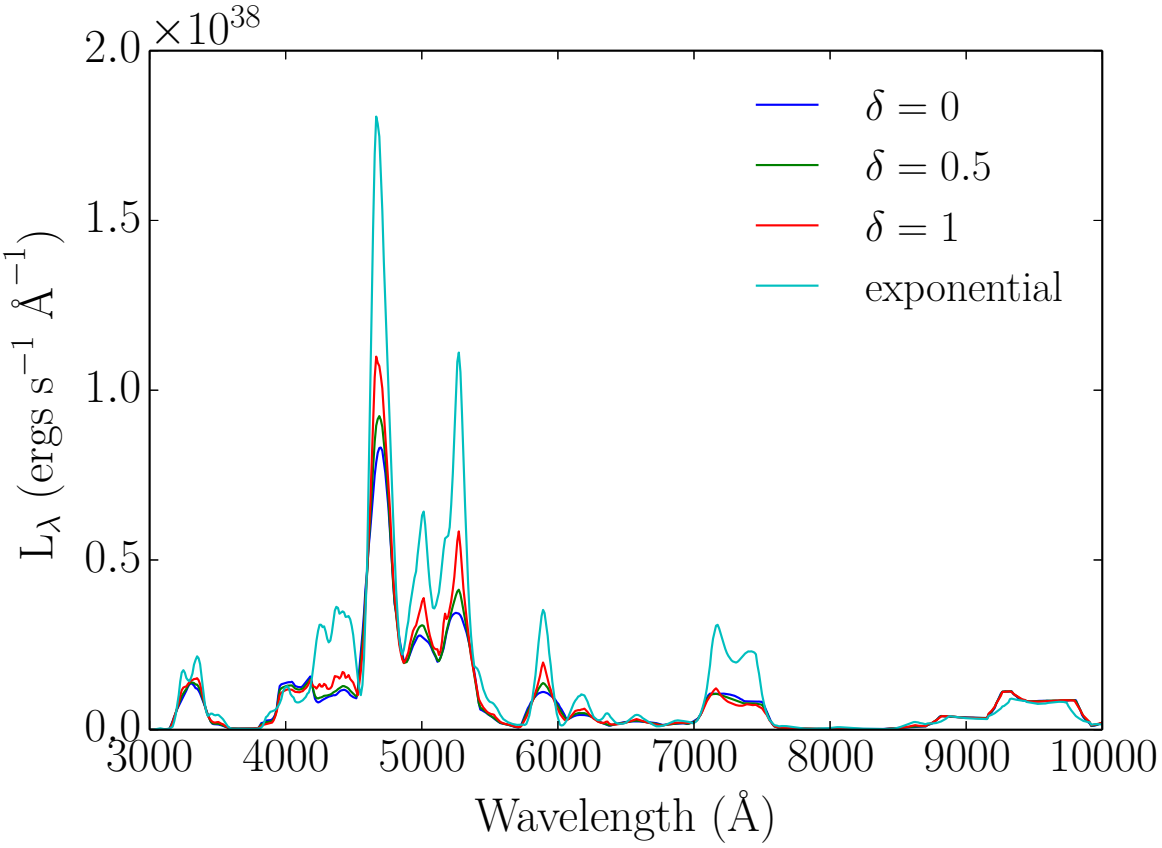

Figure 3.13: Fiducial model with varying density profiles. δ refers to the exponent of the inner region in which $\rho \propto v^{-\delta}$, and the exponential model has a density $\rho \propto e^{-v/v_e}$ with a characteristic e-folding velocity $v_e(M_{ej}, E_K)$. Steeper density profiles concentrate more mass toward the center and have narrower features, higher bolometric luminosities, and lower ionization states (as indicated by the ratio of fluxes at 4665 Å and 5272 Å).

ionization cross sections were decreased by a factor of 2, (c) the cross section of Fe II was decreased by a factor of 2 and that of Fe III was increased by a factor of 2, and (d) the cross section of Fe II was increased by a factor of 2 and that of Fe III was decreased by a factor of 2. These variations in Q affect the ionization ratio of [Fe III]/[Fe II] and can modify the [Fe III]/[Fe II] line ratio by up to $\pm$25%. There are also indirect effects, since changes to the atomic data of one element can alter the calculated gas temperature and so result in changes in the emission from other species.

To explore the effect of the thermal collisional excitation rates (Figure 3.15), we carried out calculations in which all σ_{ij} were increased or decreased by a factor of 2. These variations in σ_{ij} affect the strength of emission features and can modify the [Fe III]/[Fe II] line ratio by

up to ±10%.

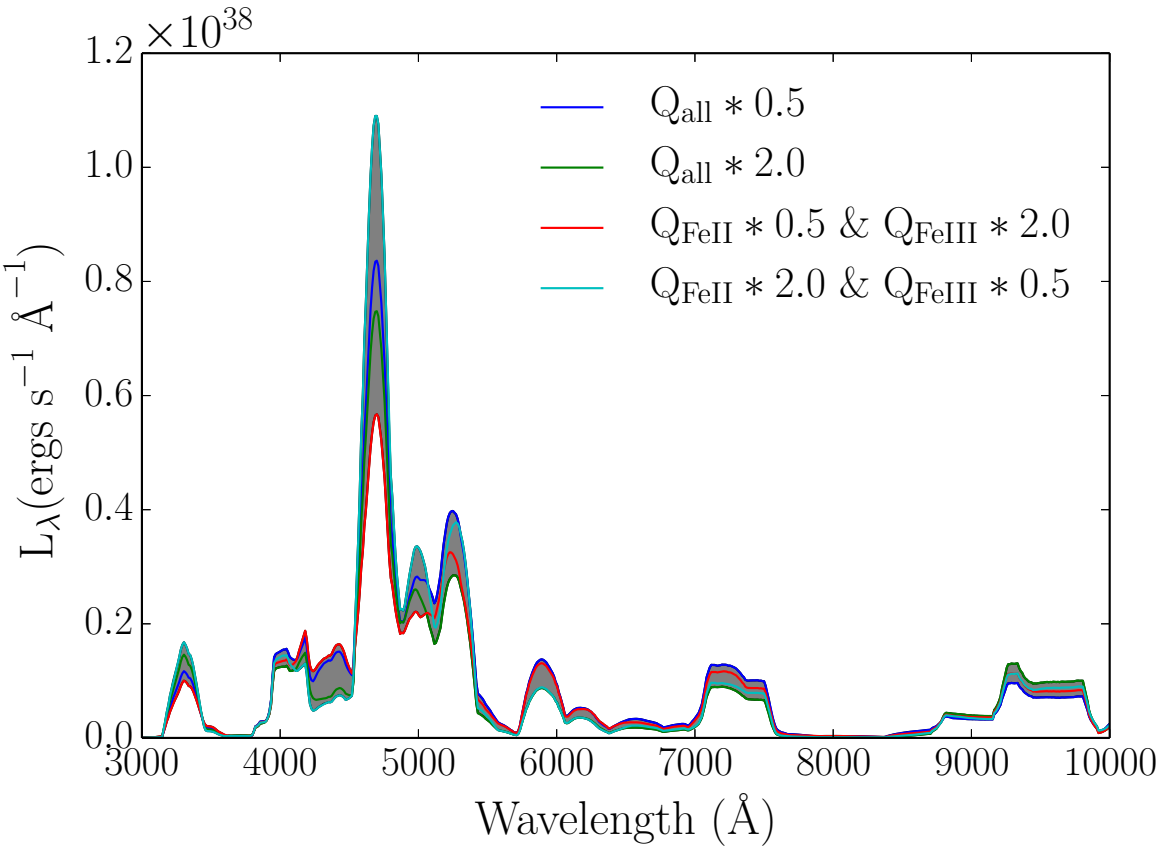

Figure 3.14: Fiducial model in which collisional ionization cross-section values were scaled by the same factor. Uncertainties at the factor of 2 level in the cross-sections produce $\sim 25\%$ changes in the spectral features.

We show in Figure 3.16 the fiducial model calculated using recombination rates from two different databases. Our calculations throughout have used recombination rates from the CHIANTI database, but more recent data for Fe I-V are available from the Nahar OSU Radiative Atomic Database (NORAD) (Nahar, 1997, 1996; Nahar, Bautista, and Pradhan, 1998, 1997). With this latter data-set, we have access to state-specific recombination rates, which we neglected in the above treatment. We also neglected charge transfer in the above analyses, which becomes important for a nickel zone with low ionization state (as is the case with NORAD recombination rates). We therefore include charge transfer in Fe I-IV with data from Krstic, Stancil, and Schultz, (1997).

While there is reasonable agreement between the synthetic spectra, the strength of emission features does depend on the atomic data set. In particular, the [Fe III]/[Fe II] line ratio

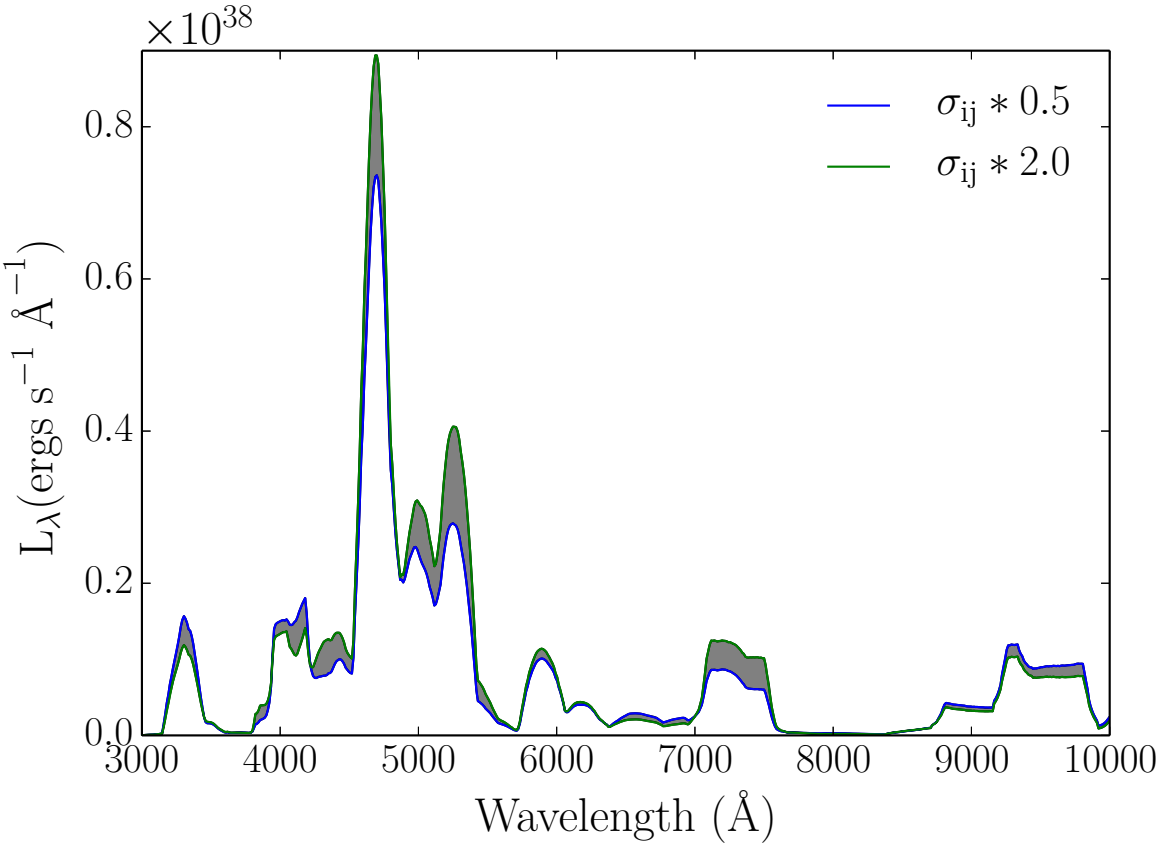

Figure 3.15: Fiducial model in which collisional excitation rates for all transitions of all species where scaled by the same factor.

shows a higher Fe II population when NORAD recombination rates are used, due to higher total recombination rates for Fe I-III in the NORAD data set, leading to a $\sim$ 30% decrease in the [Fe III]/[Fe II] line ratio. Similar variations are seen in most other spectral features.

3.3 Discussion

We have presented a new tool for calculating nebular spectra of SNe and applied it to a systematic parameter study of SNe Ia. We summarize some of our main results as follows.

Robustness and Degeneracy of Spectral Features: On the whole, we found that the features in SN Ia nebular spectra were remarkably insensitive when physical parameters were changed within the range expected for white dwarf explosions. Individually changing the ejected mass, ^{56}Ni mass, or kinetic energy by 50% produced only minor changes in

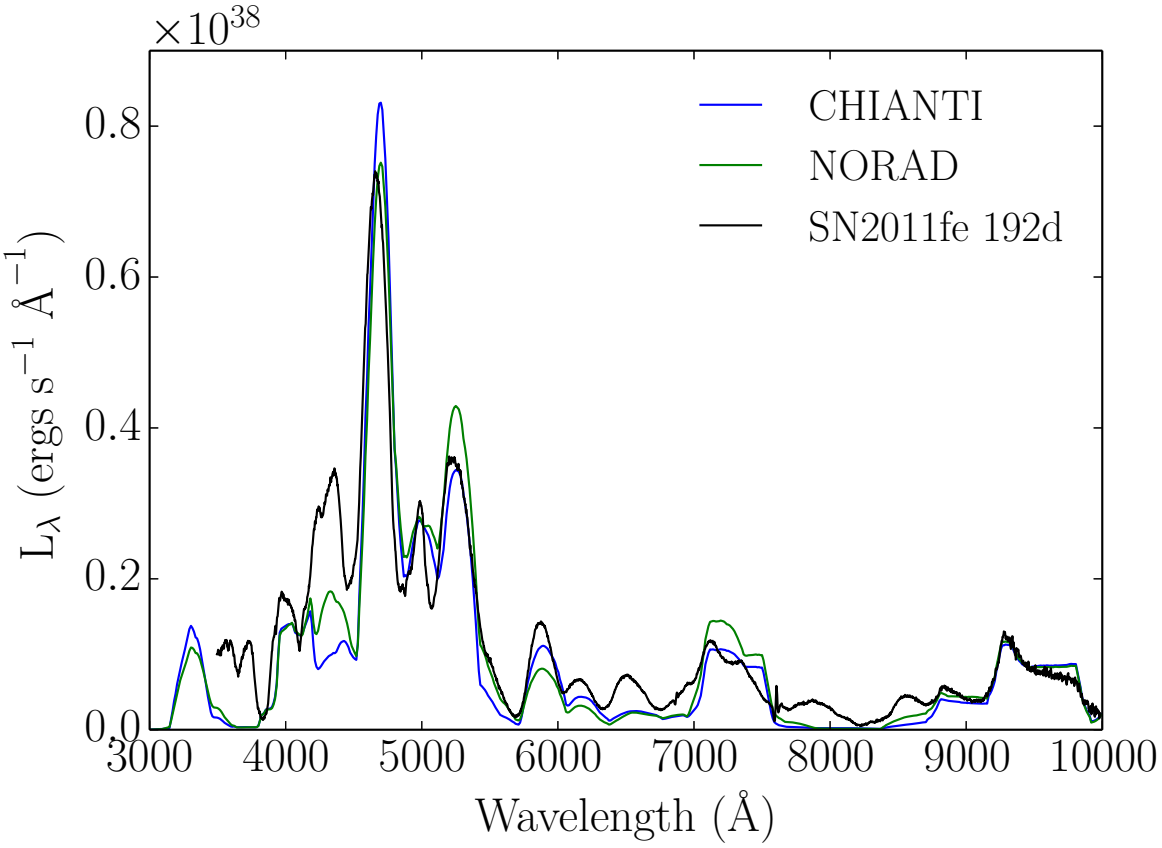

Figure 3.16: Fiducial model with two different sets of recombination rates for Fe I-V.

the relative strength of features (although the bolometric luminosity was affected owing to changes in gamma-ray trapping). Varying parameters by a larger factor of ~ 2 began to show noticeable spectral changes.

In addition, we found degeneracies in the effect of different physical parameters. An increase in the total ejecta mass, for example, could be mostly offset by a corresponding increase in kinetic energy so as to keep the overall density and velocity scale roughly fixed. As a result, quite different sets of physical parameters may be able to fit the same nebular spectrum.

Progenitor Mass: Though some previous studies have favored Chandrasekhar-mass models in explaining SN Ia nebular spectra, our model survey demonstrates that observed nebular spectra are equally well fit by generic sub-Chandrasekhar mass, Chandrasekhar mass, and super-Chandrasekhar mass models. The spectral features remained essentially unchanged when the total mass, ^{56}Ni mass, and kinetic energy were scaled up or down in unison (Figure 3.8). Nebular spectra therefore do not alone constrain the overall mass scale of SNe Ia,

and instead are more diagnostic of the relative abundance yields and the density profile.

Stable Iron Group Elements: Previous studies have fit the nebular spectra of SNe Ia with models having a $\sim 0.1-0.2\ M_\odot$ sphere of stable IGEs at the ejecta center. The presence of such an IGE "core" would favor a Chandrasekhar-mass model (where electron capture occurs during high-density deflagration burning), while disfavoring double-detonation and violent merger models.

A stable IGE "core" has been claimed necessary to explain the [Fe III]/[Fe II] line ratio in observed spectra (Maeda et al., 2010b; Mazzali et al., 2015). We show that this line ratio also depends on other explosion parameters, such as the density profile and kinetic energy, and is sensitive to the atomic data inputs. We present models that fit the SN 2011fe iron line ratio well without invoking any stable IGE "core."

Our models that did include a large ($\gtrsim 0.1\ M_\odot$) stable IGE "core" produced a flat-topped [Co III] feature near 5900 Å. Such a flat-top [Co III] profile is not seen in the nebular spectra of SN 2011fe (Mazzali et al., 2015), indicating that at least some radioactive cobalt exists at the lowest ejecta velocities. Höflich et al., (2004) and Motohara et al., (2006) observe relatively flat-topped profiles of the 1.64 μm [Fe II] feature in SN 2003du and SN 2003hv, respectively, which they take as evidence that SNe Ia have a stable IGE "core" lacking any radioactive heating. The lack of an obvious flat-topped optical [Co III] feature in SN 2011fe appears to provide evidence to the contrary.

Another diagnostic of stable IGE is the feature at ~ 7300 Å usually attributed to [Ni II]. Similar to (Mazzali et al., 2015), we find that a small amount ($\sim 0.01\ M_\odot$) of central ^{58}Ni is sufficient to reproduce a peak at 7300 Å. However, we note that in some models the [Fe II] 7388 Å and 7453 Å lines can alone account for this peak, while in general [Fe II] 7155 Å and [Ca II] 7291 Å emission also shape the overall line profile. The steepness of the inner ejecta density profile also affects how narrow and resolved the separate line peaks of the 7300 Å feature are. We find that additional ^{58}Ni mixed throughout the lower-density layers of radioactive ^{56}Ni zone may be too ionized to produce significant [Ni II] 7378 Å emission. As a result, we consider it difficult to derive a precise ^{58}Ni mass constraint from analysis of the 7300 Å feature.

In sum, our parameter study does not provide strong evidence that SNe Ia possess a substantial stable IGE "core," nor do we see a robust way of accurately inferring the total stable IGE mass from nebular spectrum analysis. We therefore do not consider the nebular spectra of SNe Ia as providing particularly strong support for the Chandrasekhar-mass model over other progenitor scenarios. However, our study did not focus on infrared features (Gerardy et al., 2007; Höflich et al., 2004; Motohara et al., 2006; Telesco et al., 2015) or the effects of positron transport (Penney and Hoeflich, 2014). Further study of stable IGE signatures using specific multidimensional explosion models is warranted.

IME indicators: While the nebular spectra of SNe Ia are dominated by iron lines, we emphasize that some features provide constraints on IME abundances. In particular, the feature at 7300 Å is sensitive to [Ca II] emission at 7291 Å, while the feature at 9500 Å is dominated by [S III] emission. We showed that the relative strength of the [S III] 9500 Å

feature to the [Fe III] 4664 Å feature tracked the relative abundance of IGEs to IMEs (see Figure 3.9). Analysis of this line ratio may thus provide valuable constraints on the nucleosynthetic yields and hence progenitors of SNe Ia. Our successful fit to the calcium and sulfur features in SN 2011fe suggests that the total IME yields may be as high as $\sim 0.75\ M_{\odot}$. However, we note that material at high velocities does not contribute significantly to nebular emission, so it is not possible to constrain all of the IME mass using nebular modeling.

Line Shifts and Ejecta Geometry: Shifts in the wavelengths of nebular line peaks are seen in many SNe Ia (Black, Fesen, and Parrent, 2016) and have been used to deduce asymmetries of IGEs (Maeda et al., 2010b). Though we have only considered spherically symmetric models in this paper, we nevertheless see shifts in the location of emission peaks due to line blending. For example, the feature around 7300 Å is a blend of [Ni II], [Fe II], and [Ca II] lines. Depending on the ejecta compositional structure and temporal evolution of line strengths, the location of the composite peak can vary by 1500 km/s in different models. This highlights the difficulty in using the 7300 Å feature shift to derive reliable kinematic measures of asymmetry (though see Maeda et al., 2010b for attempts to separate components in the blend). Our models do not show a strong, progressive redshift evolution in the main IGE features as a function of time. This supports the claim of Black, Fesen, and Parrent, (2016) that these shifts are due to permitted line emission that may help shape the spectrum even at times $\gtrsim 200$ days after explosion.

Carbon/Oxygen mixing: We find that C/O material mixed into a nickel zone is highly ionized. For large enough C/O masses ($\gtrsim 0.1\ M_{\odot}$) this produces a visible [O III] feature at 5007 Å, which is not seen in SN 2011fe. This disfavors models leaving significant amounts of oxygen mixed throughout the ejecta. To produce a narrow [O I] feature like that seen by Taubenberger et al., (2013) in the subluminous SN 2010lp would presumably require the C/O to be located in a dense central region with less non-thermal ionization from radioactivity. C/O in the outermost ejecta layers (within or above the IME zone) does not experience significant radioactive heating and has no impact on the nebular spectra.

Density Profile: We have shown that ejecta having a steep interior density profile produce narrower and more central peaked nebular emission features. In fact, the line widths depended more on the density profile than on the kinetic energy, since the former sets the degree of central concentration of mass. Comparing to the spectra of SN 2011fe, we find that a flat density profile (power-law index $\delta = 0 - 1$) best reproduces the observed spectral profiles. This suggests that nebular spectra may be able to test the density structures predicted by detailed SN Ia explosion models.

Atomic Data: Though it is well known that synthetic nebular spectra are affected by uncertainty and incompleteness in the input atomic data, the level of error has not been well quantified. We showed here that factor of 2 errors in some of the key atomic data inputs can result in changes in spectral features at the $\sim 25\%$ level. This level of variation is similar to the level we found when varying the physical ejecta parameters. Given the uncertainties, we advise against overinterpreting model fits to extract quantitative mass estimates from

individual observed SNe Ia. The trends seen among a sample of nebular spectra, however, are likely less affected by the atomic data limitations.

Limitations: While the spectral models presented here included a broad range of the most important and complex atomic processes, other physical effects may be relevant and should be addressed in future work. While the ejecta are mostly optically thin at optical wavelengths, there is evidence that some lines are nevertheless optically thick, especially in the ultraviolet (Friesen et al., 2017). Furthermore, dust/molecule absorption and emission may be important at some phases. At very late times, the freezing out of ionization requires that the problem be treated time-dependently (Jerkstrand et al., 2015; Kozma and Fransson, 1998a). The collection of reliable and complete atomic data-sets has been and remains a substantial challenge for all nebular phase modeling efforts.

Finally, while this paper was restricted to 1D parameterized models, the asphericity found in more realistic explosion models, and inferred from polarization observation of SNe, is expected to affect the nebular spectra. Our NLTE nebular spectrum code is 3D, and future work on SNe Ia and other types of SNe will aim to explore the predictions of 3D hydrodynamical models that have complex abundance distributions, clumping on multiple scales, and global ejecta asymmetries.

Ion	λ_{ij} (**Å**)	A_{ij} ($\mathbf{s^{-1}}$)	**Conf.** ($^{2S+1}L^{\pi}_{J}$)	E_i (eV)	E_j (eV)
S II	4069	0.2250	$S^{o}_{3/2} -^{2} P^{o}_{3/2}$	0.00	3.05
Fe III	4658	0.4500	$^{5}D^{e}_{4} -^{3}_{2} F2^{e}_{4}$	0.00	2.66
O III	5007	0.0196	$^{3}P^{e}_{2} -^{1} D^{e}_{2}$	0.04	2.51
Fe III	5011	0.5400	$^{5}D^{e}_{2} -^{3} P2^{e}_{1}$	0.09	2.57
Fe II	5159	0.5805	$a^{4}F^{e}_{9/2} - a^{4}H^{e}_{13/2}$	0.23	2.63
Fe III	5270	0.4200	$^{5}D^{e}_{3} -^{3} P2^{e}_{2}$	0.05	2.41
Co III	5888	0.4001	$a^{4}F^{e}_{9/2} - a^{2}G^{e}_{9/2}$	0.00	2.10
Co III	6128	0.1100	$a^{4}F^{e}_{5/2} - a^{2}G^{e}_{7/2}$	0.18	2.20
Co III	6195	0.1200	$a^{4}F^{e}_{7/2} - a^{2}G^{e}_{9/2}$	0.10	2.10
Fe II	7155	0.1495	$a^{4}F^{e}_{9/2} - a^{2}G^{e}_{9/2}$	0.23	1.96
Ca II	7291	0.803	$^{2}S^{e}_{1/2} -^{2} D^{e}_{5/2}$	0.00	1.70
Ni II	7378	0.1955	$^{2}D^{e}_{5/2} -^{2} F^{e}_{7/2}$	0.00	1.16
Fe II	7388	0.0435	$^{4}F^{e}_{5/2} - a^{2}G^{e}_{7/2}$	0.35	2.03
Fe II	7453	0.0485	$a^{4}F^{e}_{7/2} - a^{2}G^{e}_{9/2}$	0.30	1.96
Fe II	7638	0.0070	$a^{6}D^{e}_{7/2} - a^{4}P^{e}_{5/2}$	0.05	1.67
Fe II	8617	0.0334	$a^{4}F^{e}_{9/2} - a^{4}P^{e}_{5/2}$	0.23	1.67
Fe III	8729	0.0495	$^{3}P2^{e}_{2} -^{3} D^{e}_{3}$	2.41	3.83
S III	9069	0.0221	$^{3}P^{e}_{1} -^{1} D^{e}_{2}$	0.04	1.40
S III	9531	0.0576	$^{3}P^{e}_{2} -^{1} D^{e}_{2}$	0.10	1.40
S II	10336	0.1630	$^{2}D^{o}_{3/2} -^{2} P^{o}_{1/2}$	1.84	3.04
S II	10370	0.0779	$^{2}D^{o}_{5/2} -^{2} P^{o}_{1/2}$	1.85	3.04

Table 3.2: Line Identifications for Optical SN Ia Nebular Spectra

Model	v_t (km/s)	ρ_c (10^{-17} g/cm^3)	M_{IME} ($M_\odot$)	$M_{stb,tot}$ Fe, Ni ($M_\odot$)	L_{bol} (10^{40} erg/s)	$\mathbf{L_{4665}/L_{5272}}$
fiducial	10,131	8.65	0.75	0.016, 0.016	7.96	2.30
$t_{ex} = 250$ days	10,131	4.43	0.75	0.016, 0.016	3.93	2.45
$t_{ex} = 200$ days	10,131	2.56	0.75	0.016, 0.016	2.11	2.53
$t_{ex} = 350$ days	10,131	1.61	0.75	0.016, 0.016	1.19	2.54
$t_{ex} = 400$ days	10,131	1.08	0.75	0.016, 0.016	0.70	2.48
$M_{ej} = 1.0$ M$_\odot$	12,000	3.73	0.36	0.016, 0.016	5.27	2.75
$M_{ej} = 1.1$ M$_\odot$	11,442	4.73	0.46	0.016, 0.016	5.82	2.65
$M_{ej} = 1.2$ M$_\odot$	10,954	5.88	0.54	0.016, 0.016	6.58	2.53
$M_{ej} = 1.3$ M$_\odot$	10,525	7.19	0.65	0.016, 0.016	7.18	2.41
$M_{ej} = 2.0$ M$_\odot$	8,485	21.10	1.33	0.016, 0.016	13.91	1.86
$E_K = 1.0$B	9,258	11.37	0.75	0.016, 0.016	8.90	2.15
$E_K = 1.1$B	9,710	9.86	0.75	0.016, 0.016	8.33	2.23
$E_K = 1.3$B	10,556	7.67	0.75	0.016, 0.016	7.57	2.37
$E_K = 1.4$B	10,954	6.86	0.75	0.016, 0.016	7.22	2.44
$E_K = 1.5$B	11,339	6.19	0.75	0.016, 0.016	6.96	2.50
$E_K = 2.0$B	13,093	4.02	0.75	0.016, 0.016	5.79	2.73
$M_{56Ni} = 0.4$ M$_\odot$	10,131	8.65	0.96	0.011, 0.011	5.49	2.25
$M_{56Ni} = 0.5$ M$_\odot$	10,131	8.65	0.85	0.013, 0.013	6.77	2.28
$M_{56Ni} = 0.7$ M$_\odot$	10,131	8.65	0.64	0.019, 0.019	9.22	2.32
$M_{56Ni} = 0.8$ M$_\odot$	10,131	8.65	0.55	0.021, 0.021	10.21	2.33
$M_{stb} = 0.05$ M$_\odot$	10,131	8.65	0.71	0.040, 0.040	7.75	2.28
$M_{stb} = 0.10$ M$_\odot$	10,131	8.65	0.64	0.066, 0.066	7.81	2.25
$M_{stb} = 0.15$ M$_\odot$	10,131	8.65	0.59	0.093, 0.093	7.64	2.21
$M_{stb} = 0.20$ M$_\odot$	10,131	8.65	0.54	0.116, 0.116	7.55	2.17
$M_{ej} = 1.0$ scaled[1]	10,240	6.15	0.46	0.013,0.013	5.35	2.49
$M_{ej} = 1.4$ scaled	10,240	8.65	0.64	0.019,0.019	9.21	2.32
$M_{ej} = 2.0$ scaled	10,240	12.40	0.91	0.027,0.027	16.88	2.17
$M_{CO} = 0.05$ M$_\odot$	10,131	8.65	0.70	0.016, 0.016	7.85	2.25
$M_{CO} = 0.10$ M$_\odot$	10,131	8.65	0.64	0.017, 0.017	8.04	2.20
$M_{CO} = 0.15$ M$_\odot$	10,131	8.65	0.59	0.018, 0.018	7.90	2.15
$M_{CO} = 0.20$ M$_\odot$	10,131	8.65	0.55	0.019, 0.019	7.82	2.09
$M_{CO} = 0.40$ M$_\odot$	10,131	8.65	0.33	0.023, 0.023	7.76	1.86
$\delta = 0.5$, n = 10[2]	10,528	66.89	0.75	0.016, 0.016	8.21	2.17
$\delta = 1.0$, n = 10	11,098	486.5	0.75	0.016, 0.016	8.95	1.88
exponential[3]	N/A	106.6	0.75	0.016, 0.016	12.56	1.63
all $Q_k \times 2$[4]	10,131	8.65	0.75	0.016, 0.016	7.96	2.49
all $Q_k \times 0.5$	10,131	8.65	0.75	0.016, 0.016	7.96	2.02
$Q_{FeII} \times 2$, $Q_{FeIII} \times 0.5$	10,131	8.65	0.75	0.016, 0.016	7.96	2.74
$Q_{FeII} \times 0.5$, $Q_{FeIII} \times 2$	10,131	8.65	0.75	0.016, 0.016	7.96	1.72
all $\sigma_{ij} \times 2$[5]	10,131	8.65	0.75	0.016, 0.016	7.96	2.10
all $\sigma_{ij} \times 0.5$	10,131	8.65	0.75	0.016, 0.016	7.96	2.52
α from NORAD	10,131	8.65	0.75	0.016, 0.016	7.96	1.66

Table 3.3: List of models included in physical parameter study. The parameter varied from the fiducial value in each model is shown in the model description, and some derived values are shown. v_t is the transition velocity of the density profile determined by power-law exponents δ and n; ρ_c is the central density. The column for $M_{stb,tot}$, which is the sum of neutron-rich core material and stable isotopes mixed into the nickel zone, reports ^{54}Fe and ^{58}Ni masses separately. L_{bol} is the total luminosity over all wavelengths. L_{4665}/L_{5272} is the ratio of luminosities at 4665 Å and 5272 Å, the wavelengths at which the prominent [Fe III] and [Fe II]/[Fe III] features peak, respectively.

Chapter 4

Multidimensional Models of Type Ia Supernova Nebular Spectra Rule Out Classic Single-Degenerate Systems

4.1 Introduction

While it is believed that Type Ia supernovae (SNe Ia) are the thermonuclear explosion of a carbon-oxygen white dwarf (WD) in a binary system, the nature of the companion star and the mechanism that triggers the disruption remain uncertain. SNe Ia have been used successfully to infer the accelerating expansion of the universe (Perlmutter et al., 1999; Riess et al., 1998), and a better understanding of SN Ia progenitors may lead to an improved ability to standardize these events. Various theoretical models can reproduce the basic observational properties of SNe Ia (Hillebrandt et al., 2013; Wang and Han, 2012), but work is needed to determine which models explain various specific subsets of observed SNe Ia.

SN Ia models fall into either the single-degenerate (SD) or double-degenerate (DD) category, depending on the nature of the WD's binary companion. A key prediction of SD progenitor models is that material from the companion star will be swept up by SN Ia ejecta (Chugai, 1986; Wheeler, Lecar, and McKee, 1975) and may be detectable in late-time spectra. Hydrodynamical simulations have found that the mass of stripped companion material is typically between 0.002 and 0.5 $M_{\odot}$, depending on the type of companion and the binary system properties (Boehner, Plewa, and Langer, 2017; Liu et al., 2012; Liu et al., 2013; Marietta, Burrows, and Fryxell, 2000; Meng, Chen, and Han, 2007; Pakmor et al., 2008; Pan, Ricker, and Taam, 2010, 2012). This material is embedded in the ejecta at low velocities ($\sim$ 1000 – 2000 km s^{-1}) and may be observable as narrow emission lines at late times ($\gtrsim$ 200 days) when the ejecta become optically thin.

The WD explosion may also interact with circumstellar material (CSM), produced by periods of binary mass transfer, pre-supernonova outbursts, or a wind from the binary companion (Harris, Nugent, and Kasen, 2016). In these cases, broad Hα emission is visible

before the onset of the nebular phase and can stay prominent into its late stages, like in the case of PTF11kx (Dilday et al., 2012; Graham et al., 2017; Silverman et al., 2013). For the purposes of this work, we define a normal SN Ia one that has no known CSM interaction; in particular, any Hα emission detected at late times would be produced by material stripped from the companion and become visible only when the core becomes optically thin.

Many observations of SN have failed to detect Balmer emission (specifically, Hα) in late-time spectra (Bikmaev et al., 2015; Leonard, 2007; Lundqvist et al., 2013, 2015; Maguire et al., 2016; Mattila et al., 2005; Shappee et al., 2013). The only known exception may be the 3.1σ detection of Hα in SN 2013ct by Maguire et al., (2016). Translating the flux limits into a reliable constraint on the stripped mass, however, requires multidimensional hydrodynamical and radiative transfer calculations which have not, to date, been conducted.

Most analyses of late-time SN Ia spectra derive mass constraints from Mattila et al., (2005), who studied Hα formation at late times using parameterized spherically symmetric radiative transfer calculations. These models assumed the W7 SN ejecta profile (Nomoto, Thielemann, and Yokoi, 1984; Thielemann, Nomoto, and Yokoi, 1986) and added by hand varying amounts of uniform density solar abundance material at the center of the ejecta up to a fixed velocity of 1000 km s^{-1}. These authors concluded that stripped masses $\gtrsim 0.03\ M_\odot$ should produce detectable Balmer lines in the nebular spectra of SNe Ia, in conflict with observations.

Hydrodynamical models of the interaction of SNe Ia with a companion star, however, find that the stripped companion material strongly varies in density and its distribution is highly nonuniform. How this affects the predicted emission-line strengths is unclear, and requires multi-D modeling.

In this Chapter, we study realistic distributions of stripped companion material derived from multi-D hydrodynamical simulations which we post-process with a multi-D non-local thermodynamic equilibrium (NLTE) radiative transport code to synthesize nebular spectra as a function of viewing angle. This allows us to predict the line strengths resulting from stripped material of different total mass and composition, and from a variety of different companion stars (main-sequence stars, subgiants, and red giants).

4.2 Methods

The SN Ia ejecta-companion interaction models used in this work are taken from Boehner, Plewa, and Langer, 2017 (henceforth B17). Assuming cylindrical symmetry, they obtained well-resolved hydrodynamic models of interaction for a sample of semidetached binaries considered as potential SN Ia SD progenitor channels. The sample includes systems with various main sequence (MS), subgiant (SG), and red giant (RG) companions. The spherically symmetric W7 model (Nomoto, Thielemann, and Yokoi, 1984; Thielemann, Nomoto, and Yokoi, 1986) is used as the explosion model for the supernova.

We calculate nebular spectra using the 3D NLTE radiation transport code presented in Botyánszki and Kasen, (2017), which takes as input a homologously expanding supernova

model and calculates ejecta temperature and line emissivities based on the balance of radioactive heating and line emission. Energy deposition from radioactively produced gamma-rays is calculated using the Monte Carlo code from Kasen, Thomas, and Nugent, (2006) while positrons are assumed to be deposited locally. The ejecta are assumed to be optically thin, though we adjust the radiative decay rates of optically thick lines using the formulation of Li and McCray, (1993).

Recombinations are assumed to be transitions between ground states only, except in the case of hydrogen and helium, where recombination to excited states is expected to contribute nontrivially to optical line strengths. For these species, we use a simplified approach in which the recombination rates split evenly among levels and the sum of these is consistent with the well-known total recombination rates. While this recombination treatment can be improved by using level dependent values for the recombination rates, the ionization fractions of elements depend only on total recombination rates. Allowing recombination to excited states in hydrogen lowers optical line strengths, suggesting that collisional excitation from the ground state is the dominant way of populating excited states. On the contrary, allowing recombination to excited states in helium increases optical line strengths, suggesting that recombination contributes significantly to the population of excited states.

4.3 Results

Panels A and B of Figure 4.1 show the structure of a sample model (MS38) from B17 at 200 days past explosion, zoomed in to show the hydrogen-rich region. The stripped material occupies a conical section of the remnant from which the nickel-rich ejecta have been pushed away. There is no mixing of the stripped material with the nickel-rich ejecta except near the interface. Gamma-rays from ^{56}Co decay enter the hydrogen-rich region and deposit their energy there. Owing to high densities in this region, recombination is efficient against non-thermal collisional ionization and, consequently, hydrogen stays in a mostly neutral state.

Panels C and D of Figure 4.1 show the MS38-based synthetic nebular spectrum at 200 days at optical and near-infrared (NIR) wavelengths, respectively. At that time, the peak Hα flux is very strong, comparable to the prominent [Fe III] λ4658 emission line from the SN ejecta. In addition, permitted helium transitions are visible in the optical. In the near-infrared, lines from the Hydrogen Paschen series are conspicuous, along with narrow emission from forbidden iron-group lines.

The luminosity of our calculated Hα emission is higher than that of previous parameterized 1D models (Lundqvist et al., 2013; Mattila et al., 2005). We attribute this to the more realistic geometry in our multi-D calculations. In the previous works, stripped material was assumed to occupy a spherically symmetric central region of constant density. However, the hydrodynamical models show that stripped material is concentrated in a smaller volume clump that is offset from the ejecta center. The density of the hydrogen-rich material is higher, leading to a more effectively trapping of gamma-rays. As there is only minimal

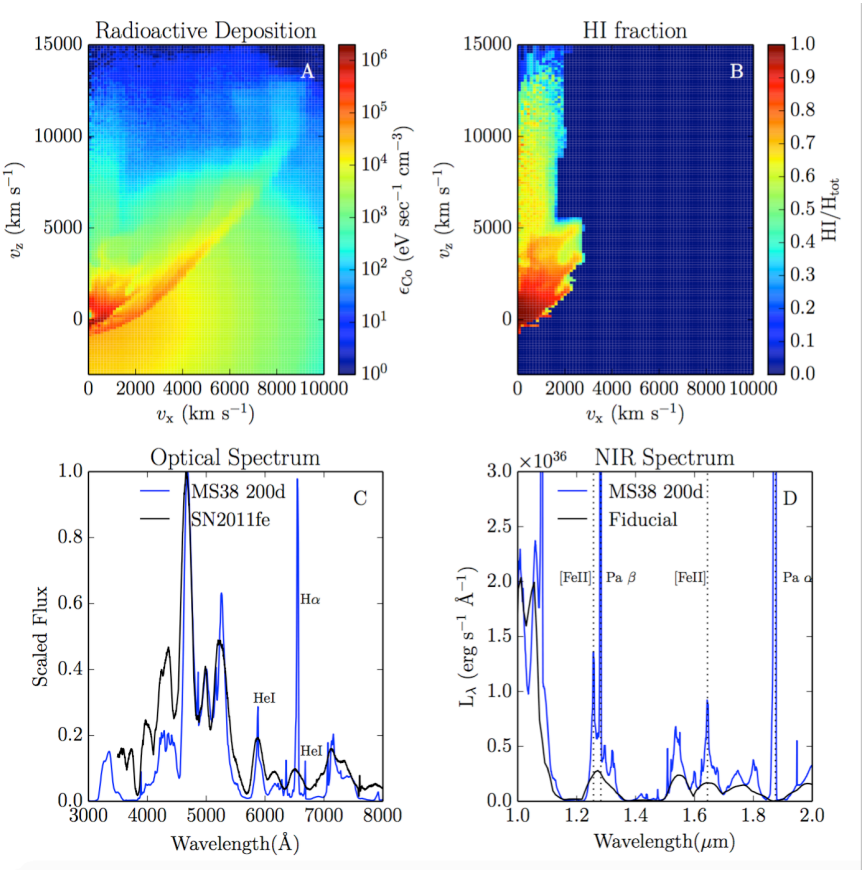

Figure 4.1: Properties of the MS38 model at 200 days past explosion, zoomed in to show the region of mass stripped from the companion. Panel (A) shows the deposition of energy from ^{56}Co decay throughout the ejecta, strongest in the region of stripped material at low velocities into which gamma-rays have penetrated from surrounding ^{56}Co-rich regions. Panel (B) shows the calculated fraction of neutral hydrogen to total hydrogen. Dark-blue regions contain less than 1% H by mass. The region near the core has high density, thus strong recombination. Panel (C) shows the synthetic optical spectrum of the MS38 model. Hα is prominent next to the normal forbidden iron and cobalt features, and permitted He I lines are also visible. Panel (D) shows the synthetic NIR spectrum of the MS38 model. The fiducial model from Botyánszki and Kasen, (2017) is included in black for reference. Dotted lines identify the following transitions: [Fe II] 12.257 μm, H I 1.2820 μm (Pβ), [Fe II] 1.6440 μm, H I 1.8750 μm (Pα). He I emission is also prominent at 1.085 μm. Line profiles in the MS38 model are more peaked than in the fiducial model, and narrow hydrogen Paschen emission dominates the NIR spectrum.

Table 4.1: Derived properties of the B17 models. $M_{\rm st}$ refers to the mass of material stripped from the companion (taken from Boehner, Plewa, and Langer, 2017). $L_{\rm H\alpha}/L_{4658}$ is the ratio of peak flux of Hα to that of [Fe III] λ4658, not necessarily at line center. All luminosities reported are calculated at 200 days past explosion.

Model Name	$M_{\rm st}$ ($M_\odot$)	$L_{\rm H\alpha}$ (10^{39} erg s^{-1})	$L_{\rm H\alpha}/L_{4658}$
MS38	0.25	6.8	0.98
MS7	0.37	9.3	1.43
MS54	0.32	15.7	1.04
MS63	0.24	7.0	1.23
SG	0.17	5.6	0.82
RG319	0.28	4.5	0.84
RG428	0.33	8.7	1.08

mixing with nickel-rich ejecta, this region cools primarily through hydrogen and helium line transitions.

Table 4.1 shows the calculated properties of the B17 models. Hα emission is strong and detectable for all of the models, regardless of whether the companion is a MS, SG, or RG star. To quantify this, we calculate the ratio of peak luminosity of Hα to that of [Fe III] λ4658 and find $L_{\rm H\alpha}/L_{4658} > 0.8$ for all models. This prominent Balmer emission is inconsistent with observations of normal SNe Ia and and so rules out progenitor scenarios with such high stripped masses. We find that the relative strength of the Hα emission is approximately constant over time, with $L_{\rm H\alpha}/L_{4658}$ decreasing by $\lesssim 20\%$ from 200 to 500 days after explosion.

4.3.1 Reduced Mass Models

The above models assumed a hydrogen companion in a semidetached system and an idealized, spherically symmetric W7-like explosion model. The total mass of stripped companion material, however, is found to be lower if the SN explosion energy is decreased or the orbital separation distance is increased (Liu et al., 2012; Pakmor et al., 2008; Pan, Ricker, and Taam, 2012). In addition, inhomogeneities in the ejecta structure may disturb the flow and potentially affect the amount of stripped material (Hansen et al., 2007).

Nondetections of Hα in observed SN Ia nebular spectra clearly constrain the allowed mass of stripped material. However, converting the observed flux limit to quantitative mass constraints has been hampered by the lack of detailed nebular modeling. Here we probe the sensitivity of the Hα flux to the amount of stripped material by gradually reducing the density in regions of the MS38 model that contain at least 1% hydrogen by mass. This simplified method should capture the basic effect of lowering the amount of stripped mass while retaining the characteristic asymmetry of the hydrodynamical interaction.

Figure 4.2 shows the Hα model luminosity for a series of MS38 models with reduced density, along with the original set of B17 models. For the set of modified MS38 models we find that the Hα model luminosity approximately varies with the stripped mass as

$$\log_{10}(L_{\mathrm{H}\alpha}) = -0.2M_1^2 + 0.17M_1 + 40.0, \tag{4.1}$$

where $M_1 = \log_{10}(M_{\mathrm{st}}/M_\odot)$ and $[L_{\mathrm{H}\alpha}] = \mathrm{erg\ s^{-1}}$. We stress that this approximate relation holds only for our scaled MS38 models, and does not take into account how the stripped mass geometry may vary with separation distance, SN ejecta properties, or companion type.

We estimate that the Hα luminosity accounts for about 30% of the total energy deposited in the stripped material for $M_{\mathrm{st}} > 0.01M_\odot$, and scales with total deposition. At lower masses, hydrogen is more ionized and only accounts for about 10% of total deposition energy.

For reference, the Hα luminosity upper bound for SN 2011fe (Shappee et al., 2013) is marked with a horizontal dashed line in Figure 4.2, scaled to account for the time difference between our models (200 days past explosion) and their observations (292 days past explosion). Since we find the Hα luminosity to be a relatively constant fraction of bolometric luminosity, we can scale the Hα limit of SN 2011fe using its bolometric light curve (Mazzali et al., 2015), in which there is roughly a factor of $\sim$4 decrease in luminosity between 200 and 292 days. Compared to our reduced mass models, the nondetection suggests a constraint on the stripped mass of $\lesssim 10^{-4}\ M_\odot$. This is a factor of about 5 lower than the constraint derived by Shappee et al., (2013) based on parameterized 1D models.

4.3.2 Effect of Viewing Angle

The asymmetry of companion-stripped material introduces a viewing angle dependence of the narrow emission-line profiles. Figure 4.3 shows the synthetic nebular spectrum of the day 200 MS38 model as observed from a number of viewing angles. While the total integrated luminosity of Hα is independent of viewing angle in optically thin ejecta, the line profiles do depend on the orientation. At $\theta = 0°$, the bulk of stripped material is moving toward the observer, resulting in a blueshifted Hα peak. For $\theta = 180°$, that region is moving away from the observer and the Hα peak is redshifted. For intermediate angles, the feature is broader and has lower peak luminosity. In general, we expect that the Hα peak will be shifted by $\sim$ 10 Å from its rest wavelength owing to orientation effects, which should be taken into account when trying to extract flux limits from observational data.

4.3.3 Helium-only Models

In addition to the hydrogen-rich systems considered by B17, helium-star companion models have been proposed to explain SNe Ia (Iben and Tutukov, 1984; Wang and Han, 2009; Wang et al., 2009; Yoon and Langer, 2003). For such companions, hydrodynamical models of interaction with the ejecta predict that up to 0.06 $M_\odot$ of companion mass becomes unbound (Liu et al., 2013; Pan, Ricker, and Taam, 2010, 2012). We explore such a scenario by

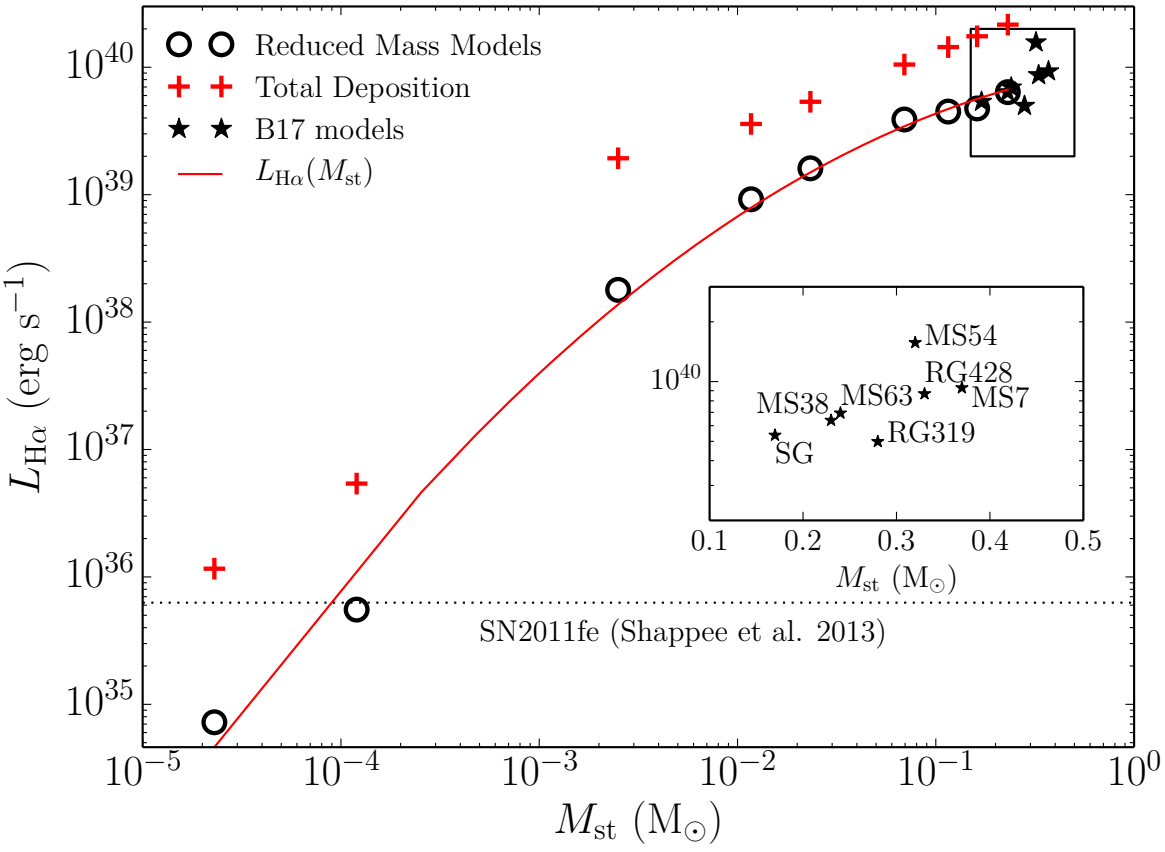

Figure 4.2: Hα luminosity for various models as a function of stripped mass. Open circles denote the amount of stripped mass in a series of modified MS38 models, while filled stars label the original B17 models. Red plus symbols indicate the total energy deposited into the stripped material for each value of stripped mass. We found a close correlation between the amount of stripped mass in the original B17 models and their estimated Hα luminosities, which suggests that such dependence is a common characteristic of SNe Ia in the SD scenario. The Hα luminosity upper limit for SN 2011fe (Shappee et al., 2013) is marked with a horizontal dashed line, scaled to the luminosity expected at 200 days past explosion (see text).

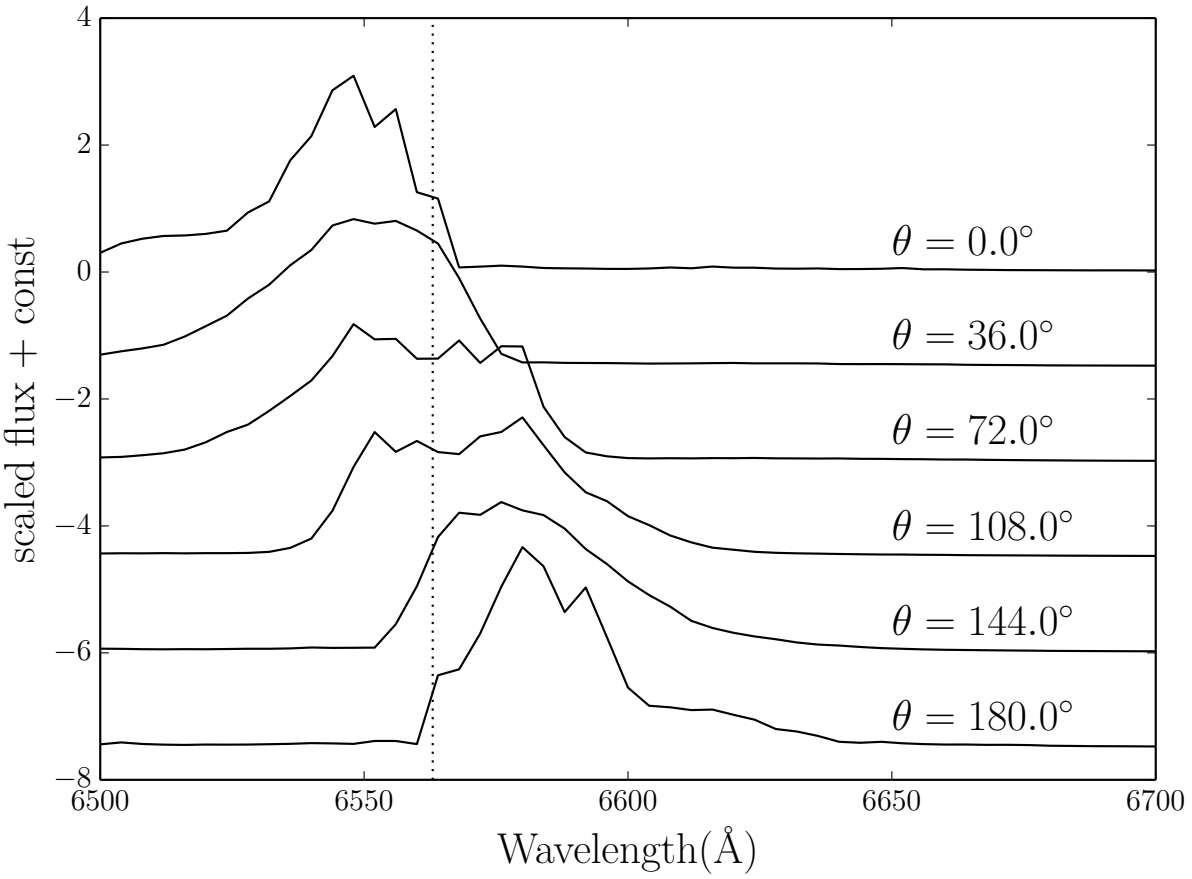

Figure 4.3: Synthetic Hα profiles of the MS38 model obtained for multiple viewing angles. Line shifts are clear from comparison with the Hα line center, shown with a dotted line. Note that the line profile is also affected by the viewing angle.

replacing all hydrogen with helium in the solar-abundance stripped material of model M38. While such a modified model overestimates the amount of stripped mass by a factor of $\gtrsim 4$ and possibly inaccurately reflects the geometry of the stripped material, it does provide a first estimate of an *upper bound* on the line emission from SD progenitors with helium companions.

Figure 4.4 shows the MS38 model with all stripped hydrogen replaced by helium. We find strong permitted helium emission at both optical and NIR wavelengths. In addition, narrow emission lines from [Ca II] and [Fe II] are visible atop broader components of line emission from the SN ejecta. The results suggest that even if the stripped helium mass is lower by a factor of 4 or more, high-resolution nebular spectra can provide strong constraints of helium-star SD progenitor models.

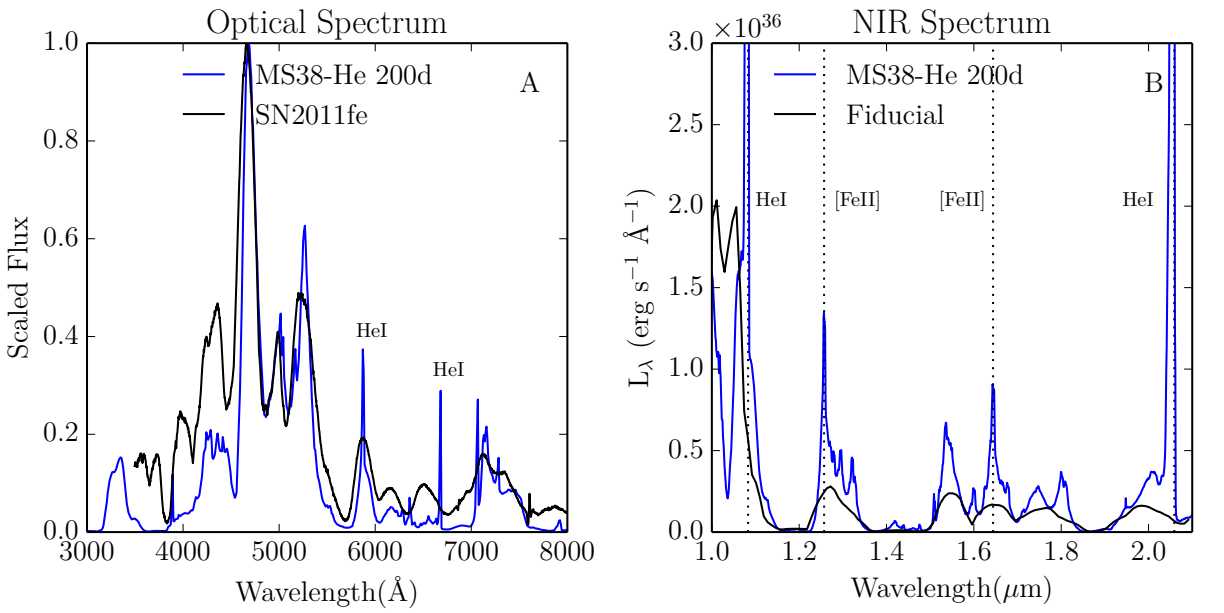

Figure 4.4: Synthetic spectra of the MS38 model at 200 days past explosion with all hydrogen replaced by helium. Panel (A) shows the optical spectrum, which contains visible He I optical emission at He I λ5875, 6678. Panel (B) shows the synthetic NIR spectrum, which contains visible [Fe II] and He I emission features. The fiducial model from Botyánszki and Kasen, (2017) is included in black for reference. Dotted lines identify the following transitions: He I 1.085 μm, [Fe II] 12.257 μm, [Fe II] 1.644 μm, He I 2.059 μm. Line profiles are more peaked than in the fiducial model, and narrow He I emission dominates the NIR spectrum.

4.4 Discussion

We have presented synthetic nebular spectra of multidimensional companion-ejecta interaction models in binary systems representing classic SD progenitors of SNe Ia. We found that the late-time Hα emission in SN Ia models with hydrogen-rich companions (regardless of whether MS, SG, or RG type), which results in $\gtrsim 0.1\ M_\odot$ of unbound solar-abundance ejecta, is strong compared to the limits derived from observed spectra. The Hα emission in our realistic models is even stronger than that found in previous parameterized 1D studies. We therefore disfavor semidetached binary systems with hydrogen-rich companions as viable SN Ia progenitors.

By artificially reducing the mass of the stripped region, we estimated that even an order of magnitude less of stripped, hydrogen-rich material (i.e., $\sim 0.01\ M_\odot$) would still be observationally detectable. Consequently, we place a strong limit of $M_{\rm st} \lesssim 1 \times 10^{-4}\ M_\odot$ on the hydrogen mass for SN2011fe (Shappee et al., 2013), assuming that our models are representative of the geometry of stripped material. This constraint is a factor of 5 stronger

than that derived by Shappee et al., (2013) based on parameterized 1D models.

For SD scenarios to be consistent with the nondetection of Hα in normal SNe Ia requires much smaller stripped hydrogen masses. This may be possible if the ratio of the binary separation distance (a) to the companion star radius (R) is larger than the value $a/R \approx 3$ adopted for the Roche-lobe-filling orbital geometry of the B17 models. For larger a/R, the solid angle subtended by the companion is smaller, and a smaller fraction of the ejecta is intercepted. Based on the scalings of Liu et al., (2012), the stripped mass may be consistent with $\lesssim 10^{-4}\ M_\odot$ if $a/R \gtrsim 20$. Certain scenarios, such as the spin-up/spin-down models of Di Stefano, Voss, and Claeys, (2011) and Justham, (2011), posit a delay between accretion and explosion during which the companion can shrink by orders of magnitude in radius.

For SD scenarios involving a nondegenerate helium-star companion, the interaction with the ejecta results in a lower amount of stripped mass, $\sim 0.06\ M_\odot$ (Liu et al., 2013; Pan, Ricker, and Taam, 2010, 2012). Our rather speculative MS38-based helium-only model still showed significant He I spectral features. As our modified model contained about 4 times more mass of stripped helium than found in actual simulations, we consider our helium emission estimates as an upper bound to the emission detectable from more realistic models.

Future work should consider a broader range of hydrodynamical models, as the B17 sample exclusively considers SD, Roche-lobe filling, hydrogen-rich companions. Both the orbital geometry (wider systems) and companion type (helium star) should be considered in more detail. An idealized, spherically symmetric W7 explosion model provides for smooth, steady flow of ejecta around the companion. However, realistic SN Ia explosion models will likely produce ejecta characterized by density inhomogeneities that will perturb the interaction region, potentially enhancing the stripping process (Hansen et al., 2007). Finally, the limitations in input atomic data and the approximations in the treatment of atomic processes and radiative transfer effects discussed in Botyánszki and Kasen, (2017) influence nebular spectral modeling and should be addressed in future studies.

Bibliography

[1] S. A. Abdel-Naby et al. "Dielectronic recombination data for dynamic finite-density plasmas. XIV. The aluminum isoelectronic sequence". In: A&A 537, A40 (Jan. 2012), A40. DOI: 10.1051/0004-6361/201117544.

[2] S. M. V. Aldrovandi and D. Pequignot. "Erratum; Radiative and Dielectronic Recombination Coefficients for Complex Ions". In: A&A 47 (Mar. 1976), p. 321.

[3] S. M. V. Aldrovandi and D. Pequignot. "Radiative and Dielectronic Recombination Coefficients for Complex Ions". In: A&A 25 (May 1973), p. 137.

[4] C. W. Allen. *Astrophysical quantities*. 1963.

[5] Z. Altun et al. "Dielectronic recombination data for dynamic finite-density plasmas. VI. The boron isoelectronic sequence". In: A&A 420 (June 2004), pp. 775–781. DOI: 10.1051/0004-6361:20040964.

[6] Z. Altun et al. "Dielectronic recombination data for dynamic finite-density plasmas. XI. The sodium isoelectronic sequence". In: A&A 447 (Mar. 2006), pp. 1165–1174. DOI: 10.1051/0004-6361:20053278.

[7] Z. Altun et al. "Dielectronic recombination data for dynamic finite-density plasmas. XIII. The magnesium isoelectronic sequence". In: A&A 474 (Nov. 2007), pp. 1051–1059. DOI: 10.1051/0004-6361:20078238.

[8] Z. Altun et al. "Erratum: Dielectronic recombination data for dynamic finite-density plasmas. VI. The boron isoelectronic sequence". In: A&A 433 (Apr. 2005), pp. 395–395. DOI: 10.1051/0004-6361:20040003e.

[9] M. Arnaud and J. Raymond. "Iron ionization and recombination rates and ionization equilibrium". In: ApJ 398 (Oct. 1992), pp. 394–406. DOI: 10.1086/171864.

[10] M. Arnaud and J. Raymond. "Iron ionization and recombination rates and ionization equilibrium". In: ApJ 398 (Oct. 1992), pp. 394–406. DOI: 10.1086/171864.

[11] M. Arnaud and R. Rothenflug. "An updated evaluation of recombination and ionization rates". In: A&AS 60 (June 1985), pp. 425–457.

[12] M. Arnaud and R. Rothenflug. "An updated evaluation of recombination and ionization rates". In: A&AS 60 (June 1985), pp. 425–457.

[13] W. D. Arnett. "A Possible Model of Supernovae: Detonation of ^{12}C". In: Ap&SS 5 (Oct. 1969), pp. 180–212. DOI: 10.1007/BF00650291.

[14] C. Ashall et al. "Abundance stratification in Type Ia supernovae - V. SN 1986G bridging the gap between normal and subluminous SNe Ia". In: MNRAS 463 (Dec. 2016), pp. 1891–1906. DOI: 10.1093/mnras/stw2114. arXiv: 1608.05244 [astro-ph.HE].

[15] T. S. Axelrod. "Late time optical spectra from the Ni-56 model for Type 1 supernovae". PhD thesis. California Univ., Santa Cruz., 1980.

[16] W. Baade and F. Zwicky. "Photographic Light-Curves of the Two Supernovae in IC 4182 and NGC 1003." In: ApJ 88 (Nov. 1938), p. 411. DOI: 10.1086/143996.

[17] N. R. Badnell. "Radiative Recombination Data for Modeling Dynamic Finite-Density Plasmas". In: ApJS 167 (Dec. 2006), pp. 334–342. DOI: 10.1086/508465. eprint: astro-ph/0604144.

[18] M. A. Bautista and N. R. Badnell. "Dielectronic recombination data for dynamic finite-density plasmas. XII. The helium isoelectronic sequence". In: A&A 466 (May 2007), pp. 755–762. DOI: 10.1051/0004-6361:20077056.

[19] W. Benz, F.-K. Thielemann, and J. G. Hills. "Three-dimensional hydrodynamical simulations of stellar collisions. II - White dwarfs". In: ApJ 342 (July 1989), pp. 986–998. DOI: 10.1086/167656.

[20] I. F. Bikmaev et al. "Type Ia supernovae 2014J and 2011fe at the nebular phase". In: *Astronomy Letters* 41 (Dec. 2015), pp. 785–796. DOI: 10.1134/S1063773715120014.

[21] C. S. Black, R. A. Fesen, and J. T. Parrent. "Progressive redshifts in the late-time spectra of Type Ia supernovae". In: MNRAS 462 (Oct. 2016), pp. 649–662. DOI: 10.1093/mnras/stw1680. arXiv: 1604.01044 [astro-ph.HE].

[22] P. Boehner, T. Plewa, and N. Langer. "Imprints of the ejecta-companion interaction in Type Ia supernovae: main-sequence, subgiant, and red giant companions". In: MNRAS 465 (Feb. 2017), pp. 2060–2075. DOI: 10.1093/mnras/stw2737. arXiv: 1612.04684 [astro-ph.SR].

[23] J. Botyánszki and D. Kasen. "How Do Type Ia Supernova Nebular Spectra Depend on Explosion Properties? Insights from Systematic Non-LTE Modeling". In: ApJ 845, 176 (Aug. 2017), p. 176. DOI: 10.3847/1538-4357/aa81d8. arXiv: 1704.06275 [astro-ph.HE].

[24] D. Branch, A. Fisher, and P. Nugent. "On the relative frequencies of spectroscopically normal and peculiar type IA supernovae". In: AJ 106 (Dec. 1993), pp. 2383–2391. DOI: 10.1086/116810.

[25] D. Branch and A. M. Khokhlov. "Type Ia supernovae: observations, modeling, distances." In: Phys. Rep. 256 (May 1995), pp. 53–67. DOI: 10.1016/0370-1573(94)00101-8.

[26] E. Bravo et al. "Pulsating Reverse Detonation Models of Type Ia Supernovae. II. Explosion". In: ApJ 695 (Apr. 2009), pp. 1257–1272. DOI: 10.1088/0004-637X/695/2/1257. arXiv: 0901.3013 [astro-ph.SR].

[27] D. A. Chamulak et al. "The Reduction of the Electron Abundance during the Pre-explosion Simmering in White Dwarf Supernovae". In: ApJ 677, 160-168 (Apr. 2008), pp. 160–168. DOI: 10.1086/528944. arXiv: 0801.1643.

[28] S. Chandrasekhar. "The Maximum Mass of Ideal White Dwarfs". In: ApJ 74 (July 1931), p. 81. DOI: 10.1086/143324.

[29] R. A. Chevalier and N. Soker. "Asymmetric envelope expansion of supernova 1987A". In: ApJ 341 (June 1989), pp. 867–882. DOI: 10.1086/167545.

[30] M. J. Childress et al. "Measuring nickel masses in Type Ia supernovae using cobalt emission in nebular phase spectra". In: MNRAS 454 (Dec. 2015), pp. 3816–3842. DOI: 10.1093/mnras/stv2173. arXiv: 1507.02501 [astro-ph.HE].

[31] N. N. Chugai. "Possible Binary Nature of Peculiar Type-I Supernovae - is the Satellite a Red Supergiant". In: Soviet Ast. 30 (Oct. 1986), p. 563.

[32] J. Colgan, M. S. Pindzola, and N. R. Badnell. "Dielectronic recombination data for dynamic finite-density plasmas. V: The lithium isoelectronic sequence". In: A&A 417 (Apr. 2004), pp. 1183–1188. DOI: 10.1051/0004-6361:20034197.

[33] J. Colgan, M. S. Pindzola, and N. R. Badnell. "Erratum: Dielectronic recombination data for dynamic finite-density plasmas. V. The lithium isoelectronic sequence". In: A&A 429 (Jan. 2005), p. 369. DOI: 10.1051/0004-6361:20042105.

[34] J. Colgan et al. "Dielectronic recombination data for dynamic finite-density plasmas. III. The beryllium isoelectronic sequence". In: A&A 412 (Dec. 2003), pp. 597–601. DOI: 10.1051/0004-6361:20031362.

[35] S. A. Colgate and C. McKee. "Early Supernova Luminosity". In: ApJ 157 (Aug. 1969), p. 623. DOI: 10.1086/150102.

[36] W. Cunto et al. "Topbase at the CDS". In: A&A 275 (Aug. 1993), p. L5.

[37] M. de Kool, H. Li, and R. McCray. "Thermal Evolution of the Envelope of SN 1987A". In: ApJ 503 (Aug. 1998), pp. 857–876. DOI: 10.1086/306016.

[38] G. Del Zanna et al. "CHIANTI - An atomic database for emission lines. Version 8". In: A&A 582, A56 (Oct. 2015), A56. DOI: 10.1051/0004-6361/201526827. arXiv: 1508.07631 [astro-ph.SR].

[39] G. Del Zanna et al. "CHIANTI - An atomic database for emission lines. Version 8". In: A&A 582, A56 (Oct. 2015), A56. DOI: 10.1051/0004-6361/201526827. arXiv: 1508.07631 [astro-ph.SR].

[40] K. P. Dere. "Ionization rate coefficients for the elements hydrogen through zinc". In: A&A 466 (May 2007), pp. 771–792. DOI: 10.1051/0004-6361:20066728.

[41] K. P. Dere et al. "CHIANTI - an atomic database for emission lines". In: A&AS 125 (Oct. 1997). DOI: 10.1051/aas:1997368.

[42] K. P. Dere et al. "CHIANTI - an atomic database for emission lines. IX. Ionization rates, recombination rates, ionization equilibria for the elements hydrogen through zinc and updated atomic data". In: A&A 498 (May 2009), pp. 915–929. DOI: 10.1051/0004-6361/200911712.

[43] L. Dessart and D. J. Hillier. "Non-LTE time-dependent spectroscopic modelling of Type II-plateau supernovae from the photospheric to the nebular phase: case study for 15 and 25 $M_\odot$ progenitor stars". In: MNRAS 410 (Jan. 2011), pp. 1739–1760. DOI: 10.1111/j.1365-2966.2010.17557.x. arXiv: 1008.3238 [astro-ph.SR].

[44] L. Dessart and D. J. Hillier. "Supernova radiative-transfer modelling: a new approach using non-local thermodynamic equilibrium and full time dependence". In: MNRAS 405 (July 2010), pp. 2141–2160. DOI: 10.1111/j.1365-2966.2010.16611.x. arXiv: 1003.2557 [astro-ph.SR].

[45] R. Di Stefano, R. Voss, and J. S. W. Claeys. "Spin-up/Spin-down Models for Type Ia Supernovae". In: ApJ 738, L1 (Sept. 2011), p. L1. DOI: 10.1088/2041-8205/738/1/L1. arXiv: 1102.4342 [astro-ph.HE].

[46] B. Dilday et al. "PTF 11kx: A Type Ia Supernova with a Symbiotic Nova Progenitor". In: *Science* 337 (Aug. 2012), p. 942. DOI: 10.1126/science.1219164. arXiv: 1207.1306.

[47] G. Dimitriadis et al. "The late-time light curve of the type Ia supernova SN 2011fe". In: *ArXiv e-prints* (Jan. 2017). arXiv: 1701.07267 [astro-ph.HE].

[48] G. J. Ferland et al. "Anisotropic line emission and the geometry of the broad-line region in active galactic nuclei". In: ApJ 387 (Mar. 1992), pp. 95–108. DOI: 10.1086/171063.

[49] A. V. Filippenko. "Optical Spectra of Supernovae". In: ARA&A 35 (1997), pp. 309–355. DOI: 10.1146/annurev.astro.35.1.309.

[50] A. V. Filippenko et al. "The peculiar Type IA SN 1991T - Detonation of a white dwarf?" In: ApJ 384 (Jan. 1992), pp. L15–L18. DOI: 10.1086/186252.

[51] A. V. Filippenko et al. "The subluminous, spectroscopically peculiar type IA supernova 1991bg in the elliptical galaxy NGC 4374". In: AJ 104 (Oct. 1992), pp. 1543–1556. DOI: 10.1086/116339.

[52] M. Fink, W. Hillebrandt, and F. K. Röpke. "Double-detonation supernovae of sub-Chandrasekhar mass white dwarfs". In: A&A 476 (Dec. 2007), pp. 1133–1143. DOI: 10.1051/0004-6361:20078438. arXiv: 0710.5486.

[53] G. Folatelli et al. "SN 2005bf: A Possible Transition Event between Type Ib/c Supernovae and Gamma-Ray Bursts". In: ApJ 641 (Apr. 2006), pp. 1039–1050. DOI: 10.1086/500531. eprint: astro-ph/0509731.

[54] R. J. Foley et al. "Type Iax Supernovae: A New Class of Stellar Explosion". In: ApJ 767, 57 (Apr. 2013), p. 57. DOI: 10.1088/0004-637X/767/1/57. arXiv: 1212.2209 [astro-ph.SR].

[55] C. Fransson and A. Jerkstrand. "Reconciling the Infrared Catastrophe and Observations of SN 2011fe". In: ApJ 814, L2 (Nov. 2015), p. L2. DOI: 10.1088/2041-8205/814/1/L2. arXiv: 1511.00245 [astro-ph.SR].

[56] C. Fransson and C. Kozma. "The freeze-out phase of SN 1987A - Implications for the light curve". In: ApJ 408 (May 1993), pp. L25–L28. DOI: 10.1086/186822.

[57] B. Friesen et al. "Optical and ultraviolet spectroscopic analysis of SN 2011fe at late times". In: MNRAS (Jan. 2017). DOI: 10.1093/mnras/stx241. arXiv: 1607.04784 [astro-ph.SR].

[58] V. N. Gamezo, A. M. Khokhlov, and E. S. Oran. "Three-dimensional Delayed-Detonation Model of Type Ia Supernovae". In: ApJ 623 (Apr. 2005), pp. 337–346. DOI: 10.1086/428767. eprint: astro-ph/0409598.

[59] D. García-Senz et al. "High-resolution simulations of the head-on collision of white dwarfs". In: MNRAS 436 (Dec. 2013), pp. 3413–3429. DOI: 10.1093/mnras/stt1821. arXiv: 1309.6884 [astro-ph.SR].

[60] C. L. Gerardy et al. "Signatures of Delayed Detonation, Asymmetry, and Electron Capture in the Mid-Infrared Spectra of Supernovae 2003hv and 2005df". In: ApJ 661 (June 2007), pp. 995–1012. DOI: 10.1086/516728. eprint: astro-ph/0702117.

[61] O. Gnat and G. J. Ferland. "Ion-by-ion Cooling Efficiencies". In: ApJS 199, 20 (Mar. 2012), p. 20. DOI: 10.1088/0067-0049/199/1/20. arXiv: 1111.6980 [astro-ph.IM].

[62] I. Golombek and J. C. Niemeyer. "A model for multidimensional delayed detonations in SN Ia explosions". In: A&A 438 (Aug. 2005), pp. 611–616. DOI: 10.1051/0004-6361:20042402. eprint: astro-ph/0503617.

[63] M. L. Graham et al. "PTF11kx: A Type Ia Supernova with Hydrogen Emission Persisting after 3.5 Years". In: ApJ 843, 102 (July 2017), p. 102. DOI: 10.3847/1538-4357/aa78ee. arXiv: 1706.02266 [astro-ph.HE].

[64] J. Guillochon et al. "Surface Detonations in Double Degenerate Binary Systems Triggered by Accretion Stream Instabilities". In: ApJ 709 (Jan. 2010), pp. L64–L69. DOI: 10.1088/2041-8205/709/1/L64. arXiv: 0911.0416 [astro-ph.HE].

[65] J. F. Hansen et al. "Experiment on the Mass Stripping of an Interstellar Cloud Following Shock Passage". In: ApJ 662 (June 2007), pp. 379–388. DOI: 10.1086/514804.

[66] C. E. Harris, P. E. Nugent, and D. N. Kasen. "Against the Wind: Radio Light Curves of Type Ia Supernovae Interacting with Low-density Circumstellar Shells". In: ApJ 823, 100 (June 2016), p. 100. DOI: 10.3847/0004-637X/823/2/100. arXiv: 1604.00019 [astro-ph.HE].

[67] M. Hicken et al. "The Luminous and Carbon-rich Supernova 2006gz: A Double Degenerate Merger?" In: ApJ 669 (Nov. 2007), pp. L17–L20. DOI: 10.1086/523301. arXiv: 0709.1501.

[68] W. Hillebrandt and J. C. Niemeyer. "Type IA Supernova Explosion Models". In: ARA&A 38 (2000), pp. 191–230. DOI: 10.1146/annurev.astro.38.1.191. eprint: astro-ph/0006305.

[69] W. Hillebrandt et al. "Towards an understanding of Type Ia supernovae from a synthesis of theory and observations". In: *Frontiers of Physics* 8 (Apr. 2013), pp. 116–143. DOI: 10.1007/s11467-013-0303-2. arXiv: 1302.6420 [astro-ph.CO].

[70] D. J. Hillier and D. L. Miller. "The Treatment of Non-LTE Line Blanketing in Spherically Expanding Outflows". In: ApJ 496 (Mar. 1998), pp. 407–427. DOI: 10.1086/305350.

[71] P. Höflich et al. "Signature of Electron Capture in Iron-rich Ejecta of SN 2003du". In: ApJ 617 (Dec. 2004), pp. 1258–1266. DOI: 10.1086/425571. eprint: astro-ph/0409185.

[72] D. A. Howell. "Type Ia supernovae as stellar endpoints and cosmological tools". In: *Nature Communications* 2, 350 (June 2011), p. 350. DOI: 10.1038/ncomms1344. arXiv: 1011.0441 [astro-ph.CO].

[73] D. A. Howell et al. "The type Ia supernova SNLS-03D3bb from a super-Chandrasekhar-mass white dwarf star". In: Nature 443 (Sept. 2006), pp. 308–311. DOI: 10.1038/nature05103. eprint: astro-ph/0609616.

[74] F. Hoyle and W. A. Fowler. "Nucleosynthesis in Supernovae." In: ApJ 132 (Nov. 1960), p. 565. DOI: 10.1086/146963.

[75] D. G. Hummer et al. "Atomic data from the IRON Project. 1: Goals and methods". In: A&A 279 (Nov. 1993), pp. 298–309.

[76] I. Iben Jr. and A. V. Tutukov. "Supernovae of type I as end products of the evolution of binaries with components of moderate initial mass (M not greater than about 9 solar masses)". In: ApJS 54 (Feb. 1984), pp. 335–372. DOI: 10.1086/190932.

[77] K. Iwamoto et al. "Nucleosynthesis in Chandrasekhar Mass Models for Type IA Supernovae and Constraints on Progenitor Systems and Burning-Front Propagation". In: ApJS 125 (Dec. 1999), pp. 439–462. DOI: 10.1086/313278. eprint: astro-ph/0002337.

[78] J. T. Jefferies. *Spectral line formation*. 1968.

[79] A. Jerkstrand, C. Fransson, and C. Kozma. "The ^{44}Ti-powered spectrum of SN 1987A". In: A&A 530, A45 (June 2011), A45. DOI: 10.1051/0004-6361/201015937. arXiv: 1103.3653 [astro-ph.HE].

[80] A. Jerkstrand et al. "Late-time spectral line formation in Type IIb supernovae, with application to SN 1993J, SN 2008ax, and SN 2011dh". In: A&A 573, A12 (Jan. 2015), A12. DOI: 10.1051/0004-6361/201423983. arXiv: 1408.0732 [astro-ph.HE].

[81] G. C. Jordan IV et al. "The Detonation Mechanism of the Pulsationally Assisted Gravitationally Confined Detonation Model of Type Ia Supernovae". In: ApJ 759, 53 (Nov. 2012), p. 53. DOI: 10.1088/0004-637X/759/1/53. arXiv: 1202.3997 [astro-ph.HE].

[82] G. C. Jordan IV et al. "Three-Dimensional Simulations of the Deflagration Phase of the Gravitationally Confined Detonation Model of Type Ia Supernovae". In: ApJ 681, 1448-1457 (July 2008), pp. 1448–1457. DOI: 10.1086/588269. eprint: astro-ph/0703573.

[83] S. Justham. "Single-degenerate Type Ia Supernovae Without Hydrogen Contamination". In: ApJ 730, L34 (Apr. 2011), p. L34. DOI: 10.1088/2041-8205/730/2/L34. arXiv: 1102.4913 [astro-ph.SR].

[84] D. Kasen. "Seeing the Collision of a Supernova with Its Companion Star". In: ApJ 708 (Jan. 2010), pp. 1025–1031. DOI: 10.1088/0004-637X/708/2/1025. arXiv: 0909.0275 [astro-ph.HE].

[85] D. Kasen, F. K. Röpke, and S. E. Woosley. "The diversity of type Ia supernovae from broken symmetries". In: Nature 460 (Aug. 2009), pp. 869–872. DOI: 10.1038/nature08256. arXiv: 0907.0708 [astro-ph.HE].

[86] D. Kasen, R. C. Thomas, and P. Nugent. "Time-dependent Monte Carlo Radiative Transfer Calculations for Three-dimensional Supernova Spectra, Light Curves, and Polarization". In: ApJ 651 (Nov. 2006), pp. 366–380. DOI: 10.1086/506190. eprint: astro-ph/0606111.

[87] R. Kashyap et al. "Spiral Instability Can Drive Thermonuclear Explosions in Binary White Dwarf Mergers". In: ApJ 800, L7 (Feb. 2015), p. L7. DOI: 10.1088/2041-8205/800/1/L7. arXiv: 1501.05645 [astro-ph.SR].

[88] M. M. Kasliwal et al. "Calcium-rich Gap Transients in the Remote Outskirts of Galaxies". In: ApJ 755, 161 (Aug. 2012), p. 161. DOI: 10.1088/0004-637X/755/2/161. arXiv: 1111.6109 [astro-ph.HE].

[89] W. E. Kerzendorf et al. "Very Late Photometry of SN 2011fe". In: ApJ 796, L26 (Dec. 2014), p. L26. DOI: 10.1088/2041-8205/796/2/L26. arXiv: 1406.6050 [astro-ph.SR].

[90] A. M. Khokhlov. "Delayed detonation model for type IA supernovae". In: A&A 245 (May 1991), pp. 114–128.

[91] C. Kozma and C. Fransson. "Gamma-ray deposition and nonthermal excitation in supernovae". In: ApJ 390 (May 1992), pp. 602–621. DOI: 10.1086/171311.

[92] C. Kozma and C. Fransson. "Late Spectral Evolution of SN 1987A. I. Temperature and Ionization". In: ApJ 496 (Mar. 1998), pp. 946–966. DOI: 10.1086/305409. eprint: astro-ph/9712223.

[93] C. Kozma and C. Fransson. "Late Spectral Evolution of SN 1987A. II. Line Emission". In: ApJ 497 (Apr. 1998), pp. 431–457. DOI: 10.1086/305452. eprint: astro-ph/9712224.

[94] C. Kozma et al. "Three-dimensional modeling of type Ia supernovae - The power of late time spectra". In: A&A 437 (July 2005), pp. 983–995. DOI: 10.1051/0004-6361:20053044. eprint: astro-ph/0504317.

[95] H. A. Kramers. "XCIII. On the theory of X-ray absorption and of the continuous X-ray spectrum". In: *Philosophical Magazine Series 6* 46.275 (1923), pp. 836–871. DOI: 10.1080/14786442308565244. eprint: http://dx.doi.org/10.1080/14786442308565244. URL: http://dx.doi.org/10.1080/14786442308565244.

[96] A. Kramida, Y. Ralchenko, and J. Reader. "Current Status of Atomic Spectroscopy Databases at NIST". In: *APS Division of Atomic, Molecular and Optical Physics Meeting Abstracts*. May 2016.

[97] M. Kromer et al. "3D deflagration simulations leaving bound remnants: a model for 2002cx-like Type Ia supernovae". In: MNRAS 429 (Mar. 2013), pp. 2287–2297. DOI: 10.1093/mnras/sts498. arXiv: 1210.5243 [astro-ph.HE].

[98] P. S. Krstic, P. C. Stancil, and D. R. Schultz. "Theoretical treatment of charge transfer processes of relevance to astrophysics". In: *NASA STI/Recon Technical Report N* 99 (Dec. 1997).

[99] M. J. Kuchner et al. "Evidence for Ni-56 yields Co-56 yields Fe-56 decay in type IA supernovae". In: ApJ 426 (May 1994), pp. 89–92. DOI: 10.1086/187347.

[100] D. Kushnir et al. "Head-on Collisions of White Dwarfs in Triple Systems Could Explain Type Ia Supernovae". In: ApJ 778, L37 (Dec. 2013), p. L37. DOI: 10.1088/2041-8205/778/2/L37. arXiv: 1303.1180 [astro-ph.HE].

[101] M. Landini and B. C. M. Fossi. "Ion equilibrium for minor components in a thin plasma". In: A&AS 91 (Nov. 1991), pp. 183–196.

[102] M. Landini and B. C. M. Fossi. "Ion equilibrium for minor components in a thin plasma". In: A&AS 91 (Nov. 1991), pp. 183–196.

[103] M. Landini and B. C. Monsignori Fossi. "The X-UV spectrum of thin plasmas". In: A&AS 82 (Feb. 1990), pp. 229–260.

[104] B. Leibundgut. "Type Ia Supernovae". In: A&A Rev. 10 (2000), pp. 179–209. DOI: 10.1007/s001590000009. eprint: astro-ph/0003326.

[105] G. Leloudas et al. "The normal Type Ia SN 2003hv out to very late phases". In: A&A 505 (Oct. 2009), pp. 265–279. DOI: 10.1051/0004-6361/200912364. arXiv: 0908.0537 [astro-ph.SR].

[106] D. C. Leonard. "Constraining the Type Ia Supernova Progenitor: The Search for Hydrogen in Nebular Spectra". In: ApJ 670 (Dec. 2007), pp. 1275–1282. DOI: 10.1086/522367. arXiv: 0710.3166.

[107] C. Li, D. J. Hillier, and L. Dessart. "Non-thermal excitation and ionization in supernovae". In: MNRAS 426 (Oct. 2012), pp. 1671–1686. DOI: 10.1111/j.1365-2966.2012.21198.x. arXiv: 1206.0215 [astro-ph.SR].

[108] H. Li and R. McCray. "The CA II emission lines of SN 1987A". In: ApJ 405 (Mar. 1993), pp. 730–737. DOI: 10.1086/172401.

[109] W. Liu, D. J. Jeffery, and D. R. Schultz. "Nebular Spectra of Type IA Supernovae". In: ApJ 483 (July 1997), pp. L107–L110. DOI: 10.1086/310752.

[110] Z. W. Liu et al. "Three-dimensional simulations of the interaction between Type Ia supernova ejecta and their main sequence companions". In: A&A 548, A2 (Dec. 2012), A2. DOI: 10.1051/0004-6361/201219357. arXiv: 1209.4458 [astro-ph.SR].

[111] Z.-W. Liu et al. "The Impact of Type Ia Supernova Explosions on Helium Companions in the Chandrasekhar-mass Explosion Scenario". In: ApJ 774, 37 (Sept. 2013), p. 37. DOI: 10.1088/0004-637X/774/1/37. arXiv: 1307.5579 [astro-ph.SR].

[112] E. Livne. "Successive detonations in accreting white dwarfs as an alternative mechanism for type I supernovae". In: ApJ 354 (May 1990), pp. L53–L55. DOI: 10.1086/185721.

[113] W. Lotz. "Electron-impact ionization cross-sections and ionization rate coefficients for atoms and ions from scandium to zinc". In: *Zeitschrift fur Physik* 220 (Oct. 1969), pp. 466–472. DOI: 10.1007/BF01394789.

[114] P. Lundqvist et al. "Hydrogen and helium in the spectra of Type Ia supernovae". In: MNRAS 435 (Oct. 2013), pp. 329–345. DOI: 10.1093/mnras/stt1303. arXiv: 1307.4099 [astro-ph.HE].

[115] P. Lundqvist et al. "No trace of a single-degenerate companion in late spectra of supernovae 2011fe and 2014J". In: A&A 577, A39 (May 2015), A39. DOI: 10.1051/0004-6361/201525719. arXiv: 1502.00589 [astro-ph.HE].

[116] R. Lunnan et al. "Two New Calcium-rich Gap Transients in Group and Cluster Environments". In: ApJ 836, 60 (Feb. 2017), p. 60. DOI: 10.3847/1538-4357/836/1/60. arXiv: 1612.00454 [astro-ph.HE].

[117] K. Maeda et al. "An asymmetric explosion as the origin of spectral evolution diversity in type Ia supernovae". In: Nature 466 (July 2010), pp. 82–85. DOI: 10.1038/nature09122. arXiv: 1006.5888.

[118] K. Maeda et al. "Nebular Spectra and Explosion Asymmetry of Type Ia Supernovae". In: ApJ 708 (Jan. 2010), pp. 1703–1715. DOI: 10.1088/0004-637X/708/2/1703. arXiv: 0911.5484 [astro-ph.SR].

[119] K. Maeda et al. "Nebular Spectra of SN 1998bw Revisited: Detailed Study by One- and Two-dimensional Models". In: ApJ 640 (Apr. 2006), pp. 854–877. DOI: 10.1086/500187. eprint: astro-ph/0508373.

[120] K. Maguire et al. "Searching for swept-up hydrogen and helium in the late-time spectra of 11 nearby Type Ia supernovae". In: MNRAS 457 (Apr. 2016), pp. 3254–3265. DOI: 10.1093/mnras/stv2991. arXiv: 1512.07107.

[121] D. Maoz, F. Mannucci, and G. Nelemans. "Observational Clues to the Progenitors of Type Ia Supernovae". In: ARA&A 52 (Aug. 2014), pp. 107–170. DOI: 10.1146/annurev-astro-082812-141031. arXiv: 1312.0628.

[122] E. Marietta, A. Burrows, and B. Fryxell. "Type IA Supernova Explosions in Binary Systems: The Impact on the Secondary Star and Its Consequences". In: ApJS 128 (June 2000), pp. 615–650. DOI: 10.1086/313392. eprint: astro-ph/9908116.

[123] H. Martínez-Rodríguez et al. "Neutronization During Carbon Simmering In Type Ia Supernova Progenitors". In: ApJ 825, 57 (July 2016), p. 57. DOI: 10.3847/0004-637X/825/1/57. arXiv: 1602.00673 [astro-ph.SR].

[124] S. Mattila et al. "Early and late time VLT spectroscopy of SN 2001el - progenitor constraints for a type Ia supernova". In: A&A 443 (Nov. 2005), pp. 649–662. DOI: 10.1051/0004-6361:20052731. eprint: astro-ph/0501433.

[125] M Mattioli et al. "Updating of ionization data for ionization balance evaluations of atoms and ions for the elements hydrogen to germanium". In: *Journal of Physics B: Atomic, Molecular and Optical Physics* 40.18 (2007), p. 3569. URL: http://stacks.iop.org/0953-4075/40/i=18/a=002.

[126] I. Maurer et al. "Hydrogen and helium in the late phase of supernovae of Type IIb". In: MNRAS 409 (Dec. 2010), pp. 1441–1454. DOI: 10.1111/j.1365-2966.2010.17186.x. arXiv: 1007.1881 [astro-ph.HE].

[127] I. Maurer et al. "NERO- a post-maximum supernova radiation transport code". In: MNRAS 418 (Dec. 2011), pp. 1517–1525. DOI: 10.1111/j.1365-2966.2011.19376.x. arXiv: 1105.3049 [astro-ph.HE].

[128] P. A. Mazzali and S. Hachinger. "The nebular spectra of the Type Ia supernova 1991bg: further evidence of a non-standard explosion". In: MNRAS 424 (Aug. 2012), pp. 2926–2935. DOI: 10.1111/j.1365-2966.2012.21433.x.

[129] P. A. Mazzali et al. "A Common Explosion Mechanism for Type Ia Supernovae". In: *Science* 315 (Feb. 2007), p. 825. DOI: 10.1126/science.1136259. eprint: astro-ph/0702351.

[130] P. A. Mazzali et al. "Hubble Space Telescope spectra of the Type Ia supernova SN 2011fe: a tail of low-density, high-velocity material with $Z < Z_{\odot}$". In: MNRAS 439 (Apr. 2014), pp. 1959–1979. DOI: 10.1093/mnras/stu077. arXiv: 1305.2356.

[131] P. A. Mazzali et al. "Nebular spectra and abundance tomography of the Type Ia supernova SN 2011fe: a normal SN Ia with a stable Fe core". In: MNRAS 450 (July 2015), pp. 2631–2643. DOI: 10.1093/mnras/stv761. arXiv: 1504.04857 [astro-ph.HE].

[132] P. A. Mazzali et al. "The Aspherical Properties of the Energetic Type Ic SN 2002ap as Inferred from Its Nebular Spectra". In: ApJ 670 (Nov. 2007), pp. 592–599. DOI: 10.1086/521873. arXiv: 0708.0966.

[133] P. A. Mazzali et al. "The Nebular Spectra of the Hypernova SN 1998bw and Evidence for Asymmetry". In: ApJ 559 (Oct. 2001), pp. 1047–1053. DOI: 10.1086/322420. eprint: astro-ph/0106095.

[134] P. A. Mazzali et al. "The nebular spectrum of the Type Ia supernova 2003hv: evidence for a non-standard event". In: MNRAS 416 (Sept. 2011), pp. 881–892. DOI: 10.1111/j.1365-2966.2011.19000.x. arXiv: 1105.1298 [astro-ph.SR].

[135] P. Mazzotta et al. "Ionization balance for optically thin plasmas: Rate coefficients for all atoms and ions of the elements H to NI". In: A&AS 133 (Dec. 1998), pp. 403–409. DOI: 10.1051/aas:1998330. eprint: astro-ph/9806391.

[136] C. F. McKee and J. P. Ostriker. "A theory of the interstellar medium - Three components regulated by supernova explosions in an inhomogeneous substrate". In: ApJ 218 (Nov. 1977), pp. 148–169. DOI: 10.1086/155667.

[137] X. Meng, X. Chen, and Z. Han. "The Impact of Type Ia Supernova Explosions on the Companions in a Binary System". In: PASJ 59 (Aug. 2007), pp. 835–840. DOI: 10.1093/pasj/59.4.835.

[138] R. Mewe and E. H. B. M. Gronenschild. "Calculated X-radiation from optically thin plasmas. IV - Atomic data and rate coefficients for spectra in the range 1-270 A". In: A&AS 45 (July 1981), pp. 11–52.

[139] R. Minkowski. "Spectra of Supernovae". In: PASP 53 (Aug. 1941), p. 224. DOI: 10.1086/125315.

[140] R. Minkowski. "The Spectra of the Supernovae in IC 4182 and in NGC 1003." In: ApJ 89 (Mar. 1939), p. 156. DOI: 10.1086/144037.

[141] D. M. Mitnik and N. R. Badnell. "Dielectronic recombination data for dynamic finite-density plasmas. VIII. The nitrogen isoelectronic sequence". In: A&A 425 (Oct. 2004), pp. 1153–1159. DOI: 10.1051/0004-6361:20041297.

[142] R. Moll et al. "Type Ia Supernovae from Merging White Dwarfs. I. Prompt Detonations". In: ApJ 785, 105 (Apr. 2014), p. 105. DOI: 10.1088/0004-637X/785/2/105. arXiv: 1311.5008 [astro-ph.HE].

[143] K. Motohara et al. "The Asymmetric Explosion of Type Ia Supernovae as Seen from Near-Infrared Observations". In: ApJ 652 (Dec. 2006), pp. L101–L104. DOI: 10.1086/509919. eprint: astro-ph/0610303.

[144] S. N. Nahar. "Electron-ion recombination of FetII". In: Phys. Rev. A 55 (Mar. 1997), pp. 1980–1987. DOI: 10.1103/PhysRevA.55.1980.

[145] S. N. Nahar. "Total electron-ion recombination of Fe III". In: Phys. Rev. A 53 (Apr. 1996), pp. 2417–2424. DOI: 10.1103/PhysRevA.53.2417.

[146] S. N. Nahar, M. A. Bautista, and A. K. Pradhan. "Electron-ion recombination of Fe IV". In: Phys. Rev. A 58 (Dec. 1998), pp. 4593–4602. DOI: 10.1103/PhysRevA.58.4593.

[147] S. N. Nahar, M. A. Bautista, and A. K. Pradhan. "Electron-Ion Recombination of Neutral Iron". In: ApJ 479 (Apr. 1997), pp. 497–503. DOI: 10.1086/303874.

[148] S. N. Nahar and A. K. Pradhan. "Electron-ion recombination in the close-coupling approximation". In: *Physical Review Letters* 68 (Mar. 1992), pp. 1488–1491. DOI: 10.1103/PhysRevLett.68.1488.

[149] S. N. Nahar and A. K. Pradhan. "Electron-Ion Recombination Rate Coefficients, Photoionization Cross Sections, and Ionization Fractions for Astrophysically Abundant Elements. I. Carbon and Nitrogen". In: ApJS 111 (July 1997), pp. 339–355. DOI: 10.1086/313013.

[150] S. N. Nahar and A. K. Pradhan. "Unified treatment of electron-ion recombination in the close-coupling approximation". In: Phys. Rev. A 49 (Mar. 1994), pp. 1816–1835. DOI: 10.1103/PhysRevA.49.1816.

[151] D. Nikolić et al. "Dielectronic recombination of argon-like ions". In: A&A 516, A97 (June 2010), A97. DOI: 10.1051/0004-6361/201014485. arXiv: 1003.5161 [physics.atom-ph].

[152] K. Nomoto, F.-K. Thielemann, and K. Yokoi. "Accreting white dwarf models of Type I supernovae. III - Carbon deflagration supernovae". In: ApJ 286 (Nov. 1984), pp. 644–658. DOI: 10.1086/162639.

[153] T. Nozawa et al. "Formation of Dust in the Ejecta of Type Ia Supernovae". In: ApJ 736, 45 (July 2011), p. 45. DOI: 10.1088/0004-637X/736/1/45. arXiv: 1105.0973 [astro-ph.SR].

[154] P. E. Nugent et al. "Supernova SN 2011fe from an exploding carbon-oxygen white dwarf star". In: Nature 480 (Dec. 2011), pp. 344–347. DOI: 10.1038/nature10644. arXiv: 1110.6201.

[155] H. Nussbaumer and P. J. Storey. "Dielectronic recombination at low temperatures". In: A&A 126 (Sept. 1983), pp. 75–79.

[156] H. Nussbaumer and P. J. Storey. "Dielectronic recombination at low temperatures. II Recombination coefficients for lines of C, N, O". In: A&AS 56 (June 1984), pp. 293–312.

[157] H. Nussbaumer and P. J. Storey. "Dielectronic recombination at low temperatures. III - Recombination coefficients for Mg, Al, SI". In: A&AS 64 (June 1986), pp. 545–555.

[158] H. Nussbaumer and P. J. Storey. "Dielectronic recombination at low temperatures. IV - Recombination coefficients for neon". In: A&AS 69 (Apr. 1987), pp. 123–133.

[159] R. Pakmor et al. "Normal Type Ia Supernovae from Violent Mergers of White Dwarf Binaries". In: ApJ 747, L10 (Mar. 2012), p. L10. DOI: 10.1088/2041-8205/747/1/L10. arXiv: 1201.5123 [astro-ph.HE].

[160] R. Pakmor et al. "The impact of type Ia supernovae on main sequence binary companions". In: A&A 489 (Oct. 2008), pp. 943–951. DOI: 10.1051/0004-6361:200810456. arXiv: 0807.3331.

[161] R. Pakmor et al. "Violent mergers of nearly equal-mass white dwarf as progenitors of subluminous Type Ia supernovae". In: A&A 528, A117 (Apr. 2011), A117. DOI: 10.1051/0004-6361/201015653. arXiv: 1102.1354 [astro-ph.SR].

[162] P. Palmeri and C. Mendoza. "TIPTOPbase". In: *Highlights of Astronomy* 13 (Jan. 2005), p. 662.

[163] K.-C. Pan, P. M. Ricker, and R. E. Taam. "Impact of Type Ia Supernova Ejecta on a Helium-star Binary Companion". In: ApJ 715 (May 2010), pp. 78–85. DOI: 10.1088/0004-637X/715/1/78. arXiv: 1004.0288 [astro-ph.HE].

[164] K.-C. Pan, P. M. Ricker, and R. E. Taam. "Impact of Type Ia Supernova Ejecta on Binary Companions in the Single-degenerate Scenario". In: ApJ 750, 151 (May 2012), p. 151. DOI: 10.1088/0004-637X/750/2/151. arXiv: 1203.1932 [astro-ph.HE].

[165] R. Penney and P. Hoeflich. "Thermonuclear Supernovae: Probing Magnetic Fields by Positrons and Late-time IR Line Profiles". In: ApJ 795, 84 (Nov. 2014), p. 84. DOI: 10.1088/0004-637X/795/1/84. arXiv: 1409.2159 [astro-ph.HE].

[166] D. Pequignot, P. Petitjean, and C. Boisson. "Total and effective radiative recombination coefficients". In: A&A 251 (Nov. 1991), pp. 680–688.

[167] H. B. Perets et al. "A faint type of supernova from a white dwarf with a helium-rich companion". In: Nature 465 (May 2010), pp. 322–325. DOI: 10.1038/nature09056. arXiv: 0906.2003 [astro-ph.HE].

[168] S. Perlmutter et al. "Measurements of Ω and Λ from 42 High-Redshift Supernovae". In: ApJ 517 (June 1999), pp. 565–586. DOI: 10.1086/307221. eprint: astro-ph/9812133.

[169] M. M. Phillips. "The absolute magnitudes of Type IA supernovae". In: ApJ 413 (Aug. 1993), pp. L105–L108. DOI: 10.1086/186970.

[170] A. L. Piro and L. Bildsten. "Neutronization during Type Ia Supernova Simmering". In: ApJ 673, 1009-1013 (Feb. 2008), pp. 1009–1013. DOI: 10.1086/524189. arXiv: 0710.1600.

[171] T. Plewa. "Detonating Failed Deflagration Model of Thermonuclear Supernovae. I. Explosion Dynamics". In: ApJ 657 (Mar. 2007), pp. 942–960. DOI: 10.1086/511412. eprint: astro-ph/0611776.

[172] L. C. Powell, A. Slyz, and J. Devriendt. "The impact of supernova-driven winds on stream-fed protogalaxies". In: MNRAS 414 (July 2011), pp. 3671–3689. DOI: 10.1111/j.1365-2966.2011.18668.x. arXiv: 1012.2839.

[173] A. K. Pradhan and S. N. Nahar. *Atomic Astrophysics and Spectroscopy*. Jan. 2011.

[174] C. Raskin et al. "^{56}Ni Production in Double-degenerate White Dwarf Collisions". In: ApJ 724 (Nov. 2010), pp. 111–125. DOI: 10.1088/0004-637X/724/1/111. arXiv: 1009.2507 [astro-ph.SR].

[175] C. Raskin et al. "On Type Ia supernovae from the collisions of two white dwarfs". In: MNRAS 399 (Oct. 2009), pp. L156–L159. DOI: 10.1111/j.1745-3933.2009.00743.x. arXiv: 0907.3915 [astro-ph.SR].

[176] C. Raskin et al. "Type Ia Supernovae from Merging White Dwarfs. II. Post-merger Detonations". In: ApJ 788, 75 (June 2014), p. 75. DOI: 10.1088/0004-637X/788/1/75. arXiv: 1312.3649 [astro-ph.HE].

[177] A. G. Riess et al. "Observational Evidence from Supernovae for an Accelerating Universe and a Cosmological Constant". In: AJ 116 (Sept. 1998), pp. 1009–1038. DOI: 10.1086/300499. eprint: astro-ph/9805201.

[178] F. K. Röpke. "Following multi-dimensional type Ia supernova explosion models to homologous expansion". In: A&A 432 (Mar. 2005), pp. 969–983. DOI: 10.1051/0004-6361:20041700. eprint: astro-ph/0408296.

[179] F. K. Röpke and J. C. Niemeyer. "Delayed detonations in full-star models of type Ia supernova explosions". In: A&A 464 (Mar. 2007), pp. 683–686. DOI: 10.1051/0004-6361:20066585. eprint: astro-ph/0703378.

[180] F. K. Röpke et al. "A Three-Dimensional Deflagration Model for Type Ia Supernovae Compared with Observations". In: ApJ 668 (Oct. 2007), pp. 1132–1139. DOI: 10.1086/521347. arXiv: 0707.1024.

[181] F. K. Röpke et al. "Multi-spot ignition in type Ia supernova models". In: A&A 448 (Mar. 2006), pp. 1–14. DOI: 10.1051/0004-6361:20053926. eprint: astro-ph/0510474.

[182] S. Rosswog et al. "Collisions of White Dwarfs as a New Progenitor Channel for Type Ia Supernovae". In: ApJ 705 (Nov. 2009), pp. L128–L132. DOI: 10.1088/0004-637X/705/2/L128. arXiv: 0907.3196 [astro-ph.HE].

[183] A. J. Ruiter et al. "On the brightness distribution of Type Ia supernovae from violent white dwarf mergers". In: MNRAS 429 (Feb. 2013), pp. 1425–1436. DOI: 10.1093/mnras/sts423. arXiv: 1209.0645 [astro-ph.SR].

[184] P. Ruiz-Lapuente. "The late-time emission of thermonuclear supernovae". In: *NATO Advanced Science Institutes (ASI) Series C*. Ed. by P. Ruiz-Lapuente, R. Canal, and J. Isern. Vol. 486. NATO Advanced Science Institutes (ASI) Series C. 1997, p. 681. DOI: 10.1007/978-94-011-5710-0_41. eprint: astro-ph/9604094.

[185] P. Ruiz-Lapuente and L. B. Lucy. "Nebular spectra of type IA supernovae as probes for extragalactic distances, reddening, and nucleosynthesis". In: ApJ 400 (Nov. 1992), pp. 127–137. DOI: 10.1086/171978.

[186] G. B. Rybicki and A. P. Lightman. *Radiative processes in astrophysics*. 1979.

[187] R. A. Scalzo, A. J. Ruiter, and S. A. Sim. "The ejected mass distribution of Type Ia supernovae: a significant rate of non-Chandrasekhar-mass progenitors". In: MNRAS 445 (Dec. 2014), pp. 2535–2544. DOI: 10.1093/mnras/stu1808. arXiv: 1408.6601 [astro-ph.HE].

[188] R. A. Scalzo et al. "Nearby Supernova Factory Observations of SN 2007if: First Total Mass Measurement of a Super-Chandrasekhar-Mass Progenitor". In: ApJ 713 (Apr. 2010), pp. 1073–1094. DOI: 10.1088/0004-637X/713/2/1073. arXiv: 1003.2217.

[189] R. Scalzo et al. "Type Ia supernova bolometric light curves and ejected mass estimates from the Nearby Supernova Factory". In: MNRAS 440 (May 2014), pp. 1498–1518. DOI: 10.1093/mnras/stu350. arXiv: 1402.6842.

[190] R. W. Schunk and P. B. Hays. "Photoelectron energy losses to thermal electrons". In: Planet. Space Sci. 19 (Jan. 1971), pp. 113–117. DOI: 10.1016/0032-0633(71)90071-7.

[191] I. R. Seitenzahl, F. Ciaraldi-Schoolmann, and F. K. Röpke. "Type Ia supernova diversity: white dwarf central density as a secondary parameter in three-dimensional delayed detonation models". In: MNRAS 414 (July 2011), pp. 2709–2715. DOI: 10.1111/j.1365-2966.2011.18588.x. arXiv: 1012.4929 [astro-ph.SR].

[192] I. R. Seitenzahl et al. "Three-dimensional delayed-detonation models with nucleosynthesis for Type Ia supernovae". In: MNRAS 429 (Feb. 2013), pp. 1156–1172. DOI: 10.1093/mnras/sts402. arXiv: 1211.3015 [astro-ph.SR].

[193] B. J. Shappee et al. "No Stripped Hydrogen in the Nebular Spectra of Nearby Type Ia Supernova 2011fe". In: ApJ 762, L5 (Jan. 2013), p. L5. DOI: 10.1088/2041-8205/762/1/L5. arXiv: 1210.3027.

[194] K. J. Shen and L. Bildsten. "The Ignition of Carbon Detonations via Converging Shock Waves in White Dwarfs". In: ApJ 785, 61 (Apr. 2014), p. 61. DOI: 10.1088/0004-637X/785/1/61. arXiv: 1305.6925 [astro-ph.HE].

[195] I. Shivvers et al. "Nebular spectroscopy of the nearby Type IIb supernova 2011dh". In: MNRAS 436 (Dec. 2013), pp. 3614–3625. DOI: 10.1093/mnras/stt1839. arXiv: 1307.2246 [astro-ph.HE].

[196] J. M. Shull and M. van Steenberg. "The ionization equilibrium of astrophysically abundant elements". In: ApJS 48 (Jan. 1982), pp. 95–107. DOI: 10.1086/190769.

[197] J. M. Shull and M. van Steenberg. "The ionization equilibrium of astrophysically abundant elements". In: ApJS 48 (Jan. 1982), pp. 95–107. DOI: 10.1086/190769.

[198] J. M. Silverman et al. "Late-time Spectral Observations of the Strongly Interacting Type Ia Supernova PTF11kx". In: ApJ 772, 125 (Aug. 2013), p. 125. DOI: 10.1088/0004-637X/772/2/125. arXiv: 1303.7234.

[199] S. A. Sim. "Multidimensional simulations of radiative transfer in Type Ia supernovae". In: MNRAS 375 (Feb. 2007), pp. 154–162. DOI: 10.1111/j.1365-2966.2006.11271.x. eprint: astro-ph/0611677.

[200] J. C. Slater. "Atomic Shielding Constants". In: *Phys. Rev.* 36 (1 July 1930), pp. 57–64. DOI: 10.1103/PhysRev.36.57. URL: http://link.aps.org/doi/10.1103/PhysRev.36.57.

[201] J. Sollerman et al. "SN 1998bw at Late Phases". In: ApJ 537 (July 2000), pp. L127–L130. DOI: 10.1086/312763. eprint: astro-ph/0006406.

[202] J. Sollerman et al. "The late-time light curve of the type Ia supernova 2000cx". In: A&A 428 (Dec. 2004), pp. 555–568. DOI: 10.1051/0004-6361:20041320. eprint: astro-ph/0409338.

[203] M. Stehle et al. "Abundance stratification in Type Ia supernovae - I. The case of SN 2002bo". In: MNRAS 360 (July 2005), pp. 1231–1243. DOI: 10.1111/j.1365-2966.2005.09116.x. eprint: astro-ph/0409342.

[204] E. Stoner. "The Equilibrium of Dense Stars". In: *The London, Edinburgh, and Dublin Philosophical Magazine and Journal of Science: Series 7, Volume 9, Issue 60, p. 944-963* 9 (Jan. 1930), pp. 944–963.

[205] M. Stritzinger et al. "Constraints on the progenitor systems of type Ia supernovae". In: A&A 450 (Apr. 2006), pp. 241–251. DOI: 10.1051/0004-6361:20053652. eprint: astro-ph/0506415.

[206] R. S. Sutherland and M. A. Dopita. "Cooling functions for low-density astrophysical plasmas". In: ApJS 88 (Sept. 1993), pp. 253–327. DOI: 10.1086/191823.

[207] D. A. Swartz. "Charge transfer in helium-rich supernova plasma". In: ApJ 428 (June 1994), pp. 267–274. DOI: 10.1086/174238.

[208] D. A. Swartz, P. G. Sutherland, and R. P. Harkness. "Gamma-Ray Transfer and Energy Deposition in Supernovae". In: ApJ 446 (June 1995), p. 766. DOI: 10.1086/175834. eprint: astro-ph/9501005.

[209] S. Taubenberger et al. "[O I] $\lambda\lambda$6300, 6364 in the Nebular Spectrum of a Subluminous Type Ia Supernova". In: ApJ 775, L43 (Oct. 2013), p. L43. DOI: 10.1088/2041-8205/775/2/L43. arXiv: 1308.3145 [astro-ph.SR].

[210] C. M. Telesco et al. "Mid-IR Spectra of Type Ia SN 2014J in M82 Spanning the First 4 Months". In: ApJ 798, 93 (Jan. 2015), p. 93. DOI: 10.1088/0004-637X/798/2/93. arXiv: 1409.2125 [astro-ph.SR].

[211] F.-K. Thielemann, K. Nomoto, and K. Yokoi. "Explosive nucleosynthesis in carbon deflagration models of Type I supernovae". In: A&A 158 (Apr. 1986), pp. 17–33.

[212] F. X. Timmes, E. F. Brown, and J. W. Truran. "On Variations in the Peak Luminosity of Type Ia Supernovae". In: ApJ 590 (June 2003), pp. L83–L86. DOI: 10.1086/376721. eprint: astro-ph/0305114.

[213] J. K. Truelove and C. F. McKee. "Evolution of Nonradiative Supernova Remnants". In: ApJS 120 (Feb. 1999), pp. 299–326. DOI: 10.1086/313176.

[214] H. van Regemorter. "Rate of Collisional Excitation in Stellar Atmospheres." In: ApJ 136 (Nov. 1962), p. 906. DOI: 10.1086/147445.

[215] D. A. Verner and G. J. Ferland. "Atomic Data for Astrophysics. I. Radiative Recombination Rates for H-like, He-like, Li-like, and Na-like Ions over a Broad Range of Temperature". In: ApJS 103 (Apr. 1996), p. 467. DOI: 10.1086/192284. eprint: astro-ph/9509083.

[216] G. S. Voronov. "A Practical Fit Formula for Ionization Rate Coefficients of Atoms and Ions by Electron Impact: Z = 1-28". In: *Atomic Data and Nuclear Data Tables* 65 (1997), p. 1. DOI: 10.1006/adnd.1997.0732.

[217] B. Wang and Z. Han. "Companion stars of type Ia supernovae and hypervelocity stars". In: A&A 508 (Dec. 2009), pp. L27–L30. DOI: 10.1051/0004-6361/200913326. arXiv: 0911.3316 [astro-ph.SR].

[218] B. Wang and Z. Han. "Progenitors of type Ia supernovae". In: New A Rev. 56 (June 2012), pp. 122–141. DOI: 10.1016/j.newar.2012.04.001. arXiv: 1204.1155 [astro-ph.SR].

[219] B. Wang et al. "The helium star donor channel for the progenitors of Type Ia supernovae". In: MNRAS 395 (May 2009), pp. 847–854. DOI: 10.1111/j.1365-2966.2009.14545.x. arXiv: 0901.3496 [astro-ph.SR].

[220] R. F. Webbink. "Double white dwarfs as progenitors of R Coronae Borealis stars and Type I supernovae". In: ApJ 277 (Feb. 1984), pp. 355–360. DOI: 10.1086/161701.

[221] J. C. Wheeler, M. Lecar, and C. F. McKee. "Supernovae in binary systems". In: ApJ 200 (Aug. 1975), pp. 145–157. DOI: 10.1086/153771.

[222] J. Whelan and I. Iben Jr. "Binaries and Supernovae of Type I". In: ApJ 186 (Dec. 1973), pp. 1007–1014. DOI: 10.1086/152565.

[223] D. T. Woods, J. M. Shull, and C. L. Sarazin. "Recombination coefficients for iron ions". In: ApJ 249 (Oct. 1981), pp. 399–401. DOI: 10.1086/159298.

[224] S. E. Woosley, A. Heger, and T. A. Weaver. "The evolution and explosion of massive stars". In: *Reviews of Modern Physics* 74 (Nov. 2002), pp. 1015–1071. DOI: 10.1103/RevModPhys.74.1015.

[225] S. E. Woosley et al. "Type Ia Supernova Light Curves". In: ApJ 662 (June 2007), pp. 487–503. DOI: 10.1086/513732. eprint: astro-ph/0609562.

[226] S. Woosley and T. Janka. "The physics of core-collapse supernovae". In: *Nature Physics* 1 (Dec. 2005), pp. 147–154. DOI: 10.1038/nphys172. eprint: astro-ph/0601261.

[227] Woosley and Weaver. "Sub-Chandrasekhar mass models for Type IA supernovae". In: ApJ 423 (Mar. 1994), pp. 371–379. DOI: 10.1086/173813.

[228] Woosley and Weaver. "The physics of supernova explosions". In: ARA&A 24 (1986), pp. 205–253. DOI: 10.1146/annurev.aa.24.090186.001225.

[229] Y. Xu and R. McCray. "Energy degradation of fast electrons in hydrogen gas". In: ApJ 375 (July 1991), pp. 190–201. DOI: 10.1086/170180.

[230] S.-C. Yoon and N. Langer. "The first binary star evolution model producing a Chandrasekhar mass white dwarf". In: A&A 412 (Dec. 2003), pp. L53–L56. DOI: 10.1051/0004-6361:20034607. eprint: astro-ph/0402286.

[231] S. M. Younger. "Electron impact ionization cross sections and rates for highly ionized atoms." In: J. Quant. Spec. Radiat. Transf. 26 (1981), pp. 329–337. DOI: 10.1016/0022-4073(81)90127-8.

[232] O. Zatsarinny et al. "Dielectronic recombination data for dynamic finite-density plasmas. II. The oxygen isoelectronic sequence". In: A&A 412 (Dec. 2003), pp. 587–595. DOI: 10.1051/0004-6361:20031462.

[233] O. Zatsarinny et al. "Dielectronic recombination data for dynamic finite-density plasmas. II. The oxygen isoelectronic sequence". In: A&A 438 (Aug. 2005), pp. 743–744. DOI: 10.1051/0004-6361:20053312e.

[234] O. Zatsarinny et al. "Dielectronic recombination data for dynamic finite-density plasmas. IV. The carbon isoelectronic sequence". In: A&A 440 (Sept. 2005), pp. 1203–1204. DOI: 10.1051/0004-6361:20034174e.

[235] O. Zatsarinny et al. "Dielectronic recombination data for dynamic finite-density plasmas. IX. The fluorine isoelectronic sequence". In: A&A 447 (Feb. 2006), pp. 379–387. DOI: 10.1051/0004-6361:20053737.

[236] O. Zatsarinny et al. "Dielectronic recombination data for dynamic finite-density plasmas. VII. The neon isoelectronic sequence". In: A&A 426 (Nov. 2004), pp. 699–705. DOI: 10.1051/0004-6361:20040463.